NUMERICAL SIMULATIONS OF RELATIVISTIC HEAVY-ION REACTIONS

By

Frank Cecil Daffin

AN ABSTRACT OF A DISSERTATION

Submitted to
Michigan State University
in partial fulfillment of the requirements
for the degree of

DOCTOR OF PHILOSOPHY

Department of Physics and Astronomy

1998

Professor Wolfgang Bauer

ABSTRACT

NUMERICAL SIMULATIONS OF RELATIVISTIC HEAVY-ION REACTIONS

By

Frank Cecil Daffin

Bulk quantities of nuclear matter exist only in the compact bodies of the universe. There the crushing gravitational forces overcome the Coulomb repulsion in massive stellar collapses. Nuclear matter is subjected to high pressures and temperatures as shock waves propagate and burn their way through stellar cores. The bulk properties of nuclear matter are important parameters in the evolution of these collapses, some of which lead to nucleosynthesis.

The nucleus is rich in physical phenomena. Above the Coulomb barrier, complex interactions lead to the distortion of, and as collision energies increase, the destruction of the nuclear volume. Of critical importance to the understanding of these events is an understanding of the aggregate microscopic processes which govern them.

In an effort to understand relativistic heavy-ion reactions, the Boltzmann-Uehling-Uhlenbeck[Ueh33] (BUU) transport equation is used as the framework for a numerical model. In the years since its introduction, the numerical model has been instrumental in providing a coherent, microscopic, physical description of these complex, highly non-linear events.

This treatise describes the background leading to the creation of our numerical model of the BUU transport equation, details of its numerical implementation, its application to the study of relativistic heavy-ion collisions, and some of the experimental observables used to compare calculated results to empirical results.

The formalism evolves the one-body Wigner phase-space distribution of nucleons in time under the influence of a single-particle nuclear mean field interaction and a collision source term. This is essentially the familiar Boltzmann transport equation whose source term has been modified to address the *Pauli exclusion principle.*

Two elements of the model allow extrapolation from the study of nuclear collisions to bulk quantities of nuclear matter: the modification of nucleon scattering cross sections in nuclear matter, and the compressibility of nuclear matter. Both are primarily subject to the short-range portion of the inter-nucleon potential, and do not show strong finite-size effects.

To that end, several useful observables are introduced and their behavior, as BUU model parameters are changed, explored. The average, directed, in-plane, transverse momentum distribution in rapidity is the oldest of the observables presented in this work. Its slope at mid-rapidity is called the flow of the event, and well characterizes the interplay of repulsive and attractive elements of the dynamics of the events.

The BUU model has been quite successful in its role of illuminating the physics of intermediate energy heavy-ion collisions. Though current numerical implementations suffer from some shortcomings they have nonetheless served the community well.

NUMERICAL SIMULATIONS OF RELATIVISTIC HEAVY-ION REACTIONS

By

Frank Cecil Daffin

A DISSERTATION

Submitted to
Michigan State University
in partial fulfillment of the requirements
for the degree of

DOCTOR OF PHILOSOPHY

Department of Physics and Astronomy

1998

ABSTRACT

NUMERICAL SIMULATIONS OF RELATIVISTIC HEAVY-ION REACTIONS

By

Frank Cecil Daffin

Bulk quantities of nuclear matter exist only in the compact bodies of the universe. There the crushing gravitational forces overcome the Coulomb repulsion in massive stellar collapses. Nuclear matter is subjected to high pressures and temperatures as shock waves propagate and burn their way through stellar cores. The bulk properties of nuclear matter are important parameters in the evolution of these collapses, some of which lead to nucleosynthesis.

The nucleus is rich in physical phenomena. Above the Coulomb barrier, complex interactions lead to the distortion of, and as collision energies increase, the destruction of the nuclear volume. Of critical importance to the understanding of these events is an understanding of the aggregate microscopic processes which govern them.

In an effort to understand relativistic heavy-ion reactions, the Boltzmann-Uehling-Uhlenbeck[Ueh33] (BUU) transport equation is used as the framework for a numerical model. In the years since its introduction, the numerical model has been instrumental in providing a coherent, microscopic, physical description of these complex, highly non-linear events.

This treatise describes the background leading to the creation of our numerical model of the BUU transport equation, details of its numerical implementation, its

application to the study of relativistic heavy-ion collisions, and some of the experimental observables used to compare calculated results to empirical results.

The formalism evolves the one-body Wigner phase-space distribution of nucleons in time under the influence of a single-particle nuclear mean field interaction and a collision source term. This is essentially the familiar Boltzmann transport equation whose source term has been modified to address the *Pauli exclusion principle*.

Two elements of the model allow extrapolation from the study of nuclear collisions to bulk quantities of nuclear matter: the modification of nucleon scattering cross sections in nuclear matter, and the compressibility of nuclear matter. Both are primarily subject to the short-range portion of the inter-nucleon potential, and do not show strong finite-size effects.

To that end, several useful observables are introduced and their behavior, as BUU model parameters are changed, explored. The average, directed, in-plane, transverse momentum distribution in rapidity is the oldest of the observables presented in this work. Its slope at mid-rapidity is called the flow of the event, and well characterizes the interplay of repulsive and attractive elements of the dynamics of the events.

The BUU model has been quite successful in its role of illuminating the physics of intermediate energy heavy-ion collisions. Though current numerical implementations suffer from some shortcomings they have nonetheless served the community well.

This work is dedicated to the holy pursuit of the truth, and the love of the chase.

ACKNOWLEDGMENTS

I wish to thank my parents for their stubborn, unflagging love and support of this gross underachiever. Without their Jobian patience I would undoubtedly be pumping gas and watching pro wrestling. Thank you.

Of the academics I have known, none have been more influential than Gerald Chatwood, my high school science and mathematics teacher. His class was the one bright spot in an otherwise dreary high school adolescent nightmare.

Professor Wolfgang Bauer deserves my thanks for his wise guidance and sharp insight during my study for the Ph.D. While it goes without saying, it should be nonetheless, that without Professor Bauer's support this work and the incalculable intellectual growth from which it springs would not have been possible.

Professor PawełDanielewicz is one of the brightest people that its been my fortune to know. Much of this work would not have been possible without his stimulating discussions.

Professor Vladimir Zelevinsky deserves acknowledgement for his astonishingly clear understanding of the fundamentals of modern physics. His presence in the faculty is a rare gift.

The ear of David Brown has been bent more than once during the final stages of this work. To him I owe a debt of gratitude for his objective attention.

Finally, I thank Professor Dan Stump for his efforts in the classroom. Learning quantum mechanics has never been so easy.

Contents

List of Tables

List of Figures

Chapter 1

BUU and the Nuclear Equation of State

1.1 Introduction

It is primarily the accessibility of ordinary matter, such as water, that has fostered such a well-developed, mature science of its bulk properties. After all we are macroscopic, Newtonian beings immersed in a world of inches and miles per hour. Our very biology is a reflection of the relationship we have with the slow, macroscopic world. It is little wonder that we have such difficulty studying elements of nature which are very far removed from our own scales of time and space. The very fast–the relativistic world of Einstein–and the very small–the world of Bohr–are very strange to us. We must fashion elaborate machines to communicate with these worlds, and apply expert skill in gleaning the effects of nature from the effects of the machinery.

Extracting the bulk properties of nuclear matter is thus a wonderfully challenging endeavor. Protons and neutrons make up the vast majority of the mass of our solar system, including the thesis you are now reading. Yet because these particles are so small, and ordinarily so tightly bound to one another, studying them and their interaction is difficult. They are quantum-mechanical systems–systems so small, the mere act of measurement significantly alters their state.

The only empirical observations that can be made of large quantities of nuclear matter are astronomical, since the Coulomb repulsion among protons renders macroscopic quantities of nuclear matter unstable. Only when huge amounts are brought together does the gravitational attraction overcome the Coulomb repulsion. However, such large masses cannot be formed in our solar system without catastrophic results (not to mention the technical challenges in doing so), thus we are relegated to being the local voyeur–peeking in from a distance on events over which we have no control. We can neither choose nor can we know their initial states. In addition, the great distance between us and these systems imposes other uncertainties, themselves objects of current debate.

Another option is to study the small, stable packages of nuclear matter we have here on earth: the nuclei of atoms. Far more accessible, they nonetheless pose their own problems in the effort to know the nuclear equation of state. There are strict limitations placed by the nature of these systems on the information we can extract from them, and on the mathematical feasibility of extrapolating this information to explain infinite nuclear matter. The systems are very small: with fewer than 1000 nucleons in any single interaction and collision volumes of the order of $10^{-40}m^3$. Interaction times are typically on the order of 10^{-21} seconds. Apart from the *Heisenberg uncertainty Principle* $\Delta x_i \Delta p_j \gtrsim \delta_{ij}\hbar$, $\Delta E \Delta t \gtrsim \hbar$, where Δx, Δp, ΔE, and Δt are the uncertainties in length, momentum, energy and time of an event, respectively, and where δ_{ij} is the Kronecker delta, there are technical limitations.

To be correct, thermodynamic quantities such as temperature are well defined only for infinite matter. That is, the differential volume δv is infinitesimal compared to the volume. In addition, the matter contained within δv is to be continuous. Macroscopic systems of ordinary matter do not meet these criteria, but it can be shown that they deviate in-substantially from the ideal. In real systems of ordinary matter, one may expect to study a mole molecules. So the ideal of continuous matter becomes a fair approximation. Such is not the case for even the compound nuclei from heavy ion collisions. One must then be careful when applying the language of thermodynamics to the science of heavy ion physics, or any other quantum process.

At intermediate energies, roughly between 50 MeV per nucleon and 1 GeV per nucleon, the constituents of the heavy-ion collisions (protons, neutrons and mesons) are relativistic, quantum-mechanical and strongly coupled. The Coulomb and the strong nuclear forces are important in the evolution of these systems. It is no surprise that a model derived from first principles is currently, and for the foreseeable future, computationally infeasible. To create a useful model, one is forced to make judicious approximations.

The effort to understand the nuclear equation of state at intermediate energies has for several years been focused upon the interplay between empirical data and observables generated from numerical models. The information gathered from the comparison tells us something about these models and nuclear matter in the context of those models.

1.2 The BUU Model of Nuclear Matter

Perhaps the first suggestions of an independent, free particle description of what was then called “high energy” (around 100 MeV per nucleon) nuclear collisions were set forth in the late nineteen forties [Ser47]. There the transparency of ions to incident protons and neutrons was argued from the the degeneracy of fermionic matter in the nucleus.

This simple model, eventually known as the Intranuclear Cascade (INC) model, formed some of the foundation upon which the application of more sophisticated transport models to heavy-ion collisions would be built. It would be almost thirty years until practical numerical techniques could be implemented on computers accessible to the nuclear physics community [Bon76, Smi77, Cug81]. While the INC was a good first step towards a practical model of heavy-ion collisions, it featured only hard collisions among the nucleons and neglected the attractive portion of the internulceon potential.

Another model which saw early application to heavy-ion collisions was the time-dependent-Hartree-Fock (TDHF). Some calculations were quantitatively promising, but serious theoretical problems existed [Dan97, Neg82]. Chief among these was the lack of two-body correlations and collisionless dynamics, which led to slow thermalization. It saw better success in describing the low-energy excitation modes of heavy ions. It is easy to see why this is so: a principle approximation of Hartree-Fock theory is that the Hamiltonian can be written as a single particle term and a weak two-body term. The assumption that two-body dynamics are unimportant is better suited for low-energy processes. At high energies the approximation is poor.

A treatment of the long-range interaction among nucleons can be found in Vlasov transport theory. In fact one can obtain the Vlasov transport equation from TDHF equations by applying the random phase approximation and recasting the result using the Wigner transform [Koon79, Ber88]. The result, as one might guess, is a collisionless approximation.

These models are incomplete compared to the Boltzmann-Uehling-Uhlenbeck transport (BUU) equation, Equation [Ueh33]:

$$\frac{\partial f}{\partial t} + D(f) = \int d\phi_1 \int g w(\vartheta g) d\Omega \{ f' f_1' (1+\theta f)(1+\theta f_1) - f f_1 (1+\theta f')(1+\theta f_1') \}, \quad (1.1)$$

where primes denote quantities that are to be taken after collision, f is the Wigner phase-space distribution, g is the relative velocity of the colliding particles (binary collisions only), ϑ is the change in the direction of g, θ takes the value 0 for classical statistics, -1 for Fermi-Dirac statistics, $+1$ for Bose-Einstien statistics, and $d\Omega$ is the usual solid angle. The expression

$$D(f) = r_\imath(\partial f/\partial x_\imath) + X_\imath(\partial f/\partial r_\imath) \tag{1.2}$$

describes the transport of mass and energy into and out of a unit volume in phase-space, where $\imath$ is a summation index, and $X_\imath$ represents the three components of the force per unit mass. Here one finds role of the long-range interaction and collisions. In more recent papers Equation 1.1 has a more familiar form [Ber84, Ber88]:

$$\begin{aligned} \frac{\partial f}{\partial t} + \vec{v} \cdot \nabla_r f - \nabla_r U \cdot \nabla_p f = -\frac{1}{(2\pi)^6} \int & d^3p_2 d^3p_{2'} d\Omega \frac{d\sigma}{d\Omega} v_{12} \\ & \times \{[f f_2 (1 - f_{1'})(1 - f_{2'}) - f_{1'} f_{2'} (1 - f_1)(1 - f_2)] \\ & \times (2\pi)^3 \delta^3(\vec{p} + \vec{p}_2 - \vec{p}_{1'} - \vec{p}_{2'})\} \end{aligned} \tag{1.3}$$

where U is the nuclear mean field, $d\sigma/d\Omega$ is nucleon scattering cross section (both are discussed below), primes denote quantities to be taken after the collision between particles 1 and 2. Note that the two colliding particles change their momenta, but their positions in configuration-space remain unchanged (they will be propagated to new positions using Hamilton's equations in the mean field). An important feature of Equation 1.3 are the terms $(1 - f)$ in the collision integral. They facilitate an approximate treatment of the *Pauli Exclusion Principle*, since f is a measure of the occupancy of phase-space.

Collisions which have final states in highly occupied regions of phase-space are stochastically forbidden at a rate proportional to f'. This allows partial transparency of nucleons incident upon bulk nuclear matter found in Serber's work[Ser47].

It can be shown that the BUU formalism is a truncation in the BBGKY (Bogoliubov-Born-Green-Kirkwood-Yvon)[Won77, Bau86a] hierarchy. The full N-body theory is quantum-mechanically exact. However, the full N-body is beyond us today. The truncation allows a numerical solution, but cannot address multi-particle dynamics. Nonetheless, the BUU formalism is very well suited to calculation of the single-body phase-space distribution.

1.2.1 Nuclear Mean Field Parameterizations

Equation 1.3 features U, a mean field which is the average of the potentials of the surrounding matter on a single nucleon. Frequently a parameterization of the Skyrme many-body potential [Skyr59] is used:

$$U(\rho) = A\left(\frac{\rho}{\rho_0}\right) + B\left(\frac{\rho}{\rho_0}\right)^{\sigma} \tag{1.4}$$

where ρ_0 is the normal, zero-temperature, zero-pressure nuclear matter density, A is attractive, B is repulsive, and $\sigma > 1$. The parameters A, B and σ are partially determined by the nuclear saturation density of infinite nuclear matter $\rho_0 = 0.16\,fm^{-3}$, and saturation binding energy $E/A = -16\,\mathrm{MeV}$. In the studies presented in this work, the compressibility [Ber88]:

$$K = 9(\frac{p^2{}_F}{3m} + A + \sigma B) \tag{1.5}$$

is treated as a “free” parameter to unambiguously fix all three parameters:

$$\begin{aligned} A &= -29.81 - 46.90\left[\frac{K + 44.73}{K - 166.32}\right] \\ B &= 23.45\left[\frac{K + 255.78}{K - 166.32}\right] \\ \sigma &= \frac{K + 44.73}{211.05}. \end{aligned}$$

Note that p_F is the Fermi momentum of nuclear matter.

The mean field allows the nucleons to be initialized with Fermi momentum– otherwise the system would quickly disassociate–as well as filling an important role in the

Model	K(MeV)	A(MeV)	B(MeV)	σ
Soft	200	-356	303	$7/6$
Medium	235	-218	164	$4/3$
Hard	380	-124	70.5	2

Table 1.1: Parameter sets used for the density-dependent mean field U

evolution of phase-space. Typical numbers for the compressibility K are 200MeV, often referred to as a "soft" equation of state, and 380MeV, a "stiff" equation of state, Ref.[Ber84]. Note that the "medium" mean field was introduced by Bauer,*et al.*[Bau86].

Development of momentum dependent mean-field, which arises from the inclusion of non-local interactions, is illustrated in some detail in Ref.[Jeu76]. Early implementations of this dependence appear in Ref.[Aich87, Gale87]. There are two popular forms of this dependence, the one used in the studies presented in this work is from Ref.[Wel88]:

$$U(\rho,\vec{p}) = A\left(\frac{\rho}{\rho_0}\right) + B\left(\frac{\rho}{\rho_0}\right)^{\sigma} + \frac{C}{\rho_0}\int d^3p' \frac{f(\vec{r},\vec{p}')}{1+\left(\frac{\vec{p}-\vec{p}'}{\Lambda}\right)^2} \tag{1.6}$$

In this work two parameter sets are used for the momentum-dependent mean field: $A = -110.44\,\mathrm{MeV}, B = 140.9\,\mathrm{MeV}, C = -64.95\,\mathrm{MeV}, \sigma = 1.24, \Lambda = 1.58\, p_F|_{T=0,\rho=\rho_0}$, which gives a compressibility of 215 MeV, and $A = -5.89\,\mathrm{MeV}$, $B = 36.21\,\mathrm{MeV}$, $C = -64.91\,\mathrm{MeV}$, $\sigma = 2.45$, $\Lambda = 1.58\, p_F|_{T=0,\rho=\rho_0}$, which gives a compressibility of 380 MeV.

1.2.2 Nucleon Scattering Cross-Section and the Collision Integral

Of vital importance is the role of hard, short-range interactions among the nucleons. The mean field is primarily responsible for the longer range interactions, both attractive and repulsive in nature, but the repulsive, short-range interaction is carried by scattering. The collision cross sections used here in the BUU equation are parameterizations of empirical data by the Particle Data Group [PDG88]. The following scattering processes are built into the computer code used in this work:

$$\begin{array}{ccccccc}
\mathrm{N} & + & \mathrm{N} & \rightarrow & \mathrm{N} & + & \mathrm{N} \\
\mathrm{N} & + & \mathrm{N} & \rightarrow & \mathrm{N} & + & \Delta \\
\mathrm{N} & + & \Delta & \rightarrow & \mathrm{N} & + & \mathrm{N} \\
\mathrm{N} & + & \Delta & \rightarrow & \mathrm{N} & + & \Delta \\
\Delta & + & \Delta & \rightarrow & \Delta & + & \Delta \\
\mathrm{N} & + & \mathrm{N} & \rightarrow & \mathrm{N}^* & + & \mathrm{N}.
\end{array}$$

Δ is a resonant state of a $\pi^{\pm}$-meson and a nucleon, and thus it has four charge states: Δ^{++}, Δ^{+}, Δ^{0}, and Δ^{-}. It has a mass of 1232 MeV, does not contribute to the Pauli exclusion of nucleons (it is a spin-$\frac{3}{2}$ fermion), and has a mean lifetime of about 1.8 fm/c. This resonance plays an important role of in entropy production during heavy-ion collisions. N* is an excited state of a nucleon. However, its production rate is only about four percent of all resonances produced in heavy-ion collisions at 800 MeV/nucleon [Dan95]–this energy approaches the upper limit of applicability of the BUU code featured in this work. Thus, this work will ignore this rare process.

1.3 Numerical Implementation of the BUU Equation

There are numerous ways to execute the BUU equation in computer code. One may attempt a numerical solution of Equation 1.3. However, the code used in this work attempts a simulation of heavy-ion collisions rather than an explicit solution of the phase-space distribution $f(\vec{r},\vec{p})$.

1.3.1 The Parallel Ensemble

The calculations of heavy-ion collisions which used the INC model amounted to Monte Carlo solutions to the collision integral. The stochastic sampling of phase-space meant that meaningful results would be obtained when an adequate portion of phase-space was calculated. Here there the situation is modified by the inclusion of the nuclear mean field. Derivatives in coordinate-space (for density-dependent mean fields) and derivatives in momentum-space (for density- and momentum-dependent mean fields) take on spurious numerical fluctuations due to two approximations, both of which lead to a calculable model.

In BUU formalism the collision integral is treated as a continuous source function. As the number of test-particles goes to infinity, the BUU equation becomes exact. However, the model is numerically executed on finite-state machines (computers), and the microscopic collision process is never mathematically infinitesimal. The collision integral is then a finite sum of discontinuous elements. Its contribution to phase-space is never continuous, and derivatives on the phase-space distribution, or parts of it like the matter or momentum density, are divergent in general. Numerically the derivatives are finite differences, and while not immune to divergence such as in the case of a divide by zero, they are nonetheless susceptible to fluctuations resulting from the aforementioned approximation. In addition, the calculation of the Pauli-blocking factors (terms of $1 - f(\vec{r},\vec{p})$) suffers as well. This causes problems at the low energy limit for this model in the form of enhanced transparency.

Another source of numerical fluctuation concerns the derivatives the mean field potential. Formulated from the Skyrme parameterization, which begins with

Dirac-delta functions, it is density-dependent and, if chosen to be so, momentum-dependent as well; whenever derivatives are taken of this field, they are naturally subject to the same divergences as are derivatives of the phase-space distribution. The nucleons are propagated each time step in the computer code using Hamilton's equations of motion:

$$\frac{d\vec{p}}{dt} = -\nabla_r U \tag{1.7}$$

$$\frac{d\vec{r}}{dt} = \frac{\vec{p}}{\sqrt{\vec{p}\cdot\vec{p}+m^2}} + \nabla_p U, \tag{1.8}$$

where ∇_p is the gradient with respect to momentum-space. One can easily see in Equations 1.4 and 1.6 where the derivatives in phase-space appear.

Efforts to address these spurious fluctuations in the collision integral and phase-space distribution have been implemented in the model studied in this work. An ensemble of nucleus-nucleus collisions is evolved in parallel in time. Nucleon collisions occur only among nucleons of the same member of the ensemble. There is no collisional communication among the members of the ensemble. This independence of the members of the ensemble is used to reduce the combinatorial burden. However, in order to generate the mean field, the mass density and momentum density are averaged over the entire ensemble. This goes a long way to quell the stochastic noise from the collision integral.

Another method employed to control spurious fluctuations is to distribute the matter of the nucleon over configuration-space. The "position" of the nucleon marks the centroid of the distribution, with a constant Gaussian fall-off in all directions. Nuclear matter is smeared in the density distribution so that derivatives in this distribution are better behaved.

1.3.2 Initialization

A semi-classical picture of the nucleus is used with the BUU equation. A nucleus is initialized by randomly distributing its nucleons throughout a spherical volume which has a radius given by

$$R = 1.2(A^{\frac{1}{3}}) fm,$$

where A is the number of nucleons in the nucleus. The form of this formula is a result of the profile of the inter-nucleon potential: a hard-core repulsion at short distances ($r \lesssim 1\, fm$), a strong attraction at intermediate distances ($1 \lesssim r \lesssim 2\, fm$), and a weak attraction at long distances ($r > 2\, fm$). The direction of a nucleon's Fermi momentum is randomly assigned, but its magnitude is calculated from the local density given by the Woods-Saxon prescription. Thus those nucleons near the surface of the nucleus, where the density decreases for real nuclei, have a smaller Fermi momentum than those nearer the center of the nucleus. This procedure is repeated for each of the members of the ensemble of pairs of nuclei to be used in the calculation.

1.3.3 The Collision Integral

The basis of the treatment of the collision integral, the right hand side of Equation 1.3, lies in previous attempts [Bon76, Smi77, Cug81] at a Monte Carlo solution. In this work the baryons are assigned an index which in various arrays within the program allow extraction of their position, momentum and identity. This information is used in the routines which effectively constitute the collision integral. A procedural outline will be used to describe the numerical implementation for two nucleons.

From the main program a collision routine is called which first randomly chooses a particle (baryon or π-meson). If it is a resonance, then whether, and if so how, the resonance will decay is calculated; each time step the probability for decay is calculated from the width of the resonance; a random number is generated and compared to the decay probability, and if it exceeded by the decay probability the resonance is said to decay. Then the program calls routines which calculate the momenta of the products of the decay. Since the product of resonance decays consists of a nucleon and a pion, the exit channel of the nucleon must be checked against the occupancy of phase-space of the rest of the spin-$\frac{1}{2}$ matter of the system. This is the Pauli-blocking mentioned earlier. First the occupancy, the Wigner term f in Equation 1.3, is measured by a number between zero for no occupancy, and one for full occupancy. A random number between zero and one is generated and compared to the occupancy. If that number is less than the occupancy, the decay is disallowed, and a new baryon is chosen at random. If not, then phase-space for the nuclear matter is updated.

Assuming the particle is not a resonance, a new particle is chosen to complete the pair to be considered for collision. If the pair consists of two π-mesons or if the pair consists of a π-meson and a resonance, the collision is not allowed, and the particles go on their merry way. In addition, if the pair are separated by a distance exceeding a range of a maximum cross section (that of a π-meson and a nucleon) or if the center-of-momentum energy of the collision is less than a predetermined cut off value, the collision is disallowed and a new pair is considered. Pion-nucleon collisions result in Δ and N* resonances and the absorption of that π-meson. The cross sections of these processes were calculated according to Danielewicz [Dan91].

Nucleon-nucleon collisions dominate the aggregate of collisions and are thus very important in the dynamics of the entire system. Once certain kinematic requirements are met, such as whether the nucleons are moving toward each other, the cross section is calculated according to the Particle Data Group fit [PDG88]. Here the in-medium effects of fermionic matter on the cross section can be introduced for study. The effect is illustrated in Brückner G-matrix theory [Brü55], where certain "soft" or low-momentum processes are disallowed by the *Pauli exclusion principle.* Brückner theory forms the foundation for the on-shell propagation, ignoring the mean field, of the nucleons between collisions. In intermediate energy heavy-ion collisions, most of the nucleon collisions scatter nucleons to the outside of the initial Fermi spheres. Thus, the analogy is extended to "hard" processes in this model. Usually the form of the effect is parameterized by

$$\sigma_{nn} = \sigma_{free}(1 + \alpha\frac{\rho}{\rho_0}) \tag{1.9}$$

[Kla93], where σ_{nn} is the in-medium nucleon cross section, σ_{free} is the nucleon cross section in the vacuum, ρ is the density of matter local to the collision, ρ_0 is the density of infinite nuclear matter in the ground state, and α is a parameter between 0 and -1. Reducing the cross section makes nucleus-nucleus collisions less repulsive on average as there are fewer nucleon-nucleon collisions.

More sophisticated treatments of in-medium corrections exist. Alm,*et al.*[Alm95] used a thermodynamic T-matrix at finite temperatures to calculate the in-medium nucleon cross section. Their cross section depended upon the local values of temperature, density, collision energy and the momentum of the center-of-momentum frame of the colliding pair relative to the surrounding matter. They found an enhancement of the cross section for a local temperature of 10 MeV and local density of $0.5\rho_0$. At higher temperatures, however, a reduction was calculated. They found that the enhancement in the cross section was due to Pauli blocking in their calculations, whereas the reduction in the cross section was due to self-energy effects. Nonetheless, in BUU calculations using the cross sections of Alm,*et al.* nucleon collision rates were found to be remarkably similar to nucleon collision rates in BUU calculations using the parameterization of Klakow,*et al.*[Kla93].

More recent work by Schnell,*et al.*[Sch98], using a non-relativistic in-medium scattering matrix with a realistic inter-nucleon potential, calculated the nucleon cross section as a function of relative momentum of the colliding pair, their total momentum, local density and local temperature. They then calculate an average cross section which depends upon the energy of the scattering, the local density and local temperature. They found this average cross section to be only weakly dependent upon temperature. Their parameterization:

$$\frac{\langle\sigma\rangle}{\langle\sigma_{free}\rangle} = 1 + \alpha(E,T)\frac{\rho}{\rho_0} - \beta(E,T)(\frac{\rho}{\rho_0})^2 \tag{1.10}$$

includes a second-order correction in density, as well as a dependency in E, the scattering energy. We do not expect this new parameterization to significantly alter the single-particle observables calculated with BUU.

If the transverse separation (impact parameter) of the colliding nucleons in their center-of-momentum frame is within $\sqrt{\sigma_{nn}/\pi}$, then the possible exit channels are considered. Elastic and inelastic processes are stochastically selected according to the ratio of the scattering cross section as determined by the Particle Data Group fit [PDG88] to a maximum, low-energy ($\sqrt{s} = 1.89\,GeV/c^2$) cut-off cross section. If the two are the same, the ratio is 1 and the collision is certain to be elastic. If this ratio is less than one, then there is some chance the collision is elastic. If the collision is to be inelastic, exit channels for the Δ or N*–and π-meson if direct pion production is to be included in the model–are generated. Finally, all spin-$\frac{1}{2}$ exit states are checked for Pauli-blocking. If an exit is blocked, then the collision is disallowed, the pre-collision phase-space of the nucleons is restored and a new pair is randomly chosen. It is no surprise that most of the given computational resources are devoted to sampling the collision integral.

The geometrical arguments involved in the numerical implementation of the collision integral are tantamount to assuming the nucleons to be point-like. At distances less than a fermi, the inter-nucleon potential is very repulsive. Thus one may suggest the inclusion of this hard-sphere behavior in the scattering algorithm. Such an effort has been made by Kortemeyer,*et al.*[Kor95]. This work featured the Direct Simulation Monte Carlo approach, see Lang,*et al.*[Lan93] and Danielewicz,*et al.*[Dan91]. The hard-sphere advection gives a van der Waals behavior in the collision integral. Corrections were made to scattering probabilities. The modifications to the collision integral pushed calculated observables further from their experimental values, although it should be noted that the inclusion of in-medium corrections to the nucleon cross section would improve the results.

Phase-Space Occupancy $f(\vec{r},\vec{p})$

Measuring the occupancy of phase-space is necessary to approximately treat the *Pauli exclusion principle.* In this implementation of the BUU model, coordinate-space and phase-space densities are separately maintained. The 6-dimensional phase-space information is ingeniously stored in a character array. Storing this information in a character array minimizes the amount of memory the information consumes, although it also necessarily places a limit on the number of nucleons which may occupy a single phase-space element. Characters are represented by 8-digit binary numbers giving a total of $2^8 = 256$ permutations. Thus, 256 is the maximum number of nucleons which may occupy a given cell in phase-space. Normally, *a priori* knowledge of the size of the collision volume and its distribution in momentum-space allows adjustment of the lattice parameters as long as the volume element (cell) $dx\,dy\,dz\,dp_x\,dp_y\,dp_z$ remains h^3. Here the coordinate-space lattice parameter is 2.73 fm and that for the momentum-space lattice is 0.18 GeV/c.

The size of a cell comes from considerations of low-energy theories of the nucleus and the Wigner transform, a classical analog of which is used here. Wigner functions composed from quantum wave packets are not positive-definite. In an effort to remove these non-classical negative values, a Gaussian smoothing is often applied with a length parameter of h^3, and so this is taken to be a proper lattice parameter for phase-space.

Within the program whenever it is necessary to check the occupancy of a spin-$\frac{1}{2}$ exit channel, the index of the nucleon is passed to a routine which returns the occupancy of phase-space in that nucleon's neighborhood. First the nucleon's position and momenta are extracted from the appropriate arrays and are decretized on lattices for momentum- and coordinate-space. These become the indices of the phase-space lattice site. A linear interpolation is then executed on the 2^6 nearest neighbors. The result is normalized to the volume element, spin and iso-spin degeneracies, and the number of parallel members nucleus-nucleus events in the ensemble. In the end a number between 0 and 1 is returned, the measure of the occupancy of that region of phase-space.

1.4 Summary

The BUU formalism forms the foundation for one of the most successful numerical approaches to relativistic heavy-ion theory. The truncation of the BBGKY[Won77, Bau86a] hierarchy, from which BUU model can be derived, relieves one of the huge combinatorial burden that the full N-body calculation carries.

However, what one gains in calculability, one loses in physical completeness. In part this means the systems modeled do not condense into the highly correlated shell-like structures found in low energy nuclear excitations. Nor are quark and gluon degrees of freedom explored at high energies. These limitations place upper and lower limits in energy upon the viability of the model. Finally, the system's relativistic nature is only partially addressed; relativistic kinematic are used, but fields are propagated with infinite velocity.

The strong anti-correlation due to the *Pauli exclusion principle* is approximated in parts of the model. However, nearly all dynamical and kinematical elements must include consideration of Pauli-blocking.

The inter-nucleon potential is split among two mechanisms: hard scattering for modeling the strong, repulsive, high-momentum processes, and a nuclear mean field for soft, low-momentum processes.

In spite of these approximations, the BUU model has been successful in providing science insight into the rich dynamics of relativistic heavy-ion collisions.

Chapter 2 describes two directed, collective observables which can be used to discriminate among the various sets of model parameters of BUU. Presented is the distribution of the average, in-plane, transverse momentum in rapidity, the derivative of which at mid-rapidity is called the flow of the collision. The other is the distribution of the total in-plane, transverse momentum in rapidity. Both of these observables are sensitive to the dynamics of the collision and, in turn, sensitive to the model parameters of BUU.

Chapter 2

Collective Phenomena

Studying the behavior of groups of nucleons liberated in heavy-ion collisions gives one a peek into the collective behavior of large amounts of nuclear matter. Today we use several experimental observables of collective phenomena to characterize various equations of state. They are, to one degree or another, sensitive to important elements of the model: compressibility, in-medium effects, momentum dependence. And the search for cleaner probes continues. In this chapter some of the most often-used observables in heavy-ion physics are presented in addition to the influence the equations of state have on their values.

2.1 A Picture of the Nucleus-Nucleus Collision from BUU

At intermediate collision energies, the nucleus behaves somewhat like a droplet of liquid; as it collides with another nucleus, its shape distorts from an initial sphere to an ellipsoid, compressional energy builds as some of the beam energy is converted, primarily through hard nucleon collisions, to locally random or thermal energy. Some of the matter is stopped, or nearly so, in the center-of-momentum frame of the nuclei and forms a rotated elliptical hard core.

The evolution of the phase-space of a ^{197}Au + ^{197}Au collision with a beam energy of 50 MeV/A is shown in Figures 2.1, 2.2, 2.3, and 2.4. The first is a series of projections of the momentum space of 10% of the nucleons of the entire ensemble every 10 fm/c. As one looks at each panel, one sees the P_x-P_z plane, where the z-direction denotes the beam direction. The first panel in the upper left corner shows the initial state of the nuclei: two Fermi spheres the centers of which are separated by beam momentum. Here the two spheres are not completely separated since the radius of each sphere is only about 267 MeV/c whereas the beam momentum per nucleon is only 310 MeV/c. As time advances from the upper left corner down the page, the initial Fermi spheres dissolve as the beam momentum is thermalized. Nearly complete thermalization results in the final panel.

Figure 2.2 shows the configuration-space projection of the same nucleons. Here the view is onto the reaction plane, which is defined by the centers of the nuclei and the impact vector. Again the z-direction is collinear with the beam. Beginning with the initial state in the upper left corner and progressing in time down the page, one sees the well-defined spherical nuclei approach each other. By about 90 fm/c the system is near maximum compression. Here a large fraction of the beam energy has been converted, through hard scattering, repulsive contributions from the nuclear mean field, and the Coulomb field, into potential energy. The very next panel shows the evidence of the release of this pent-up potential. Most of the nucleons have left the calculation volume. The system becomes quite diffuse. This violence is typical of central (zero impact parameter) collisions.

The amount of the initial longitudinal momentum transformed into momentum perpendicular to the beam is often used as a means of characterizing the impact parameter of the collision. This is accomplished with the help of theoretical models, like BUU, wherein one has *a priori* knowledge of the impact parameter. A mapping

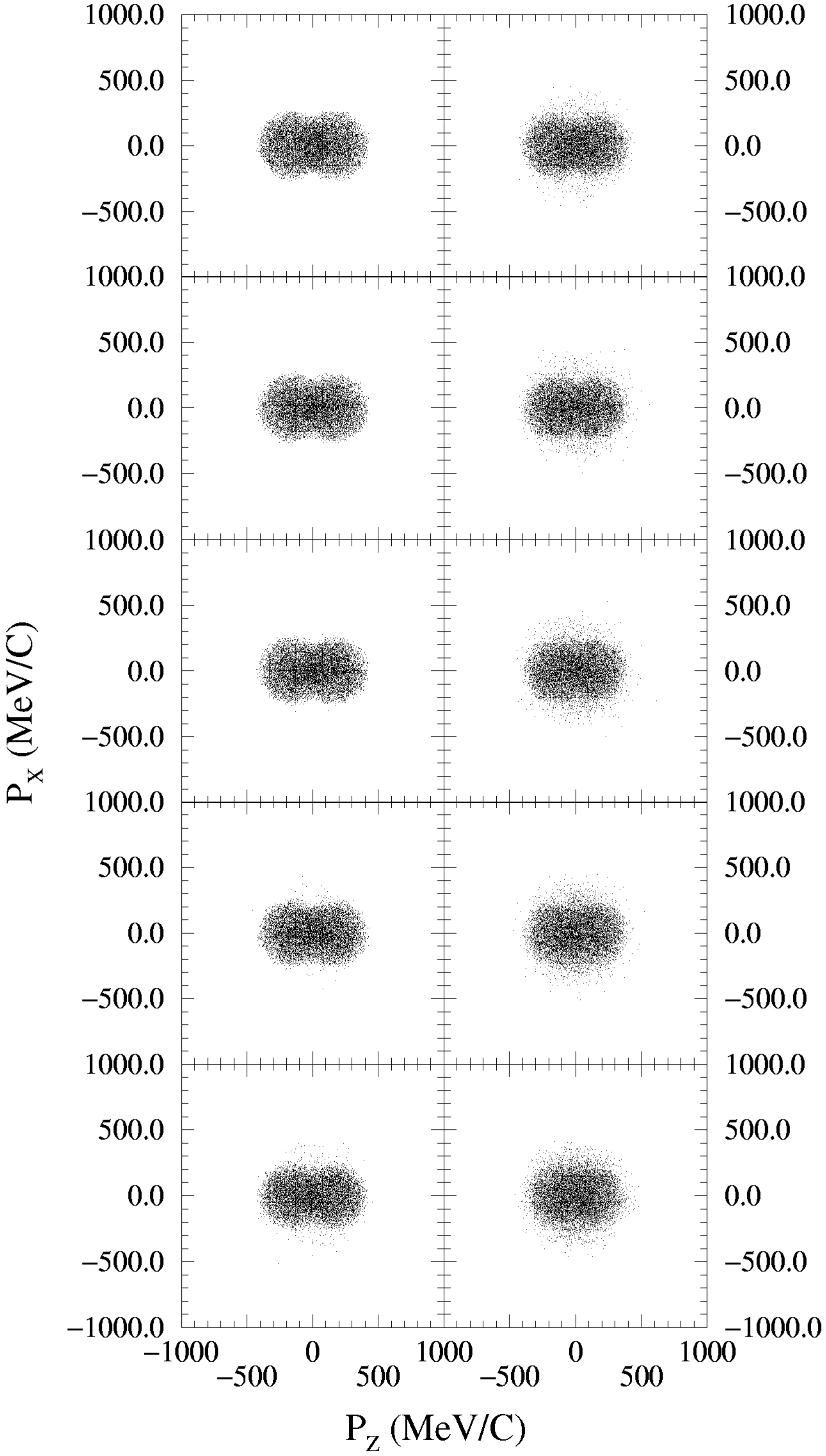

Figure 2.1: Momentum-space projection upon the P_x-P_z plane for ^{197}Au + ^{197}Au reaction at 50 MeV/A. Impact parameter is zero, soft (compressibility = 200 MeV) mean field and vacuum nucleon cross sections were used. Each panel is separated by 10 fm/c. Initial state is the upper left panel, and time passes from top to bottom. final-state is the lower right panel.

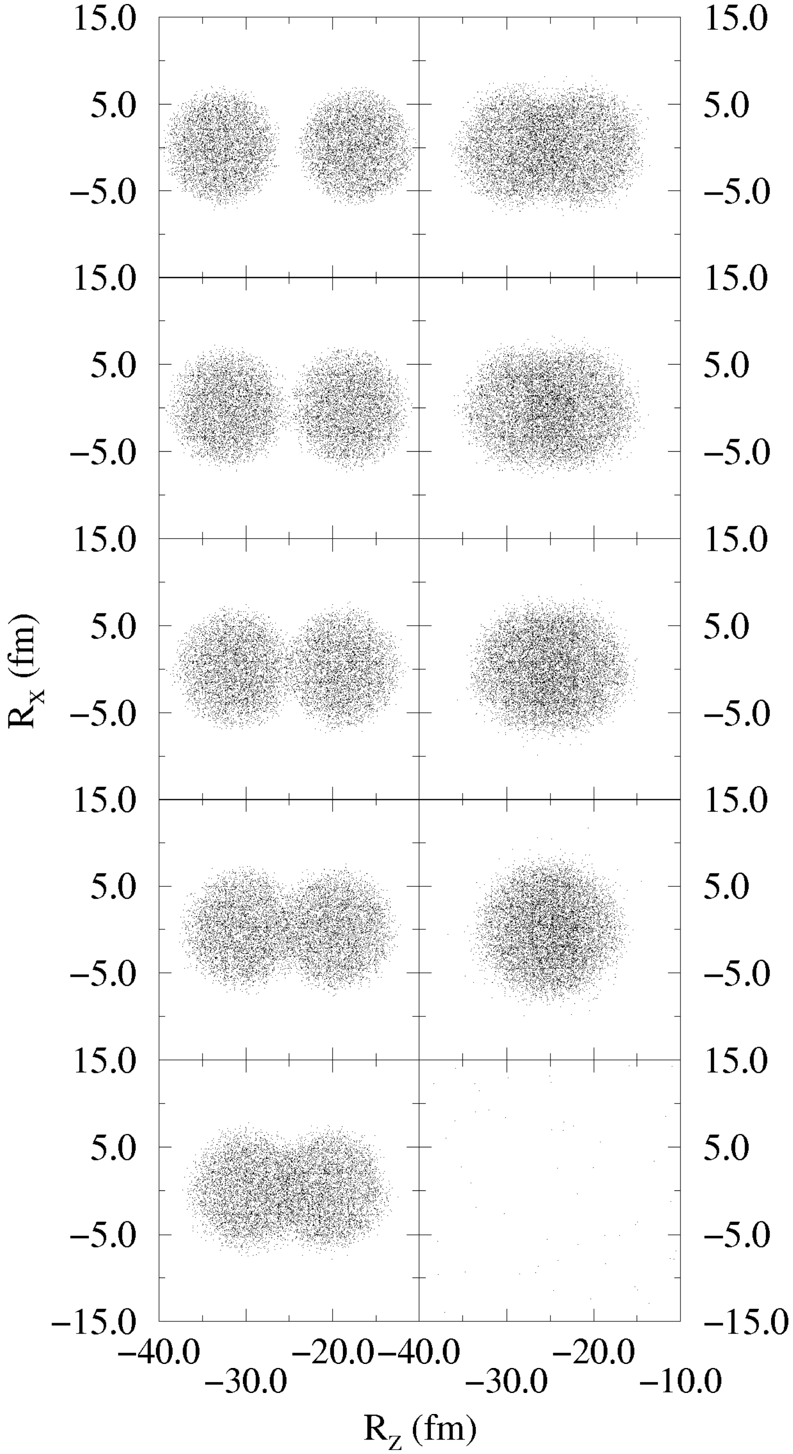

Figure 2.2: Configuration-space projection upon the reaction plane for ^{197}Au + ^{197}Au reaction at 50 MeV/A. Impact parameter is zero, soft (compressibility = 200 MeV) mean field and vacuum nucleon cross sections were used. Each panel is separated by 10 fm/c. Initial state is the upper left panel, and time passes from top to bottom. final-state is the lower right panel.

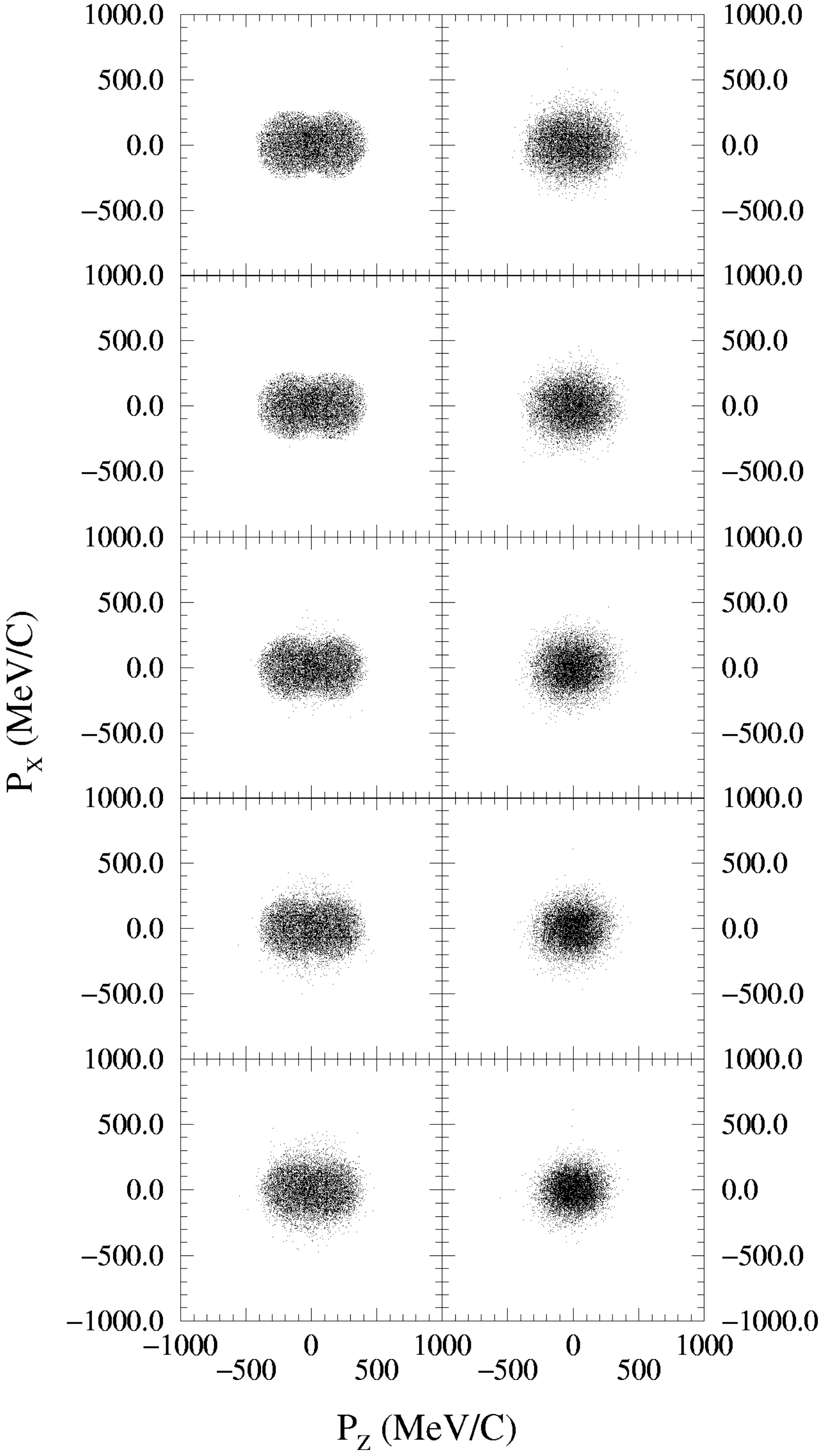

Figure 2.3: Momentum-space projection upon the P_x-P_z plane for ^{197}Au + ^{197}Au reaction at 50 MeV/A. Impact parameter is 3.5 fm, soft (compressibility = 200 MeV) mean field and vacuum nucleon cross sections were used. Each panel is separated by 10 fm/c. Initial state is the upper left panel, and time passes from top to bottom. final-state is the lower right panel.

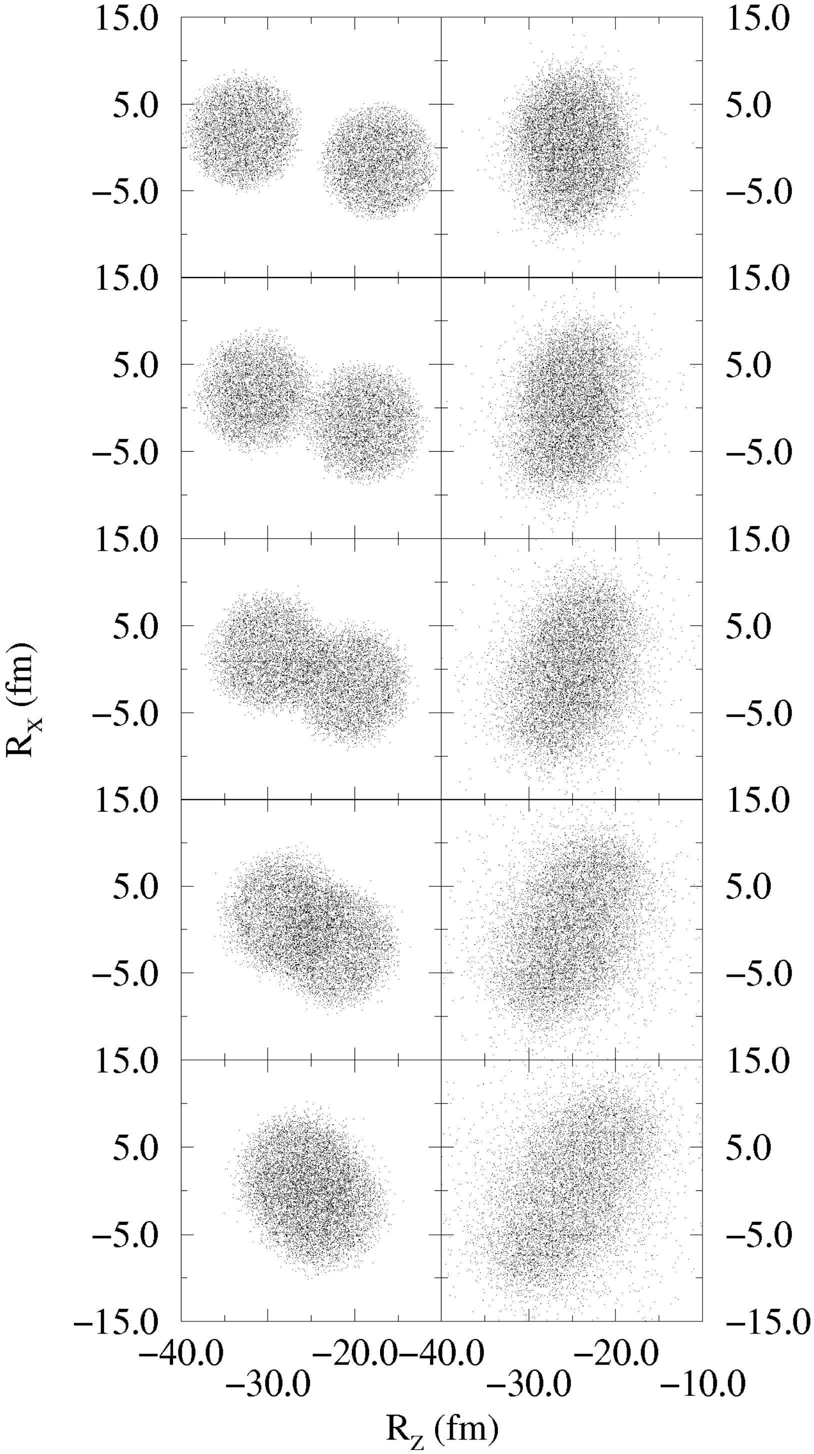

Figure 2.4: Configuration-space projection upon the reaction plane for ^{197}Au + ^{197}Au reaction at 50 MeV/A. Impact parameter is 3.5 fm soft (compressibility = 200 MeV) mean field and vacuum nucleon cross sections were used. Each panel is separated by 10 fm/c. Initial state is the upper left panel, and time passes from top to bottom. final-state is the lower right panel.

can then be constructed from the theoretical calculations of the transverse momentum in the final state. Other observables may be used as well.

Figure 2.3 is the momentum-space projection for a ^{197}Au + ^{197}Au collision with a 3.5 fm impact parameter. One can immediately see that the momentum space distribution appears qualitatively similar to that of the central collision, Figure 2.1. The next section will address some of the differences between central collisions and the far more common off-center collisions. The initial state consists of two Fermi spheres not quite separated by beam momentum, and the final-state appears well thermalized at 100 fm/c.

The evolution of the configuration-space distribution is strikingly different. Figure 2.4 shows a more complex picture. The first panel shows two distinct nuclei offset by the impact parameter. In the next few panels the two nuclei touch and their constituent nucleons collide. These nucleon collisions begin to transform the initial low temperature system into a hot compound nucleus. This nucleus is unstable. An elliptical distribution is quickly formed and the initial angular momentum (there was none in the previous example) results in a rotation of this ellipsoid. The rotation is complete in final panel after which residual beam momentum tears the system apart. In experiments the remnants end up in the detectors.

2.2 Directed Transverse Flow

Collisions with non-zero impact parameter develop differently from central collisions. Here the symmetry of the central events is broken. Of course in experiments one cannot choose the impact parameter, and selecting on impact parameter is not a trivial exercise. All events will have non-zero impact parameters.

Figures 2.5 and 2.6 are good examples of the evolution of a heavy-ion collision and more typical of what is observed in experiments. The momentum-space distribution of the nucleons is more vividly realized here because the beam energy of 500 MeV/A well separates the Fermi spheres. And, unlike the lower energy collision in Figure 2.3, one can clearly see the characteristic ellipsoidal distribution of momentum in the final state. With a beam energy of only 50 MeV/A the ellipsoid is too small to reach beyond the thermal sphere in Figure 2.3.

One can get a feel for the development of the deflection of matter in this off center collision. Figure 2.6 shows the configuration-space development of the collision. Notice the sigmoidal "S"- shape of the distribution in the third panel (t=20 fm/c). The sigmoid is an intermediate form which consists of spectator matter (nucleons which have not significantly scattered) in the periphery, and participant matter (nucleons which have experienced several hard scattering events) occupying the volume common to both nuclei. The participant matter is significantly slowed[Bau88] and compressed. The initial angular momentum carries the spectator matter into the forward and backward hemispheres in the center-of-momentum frame (t=30 and 40 fm/c) and rotates the compressed core. The ellipsoidal distribution follows from the expansion of the compressed participant matter and the deflection of the spectator matter off of the core, both along the major axis of the ellipsoid. Notice that in later times the system is very diffuse, with only a few of the original nucleons remaining. This is a testament to the release of the pent-up compressional energy in the system. The matter expands quickly, and much of it has left the calculation volume.

In 1985 Danielewicz and Odyniec[Dan85] proposed a new observable: average transverse in-plane momentum as a function of rapidity. To calculate this observable from experimental data, one needs to establish the reaction plane. They proposed the vector:

$$\mathbf{Q} = \sum_{\nu=1}^{M} \omega_\nu \mathbf{p}_\nu^{\perp}, \tag{2.1}$$

where ν is the particle index, $\mathbf{p}_\nu^{\perp}$ is the transverse momentum of the particle, ω_ν is a weight for the particle. Usually ω_ν is -1 for $y_\nu < y_{C.O.M.}$, that is backward going in the center-of-momentum frame, and is +1 for $y_\nu > y_{C.O.M.}$. Thus for particles deflected to positive rapidities, positive-x in Figure 2.6, their transverse momentum makes a positive contribution to **Q**. Those deflected to the negative rapidities will get a negative weight. **Q** is used to determine the reaction plane in experimentally measured transverse momentum distributions. With an estimation of the reaction plane, one can calculate the average per nucleon, in-plane, transverse momentum as a function of rapidity. Figure is such a distribution for the ^{197}Au + ^{197}Au collisions in Figures 2.5 and 2.6. The slope of the curve at mid-rapidity is the flow[Dan85, Ogi89] for the system.

Figure 2.7 shows a projection of the momentum-space distribution of a ^{197}Au + ^{197}Au collision at 500 MeV/A and an impact parameter of 3.5 fm. Unlike Figure 2.5 this calculation used the "stiff" mean field. The two momentum distributions are similar. Both exhibit the ellipsoidal shape of a system under directed flow.

The observable "flow" is defined as:

$$\left.\frac{d\langle p_x\rangle}{dy}\right|_{y=0},$$

where $\langle p_x\rangle$ is

$$\frac{\sum_{\nu(y)}^{N(y)} p_x^\nu}{N(y)},$$

$N(y)$ is the number of fragments (protons in this work) with rapidity y, and $\nu(y)$ is the particle index.

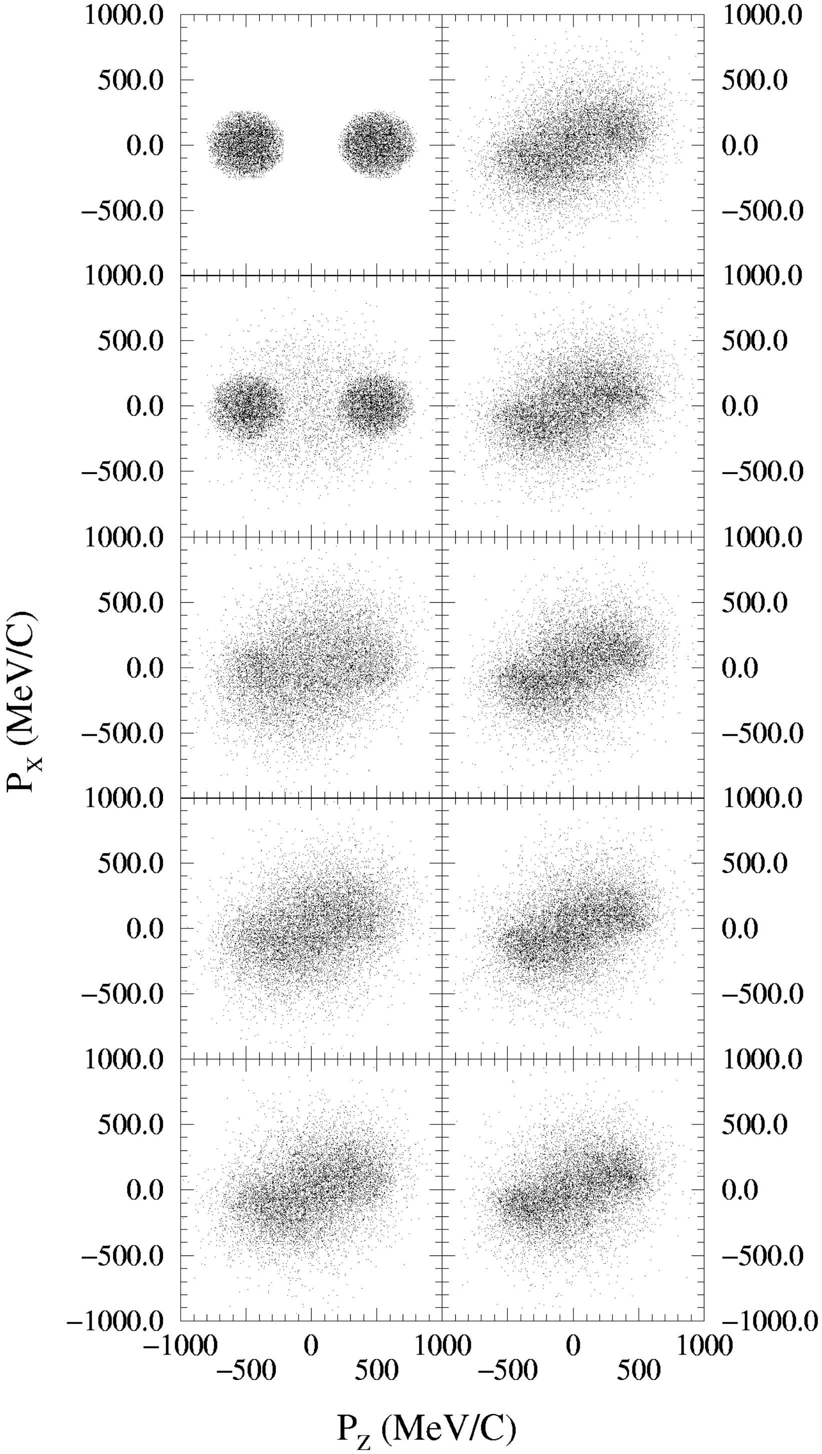

Figure 2.5: Momentum-space projection upon the P_x-P_z plane for ^{197}Au + ^{197}Au reaction at 500 MeV/A. Impact parameter is 3.5 fm. Each panel is separated by 10 fm/c; soft (compressibility = 200 MeV) mean field and vacuum nucleon cross sections were used. Initial state is the upper left panel, and time passes from top to bottom. final-state is the lower right panel.

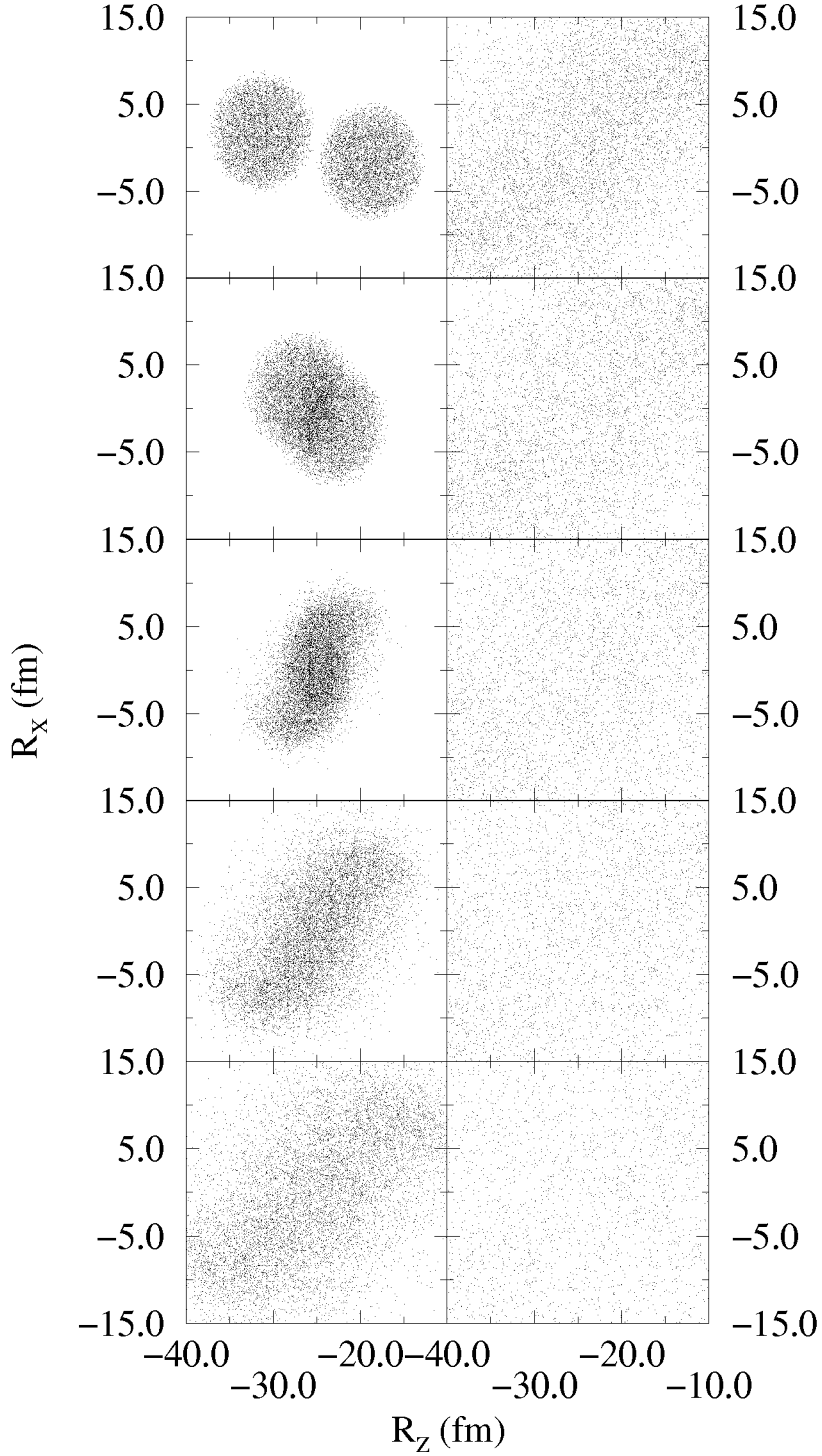

Figure 2.6: Configuration-space projection upon the reaction plane for ^{197}Au + ^{197}Au reaction at 500 MeV/A. Impact parameter is 3.5 fm, soft (compressibility = 200 MeV) mean field and vacuum nucleon cross sections were used. Each panel is separated by 10 fm/c. Initial state is the upper left panel, and time passes from top to bottom. final-state is the lower right panel.

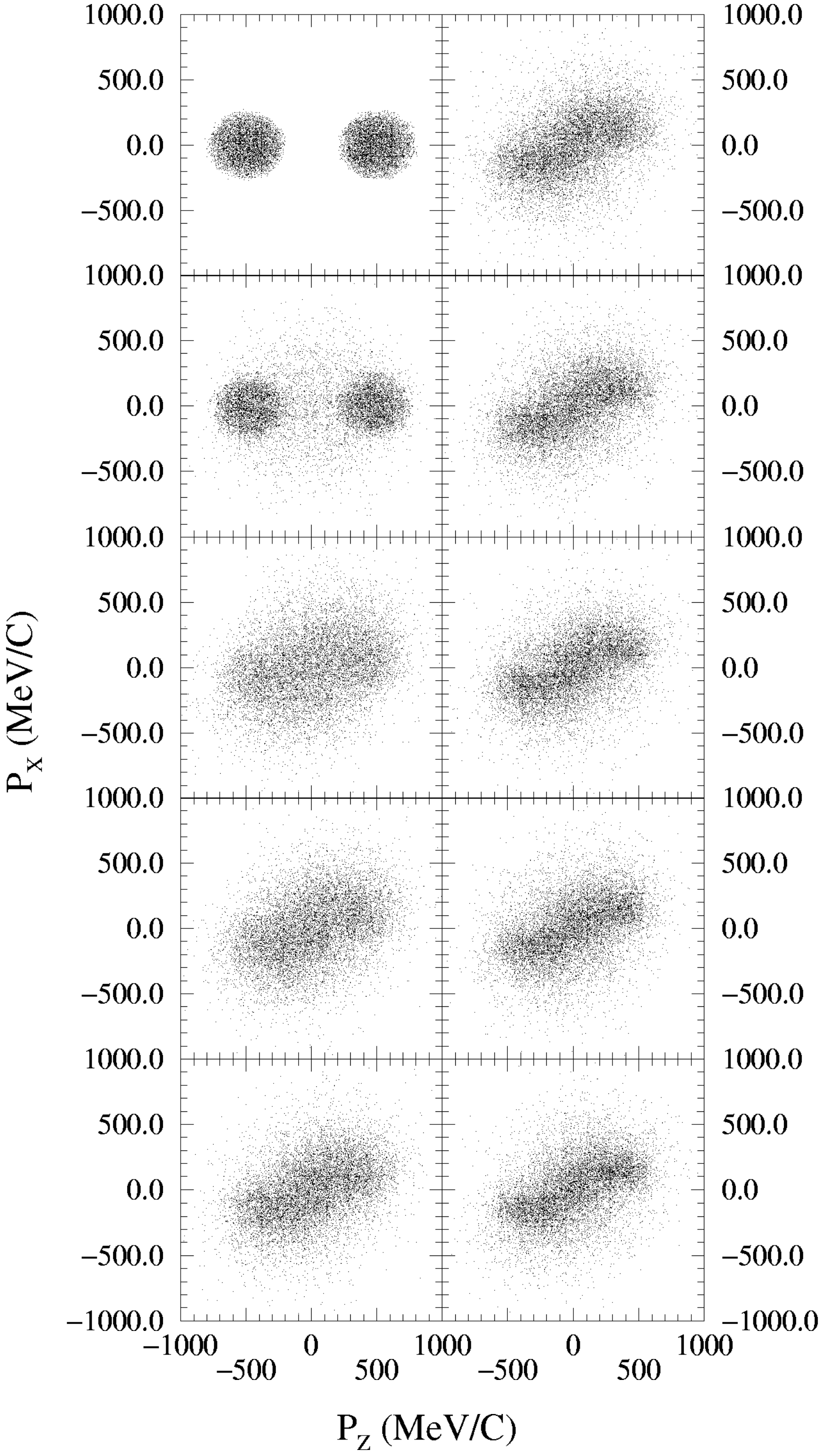

Figure 2.7: Momentum-space projection upon the P_x-P_z plane for ^{197}Au + ^{197}Au reaction at 500 MeV/A. Impact parameter is 3.5 fm, stiff (compressibility = 380 MeV) mean field and vacuum nucleon cross sections were used. Each panel is separated by 10 fm/c. Initial state is the upper left panel, and time passes from top to bottom. final-state is the lower right panel.

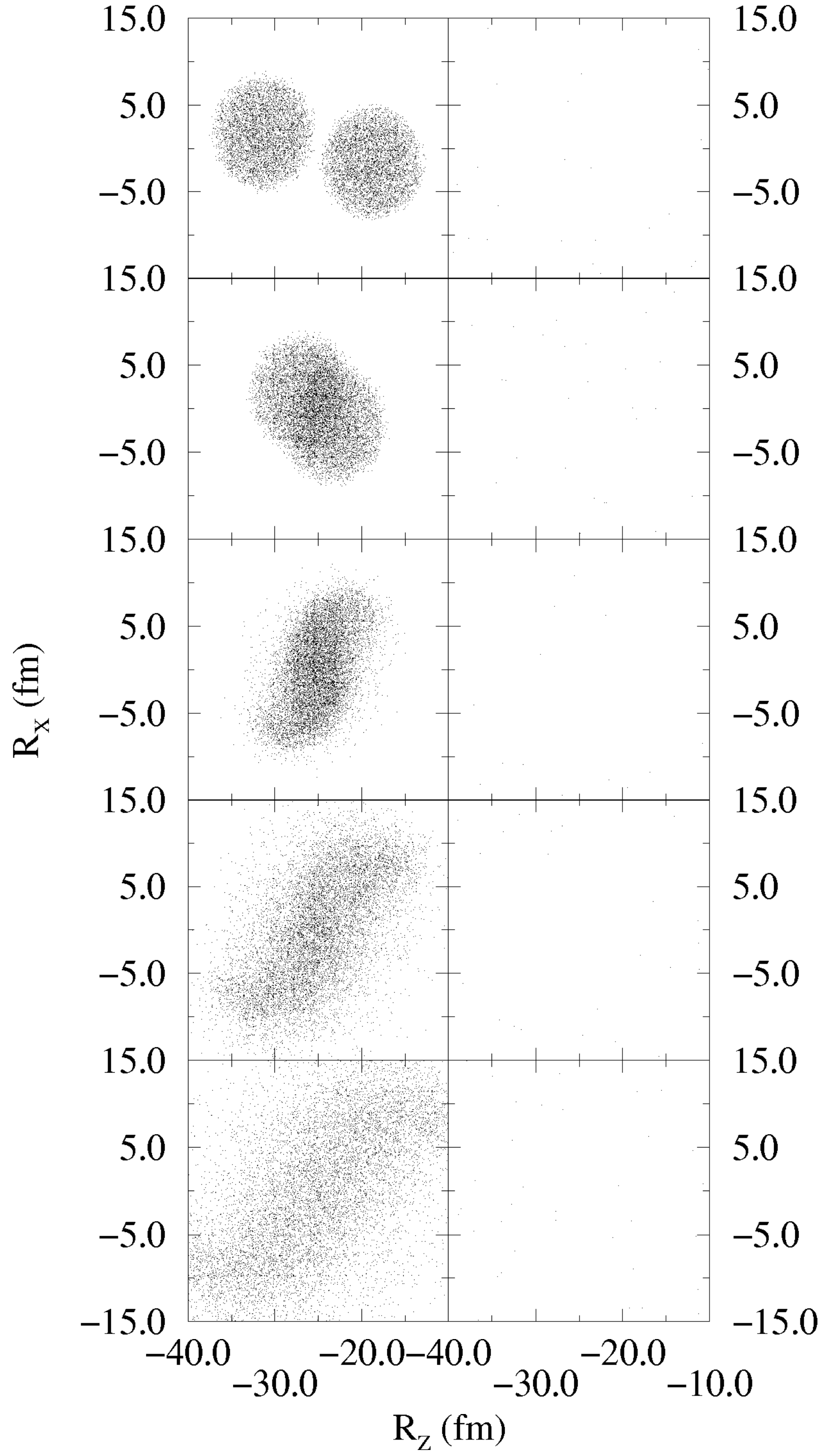

Figure 2.8: Configuration-space projection upon the reaction plane for ^{197}Au + ^{197}Au reaction at 500 MeV/A. Impact parameter is 3.5 fm, stiff (compressibility = 380 MeV) mean field and vacuum nucleon cross sections were used. Each panel is separated by 10 fm/c. Initial state is the upper left panel, and time passes from top to bottom. final-state is the lower right panel.

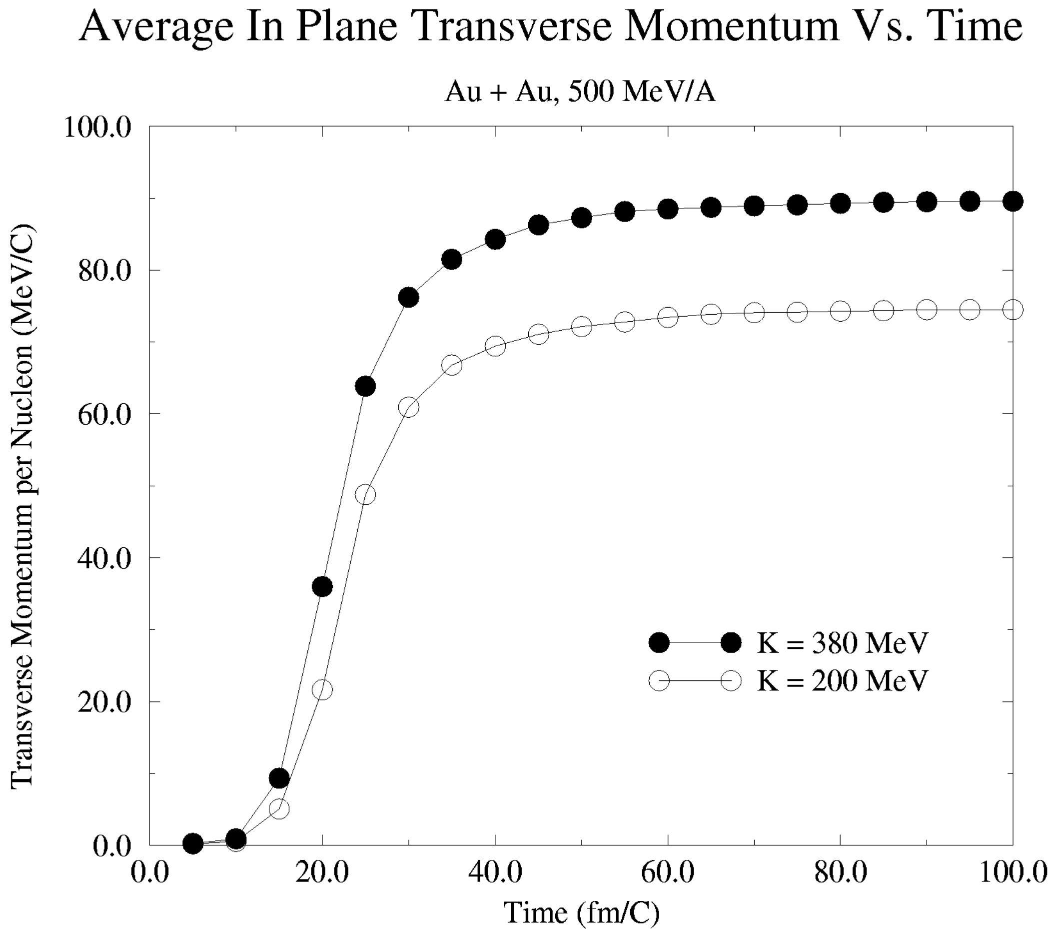

Figure 2.9: Evolution of the in-plane, transverse momentum for forward-going nucleons. Impact parameter is 3.5 fm. Two different mean fields were used, as indicated.

Figure 2.8 shows a projection of the configuration-space distribution of the same collision as in Figure 2.7. Contrast this with Figure 2.6. The two collisions look the same until about 50 fm/c where the calculations using the stiff mean field and the soft mean field diverge. The stiff mean field is more efficient in converting the beam energy into transverse degrees of freedom. The diffuse appearance of the latter stages of the calculation in Figure 2.7 bears witness to the nucleons leaving the calculation volume.

The time development of the system using different nuclear mean fields is illustrated in Figure 2.9. Notice that the more repulsive field converts more of the beam

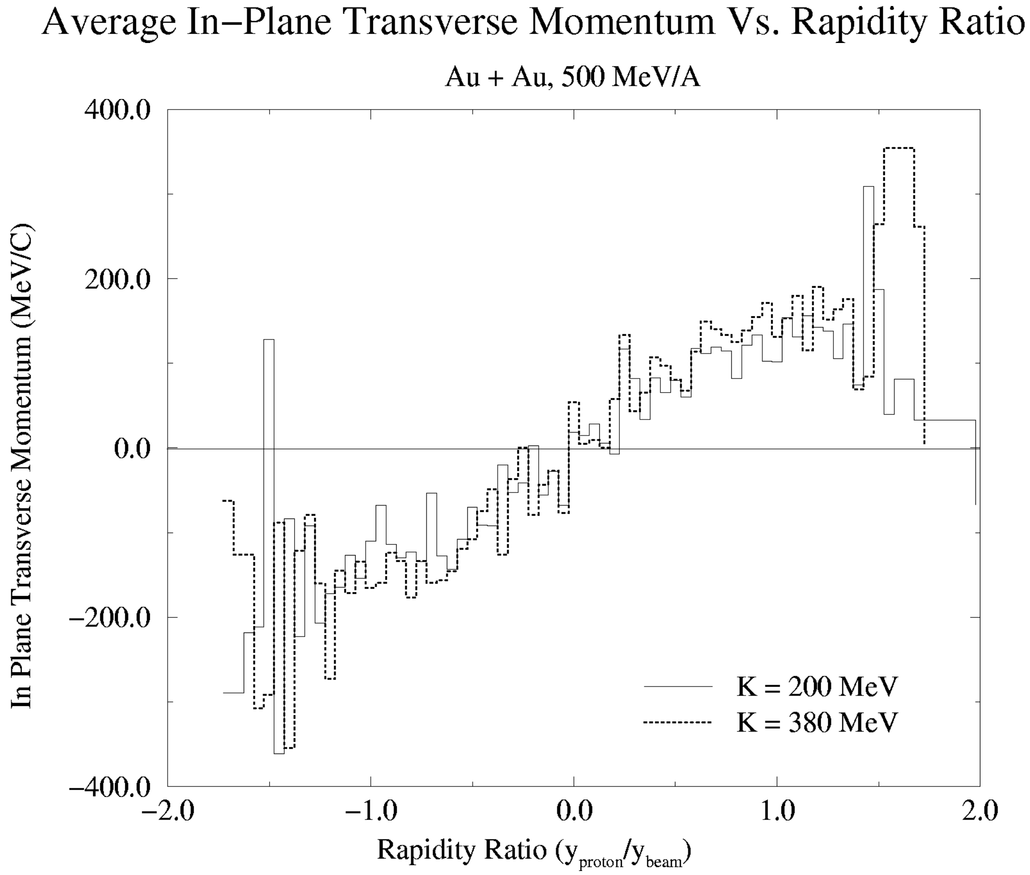

Figure 2.10: Average in-plane, transverse momentum versus reduced rapidity. The system is ^{197}Au + ^{197}Au at 500 MeV/A, impact parameter is 3.5 fm. Two mean fields were used, as indicated.

momentum to transverse momentum than the soft mean field. The slopes of the plots of Figure 2.10 are the flows of the two calculations. The stiff mean field yielded a flow of 225±6 MeV/c whereas the soft mean field yielded a flow of 172±6 MeV/c. A χ^2-minimization of a straight line was applied to the region near mid rapidity.

2.3 Impact Parameter Dependence of Flow for Momentum-Dependent and Momentum-Independent Nuclear Mean Fields

The inter-nucleon interaction is in general momentum dependent[Gale87, Gale90]. This stems primarily from the Brükner treatment of the behavior of nucleons in nuclear matter and non-local effects from nucleon-nucleus potential scattering[Gale90]. Soft or low-momentum transfer interactions are blocked by Fermi terms in the scattering equation. On average, nucleons streaming into hot, well-thermalized regions of the collision volume are blocked from scattering into these regions. This makes the bulk dynamics more repulsive on average. In the BUU model used here, the momentum-dependent of mean field of Welke, *et al.*[Wel88] is used:

$$U(\rho,\vec{p}) = A\left(\frac{\rho}{\rho_0}\right) + B\left(\frac{\rho}{\rho_0}\right)^{\sigma} + \frac{C}{\rho_0}\int d^3p'\frac{f(\vec{r},\vec{p}\,')}{1+\left(\frac{\vec{p}-\vec{p}\,'}{\Lambda}\right)^2} \tag{2.2}$$

The mean field can be modeled with various combinations of force parameters leading to different compressibilities in addition to toggling the momentum dependence. Values for the parameters in Equation 2.2 are shown in Table 2.1.

For most collisions the addition of the momentum dependence in the mean field yields more repulsive behavoir overall. Figure 2.12 shows flow values calculated for

EOS	A (GeV)	B (GeV)	σ	C (GeV)	Λ (GeV/c)	ρ_0
Soft	−0.109	0.082	7/6	0	–	0.168
Stiff	−0.062	0.03525	2	0	–	0.168
Soft $\vec{p}$	−0.11044	0.1409	1.24	−0.06495	0.416	0.168
Stiff $\vec{p}$	−0.0589	0.03621	2.45	−0.06591	0.416	0.168

Table 2.1: The constants in used in the nuclear mean field. Note that “soft” refers to a compressibility K of 215 MeV and “stiff” refers to a compressibility of 380 MeV for the momentum-dependent mean fields, whereas “soft” refers to a compressibility K of 200 MeV and “stiff” refers to a compressibility of 380 MeV for the momentum-independent mean fields.

^{197}Au on ^{197}Au at 400 MeV/A (upper panel) and 200 MeV/A (lower panel). The calculations used an in-medium nucleon cross section reduction factor of 20%, and the compressibility K was fixed at 200 MeV for all calculations.

Notice that for all but the smallest impact parameters, the flow values are larger for calculations using the momentum-dependent mean field than those for calculations using the momentum-independent mean field. However, for the ^{197}Au on ^{197}Au collision at 200 MeV/A, something unexpected occurs at the lowest impact paramters: the momentum-independent mean field produces a larger flow than does the momentum-dependent mean field.

This effect was first brought to our attention during calculations of ^{84}Kr on ^{197}Au at 200 MeV/A, which appear in work by M. J. Huang, *et al.*[Hua96]. Figure 2.11 shows flow results from BUU calculations compared with experimental data. There the impact-parameter-averaged, filtered flow values for momentum-independent mean fields were larger than those for momentum-dependent mean fields. The trend was reversed at an impact parameter of about 4 fm.

Why is this so? What mechanism is responsible for this counter-intuitive result? Is there an experimental observable which may be more sensitive to this effect and

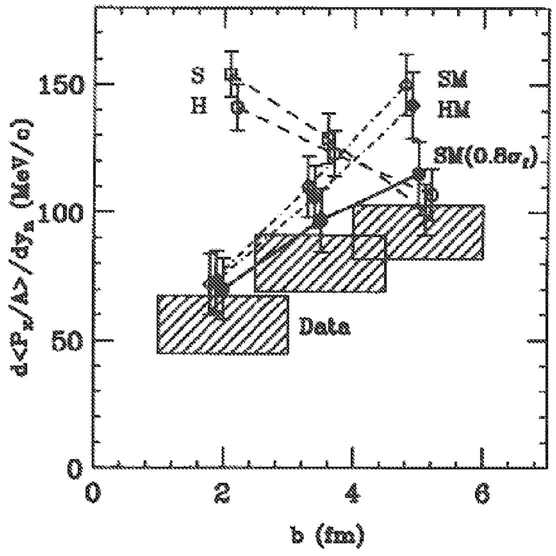

Figure 2.11: Flow results from M. J. Huang, *et al.*[Hua96]. In the Figure experimental data are the cross-hatched regions, the rest are calculated flow values with detector acceptances. "S" and "H" refer to the soft, momentum-independent and hard, momentum-independent mean fields, respectively. "SM" and "HM" refer to soft, momentum-dependent and hard, momentum-dependent mean fields, respectively. The BUU results denoted by "$(0.8\sigma_{\text{free}})$" were calculated with a 20% reduction in the free nucleon-nucleon cross section.

thus may be used to discriminate among the model parameters of BUU? The following will attempt to answer these questions.

2.3.1 The Development of Density in Time

In order to give the reader a sense of the differences in the evolution of reactions using the momentum-dependent mean field and reactions using the momentum-independent mean field, Figures 2.13–2.24 were developed. These Figures show the lab-frame evolution of the nucleon density of ^{197}Au on ^{197}Au collisions in time. Each Figure shows the normalized contours of density projected onto the reaction plane. The normalization constant is ρ_0, normal nuclear density. The upper panels show the contours from calculations using the soft, momentum-independent mean field; the lower panels show the contours from calculations using the soft, momentum-dependent mean field.

All of these calculations utilized the same model parameters used to generate the flow values in Figure 2.12. The times at which the contours are extracted from the BUU calculations were selected to demonstrate the salient features of the differences between the dynamical evolution of reaction using the momentum-dependent mean field and reactions using the momentum-independent mean field.

Figures 2.13–2.16 show central ^{197}Au on ^{197}Au collisions. For time t =1.0 fm/c, one can discern the Lorentz contraction of the projectile nucleus. At this time step the upper and lower panels are almost identical. At t =5.0 fm/c, Figure 2.14, the nuclei begin to touch. Here one can just see the beginings of differences in the evolution of the systems. This is quite clear by t =10 fm/c, Figure 2.15. The neck region separating the centroids of the two nuclei are markedly different in profile; the momentum-independent calculation showing substantially steeper density gradients than the momentum-dependent calculation. As time passes the gradients in the momentum-dependent calculations mitigate. By t =60 fm/c, Figure 2.16, the systems approach thier respective final states looking remarkably similar given their previous divergent behavoir. Apparently the momentum-independent mean-field has had time to relax to the smooth, diffuse profile seen in Figure 2.16.

Figures 2.17–2.20 show density profiles for an impact paramter b =2 fm and beam energy 200 MeV/A. This is the same impact parameter wherein Figure 2.12 the momentum-dependent flow enhancement is strongest. Begining at t =1.0 fm/c the nuclei are very similar. By 10 fm/c density gradients for the two systems begin to differ. Around t =20 fm/c, Figure 2.19, the momentum-dependent calculation shows maximum compression. However, it will be about another 10 fm/c before the momentum-dependent calculation reaches maximum compression. Figure 2.20 shows the momentum-independent system near maximum compression. Note the steep gradients and the enhancement of the central density in the momentum-independent system over those of the momentum-dependent system.

As time goes on the dense central cores of both systems rotate under the influence of the cold spectator matter farthest from the beam axis. An important clue reveals itself during this phase of the evolution: the momentum-independent system is releasing its pent-up compressional energy more slowly than the momentum-dependent system. It is the timing here that is important. If a system releases the energy too early, that is, before the rotation past 90° to the beam axis, the motion of the spectator matter up and down the beam axis will be impeded. In momentum-space, where directed flow is measured, this will shift a portion of the matter closer to mid-rapidity resulting in a more spherical distribution. This appears to be the case for the momentum-dependent calculations, and could offer an explanation for the suppression of the flow.

Figures 2.21–2.24 show density profiles for ^{197}Au on ^{197}Au collisions at 400 MeV/A. At time t =1.0 fm/c one can see the pronounced Lorentz contraction of the projectile nucleus. From Figures 2.22 and 2.23 one can see that the two systems reach their respective maximum compression at roughly the same time, although it is clear that higher densities and gradients persist in the momentum-independent calculation. Substantial release of the compressional energy seems to occur when both systems have rotated past 90° to the beam axis. By 55 fm/c the two systems are similarly diffuse.

Inspection of Figures 2.13–2.24 and Equation 2.2, one gets the impression that something else in addition to the timing of the release of compressional energy may be at work. The momentum dependence in Equation 2.2 is likely to be smaller for the well-thermalized matter of the core. However, the gradients in momentum-space, which contribute to the velocity field, see Equations 1.7 and 1.8 in Chapter 1, tend to deflect the in-coming matter perpendicular to the beam axis. This would tend to reduce the oblateness of the momentum ellipsoid and lead to a general supression of the flow signal. Evidence of similar effects have been seen[Gut89, Gut90].

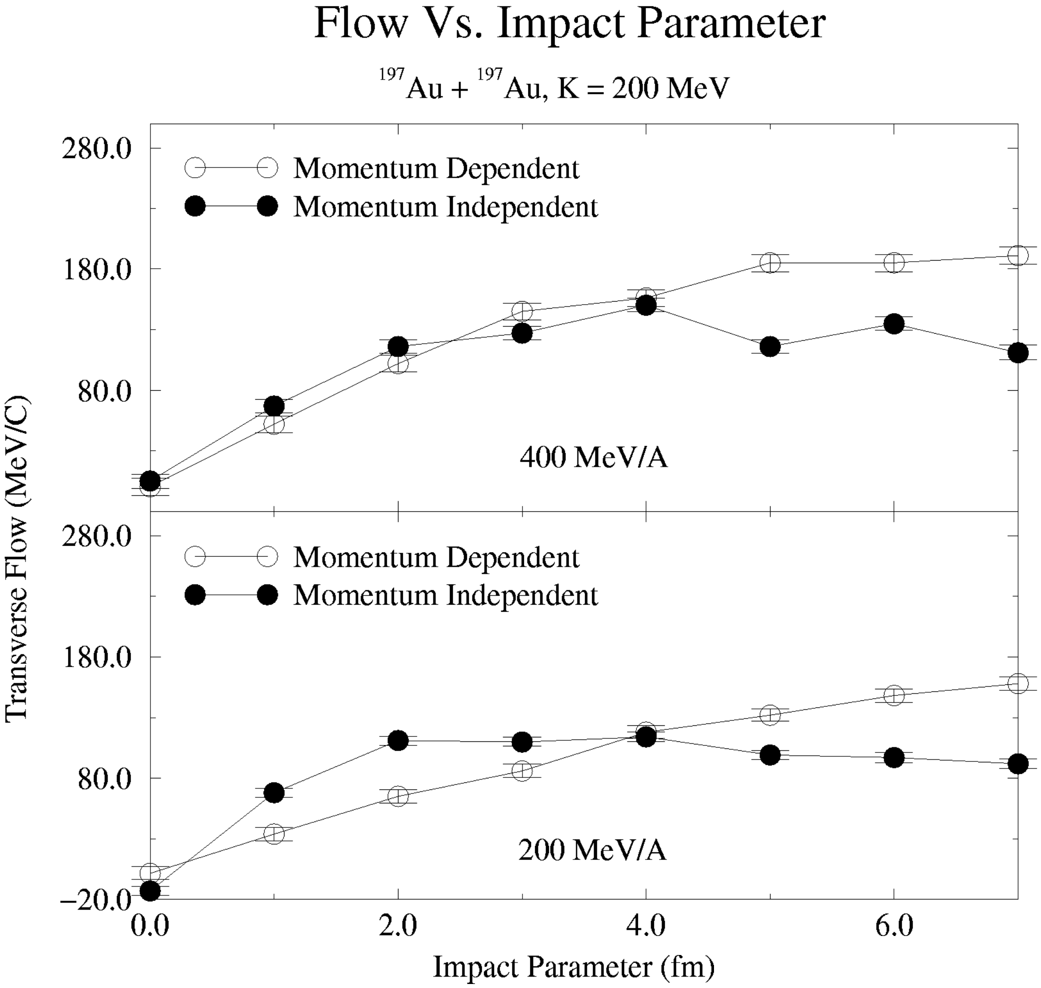

Figure 2.12: Average in-plane, transverse flow as a function of impact parameter. Upper panel shows flow calculations for ^{197}Au on ^{197}Au at 400 MeV/A for the indicated impact parameters. The lower panel shows the same observable, but for ^{197}Au on ^{197}Au at 200 MeV/A.

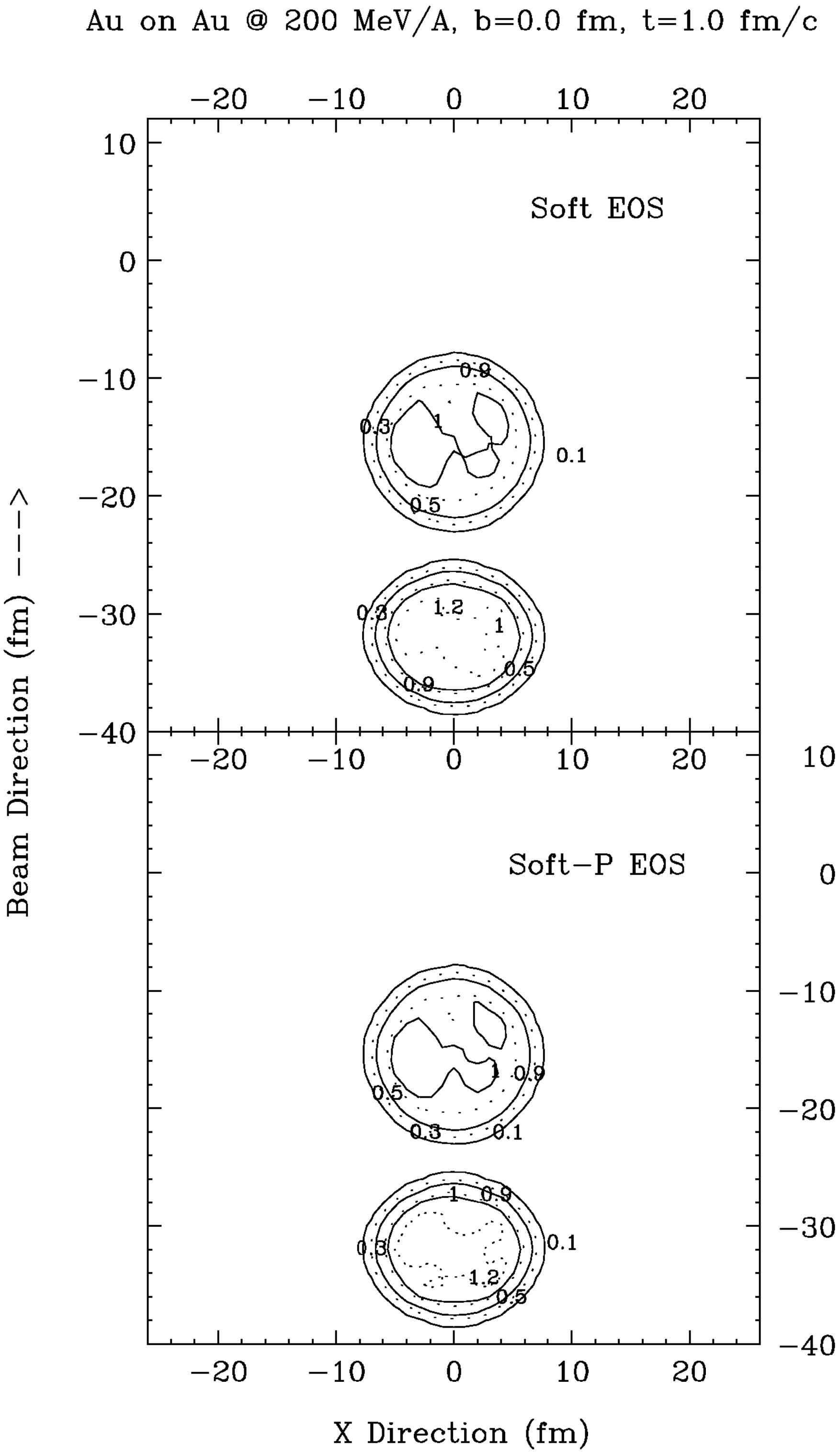

Figure 2.13: Calculated density contours. Numbers are normalized densities: ρ/ρ_0.

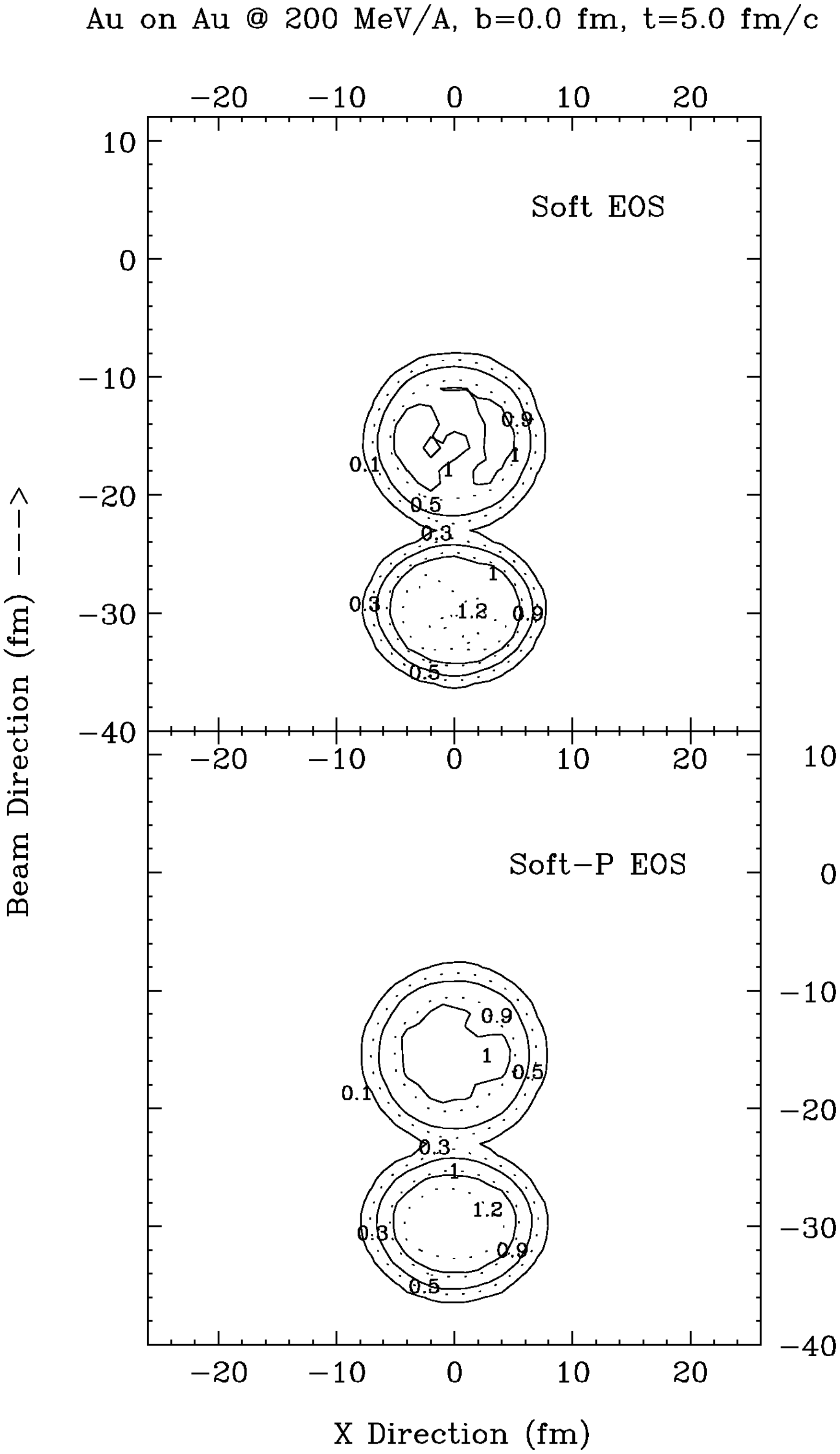

Figure 2.14: Calculated density contours. Numbers are normalized densities: ρ/ρ_0.

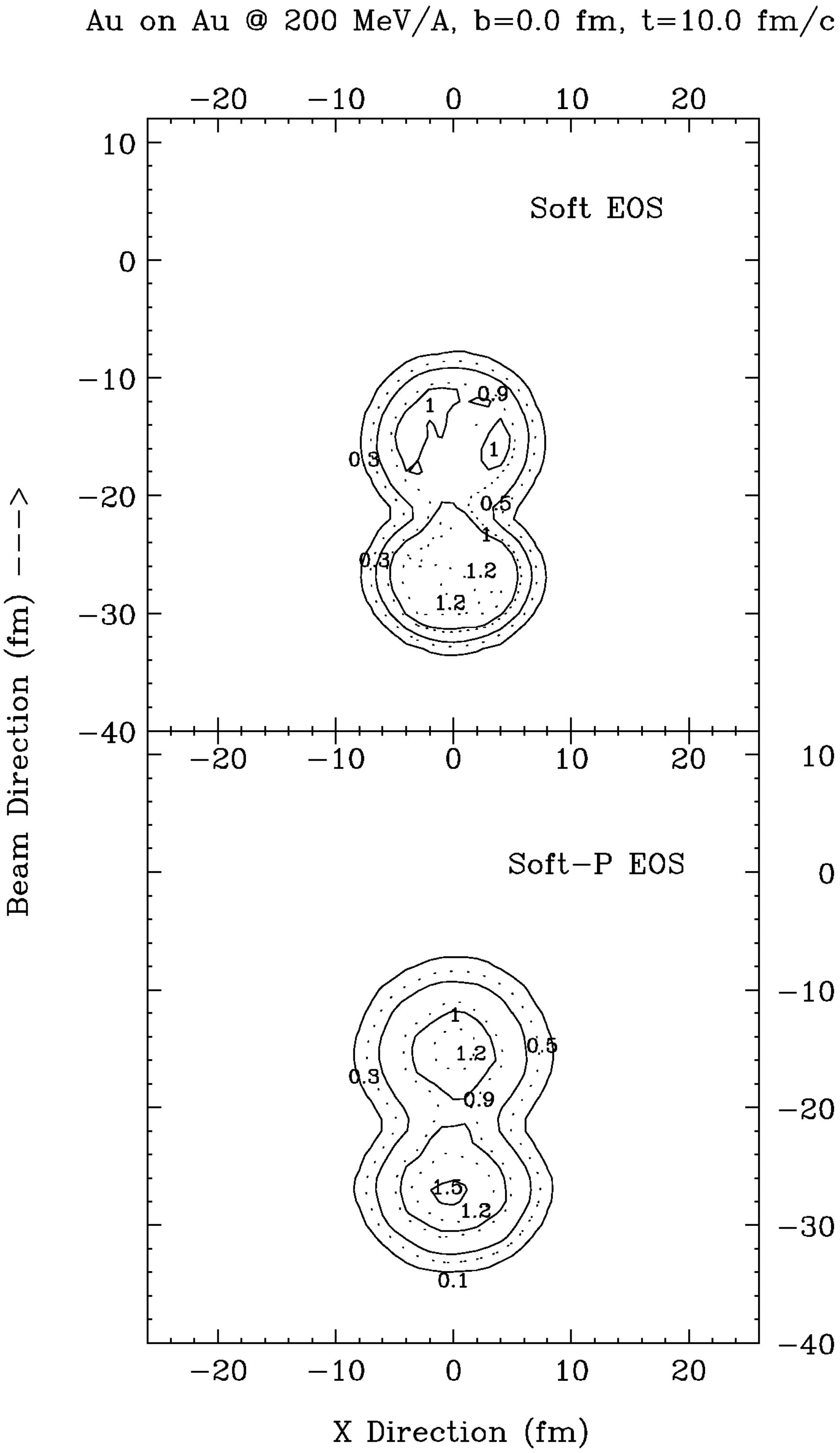

Figure 2.15: Calculated density contours. Numbers are normalized densities: ρ/ρ_0.

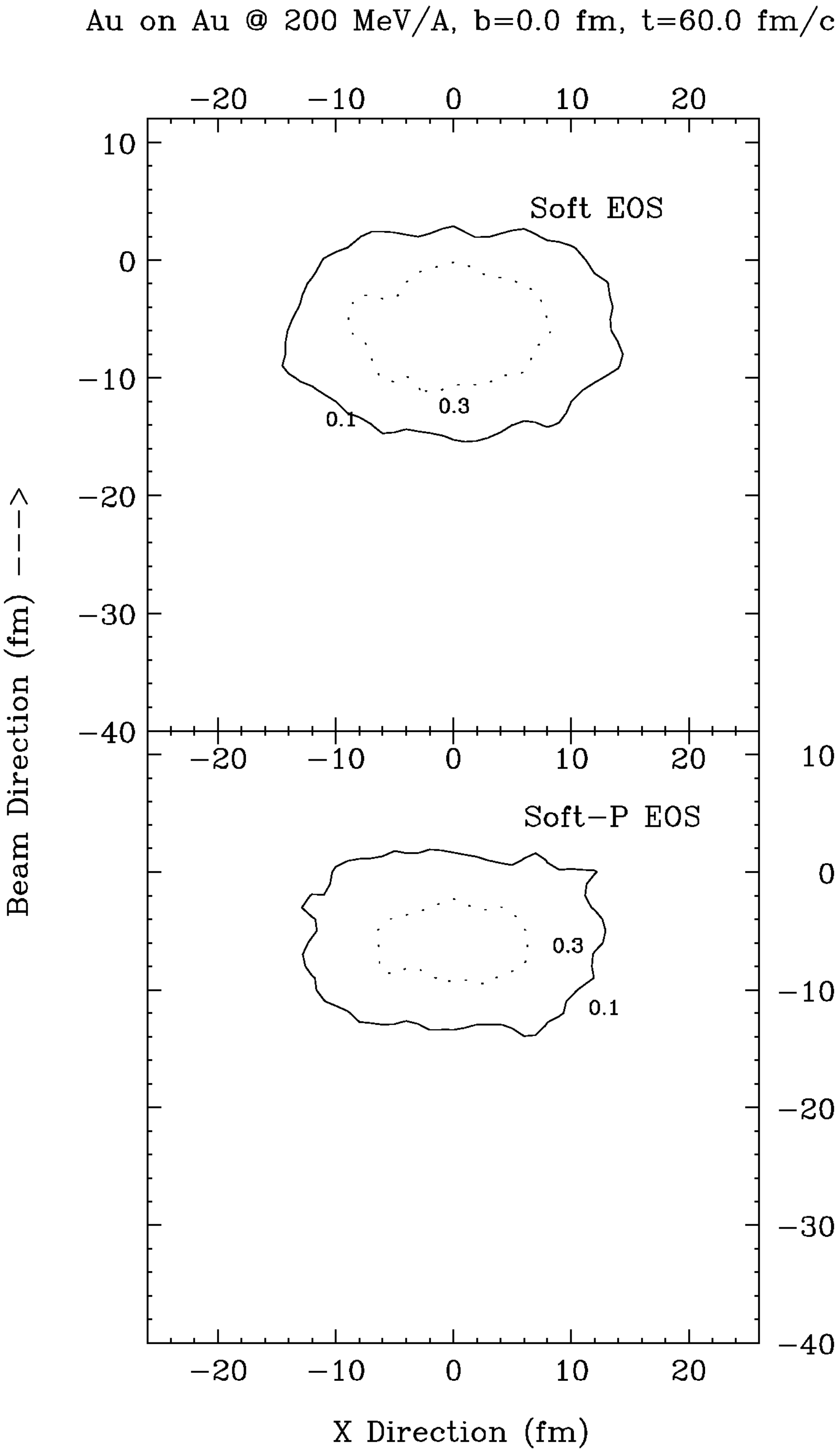

Figure 2.16: Calculated density contours. Numbers are normalized densities: ρ/ρ_0.

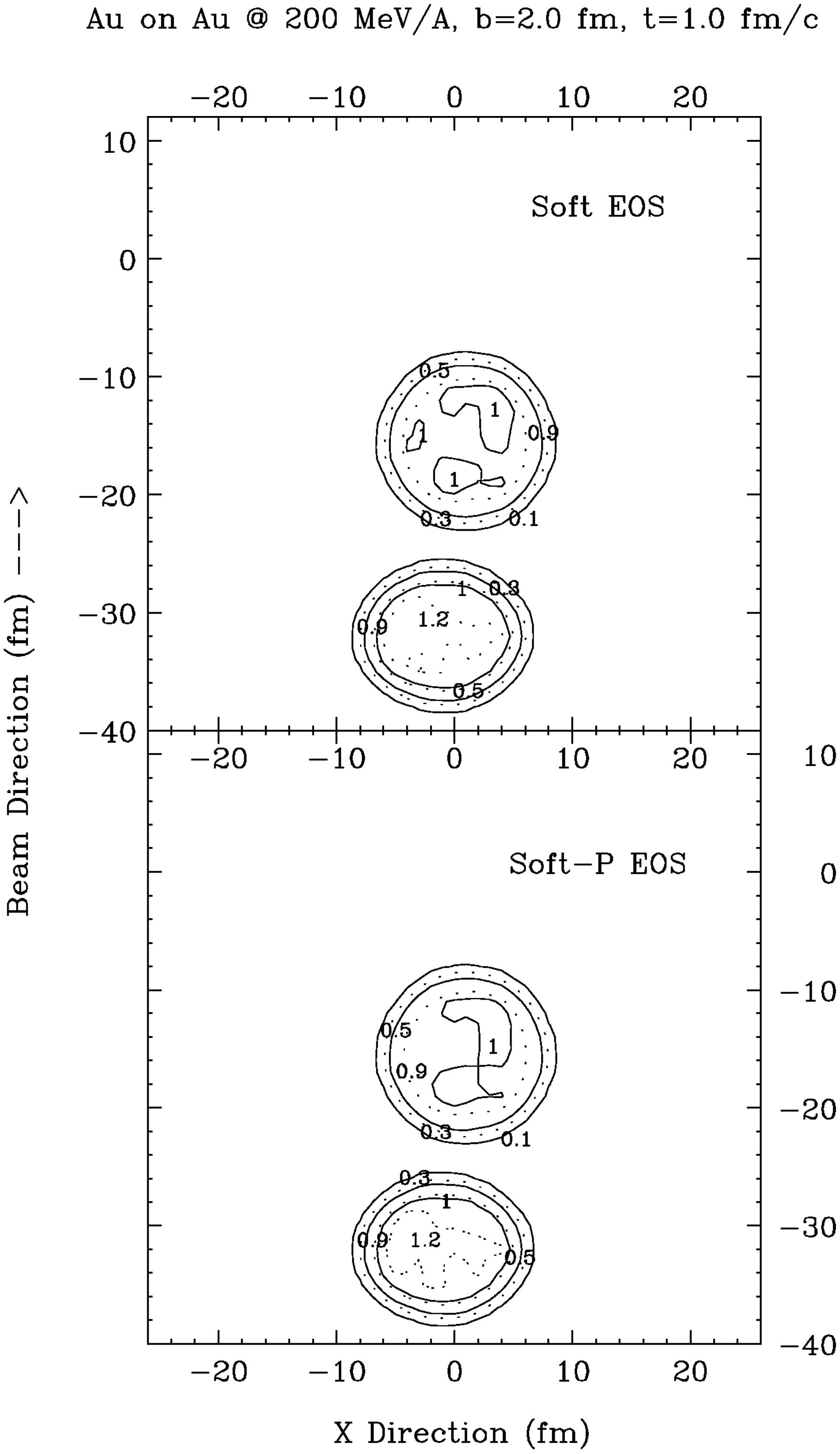

Figure 2.17: Calculated density contours. Numbers are normalized densities: ρ/ρ_0.

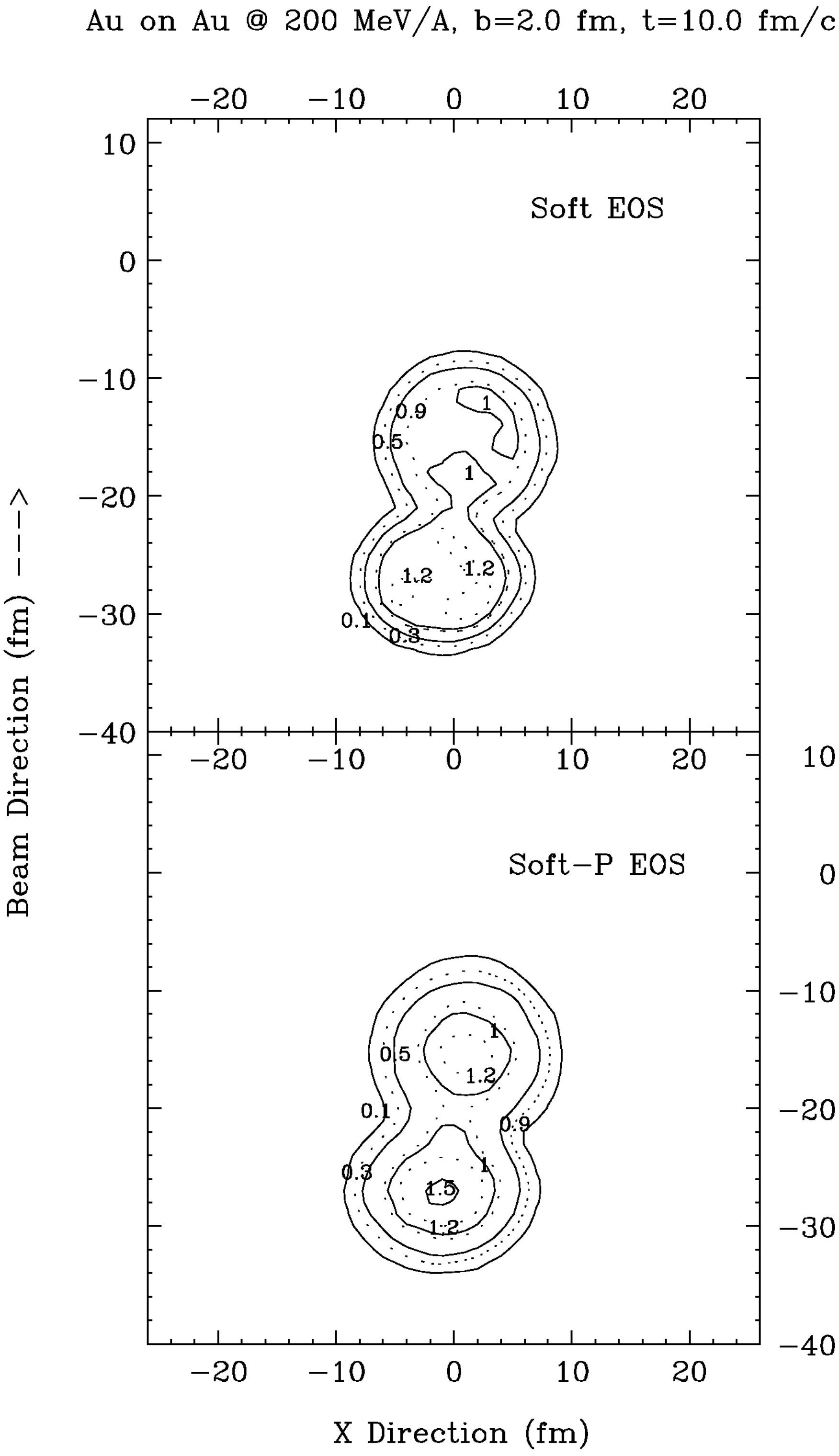

Figure 2.18: Calculated density contours. Numbers are normalized densities: ρ/ρ_0.

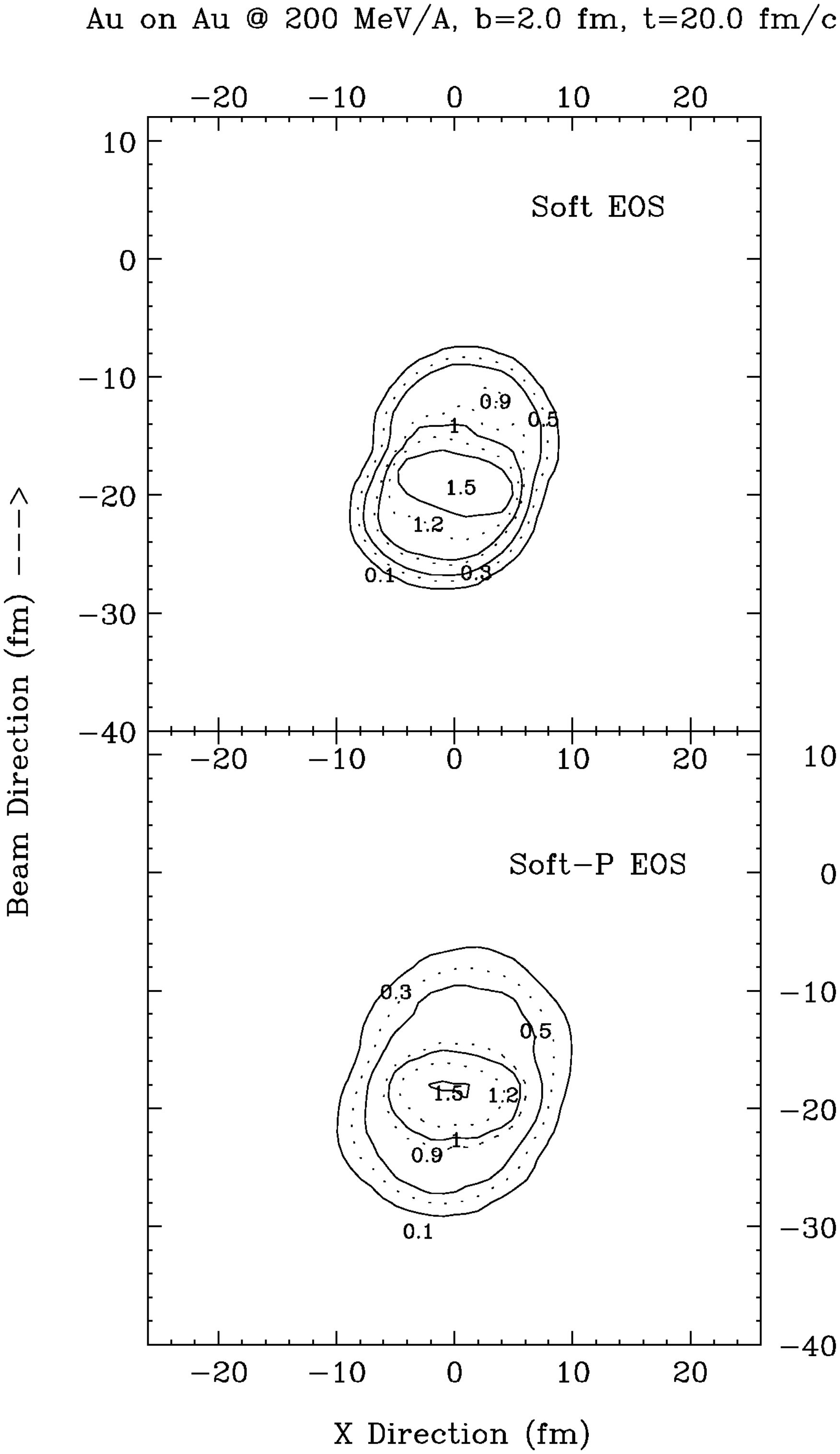

Figure 2.19: Calculated density contours. Numbers are normalized densities: ρ/ρ_0.

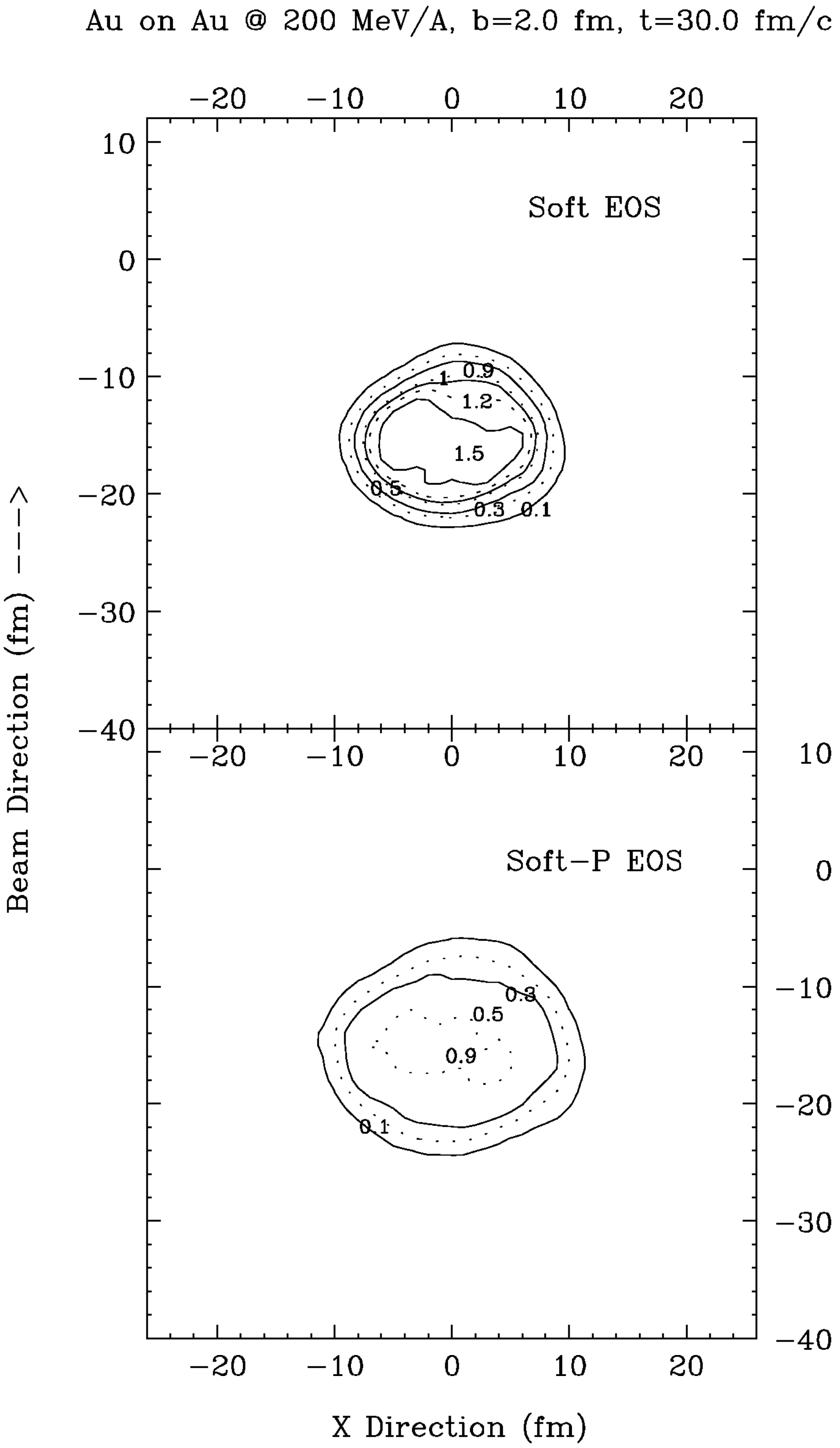

Figure 2.20: Calculated density contours. Numbers are normalized densities: ρ/ρ_0.

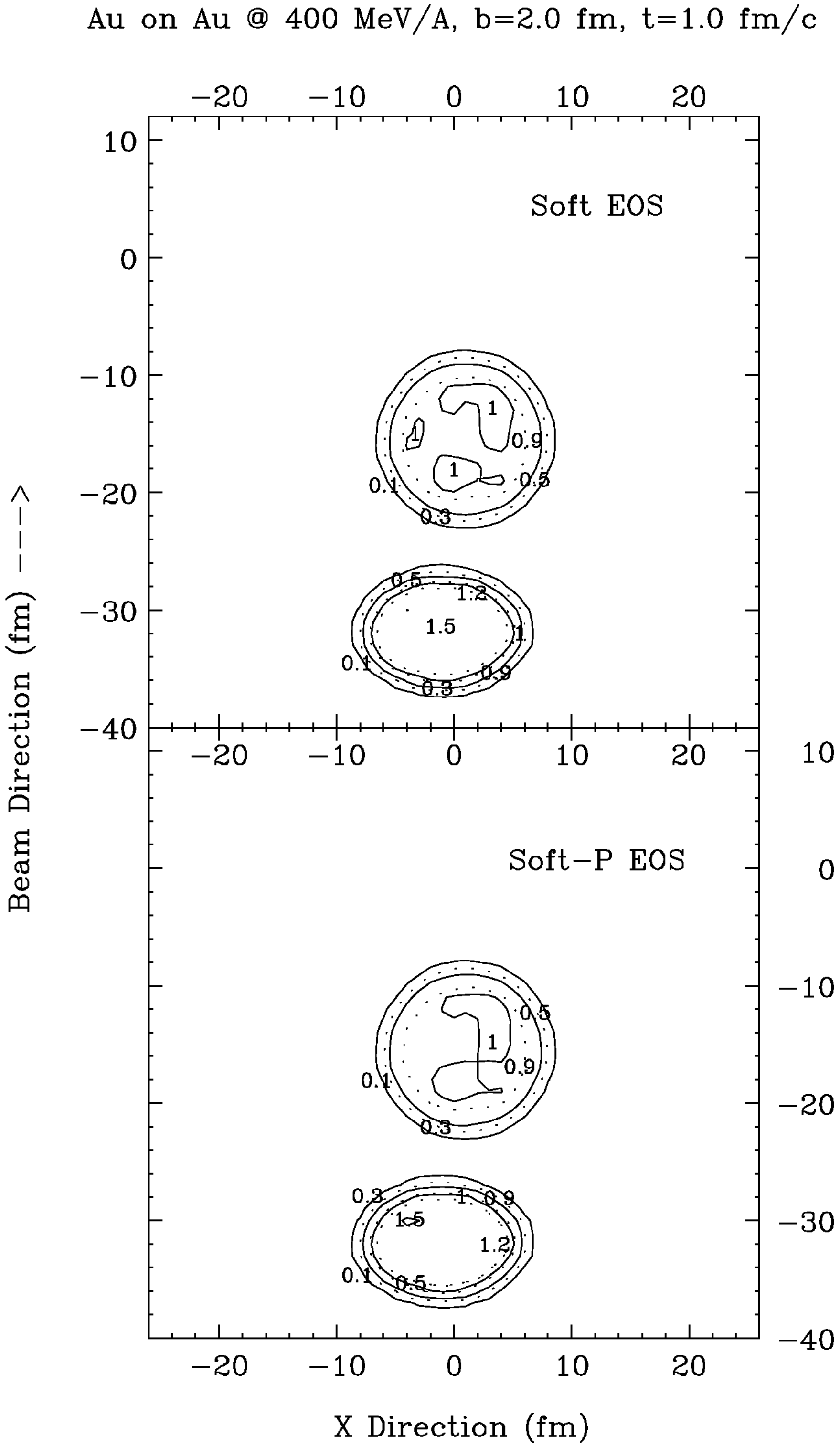

Figure 2.21: Calculated density contours. Numbers are normalized densities: ρ/ρ_0.

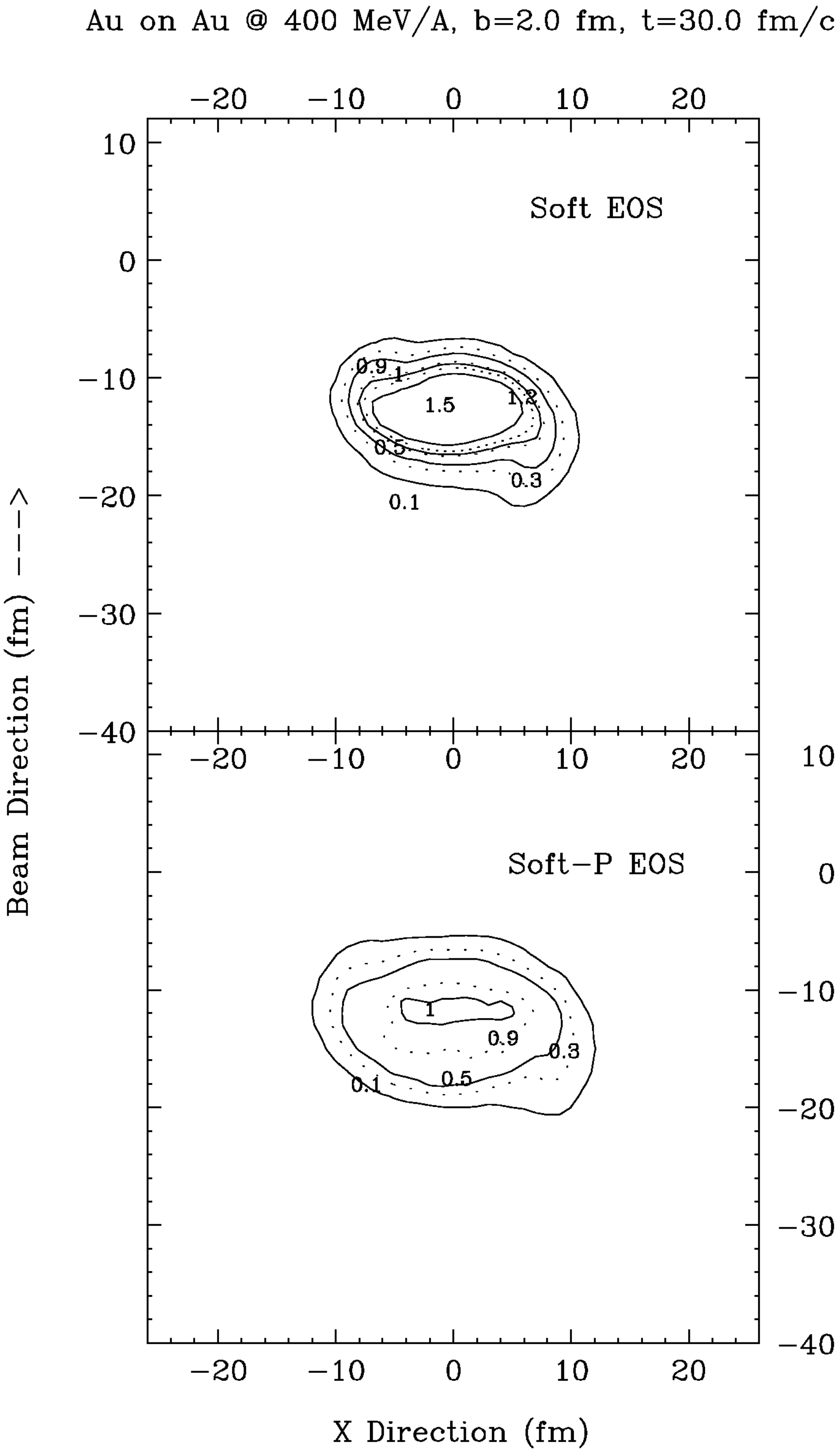

Figure 2.22: Calculated density contours. Numbers are normalized densities: ρ/ρ_0.

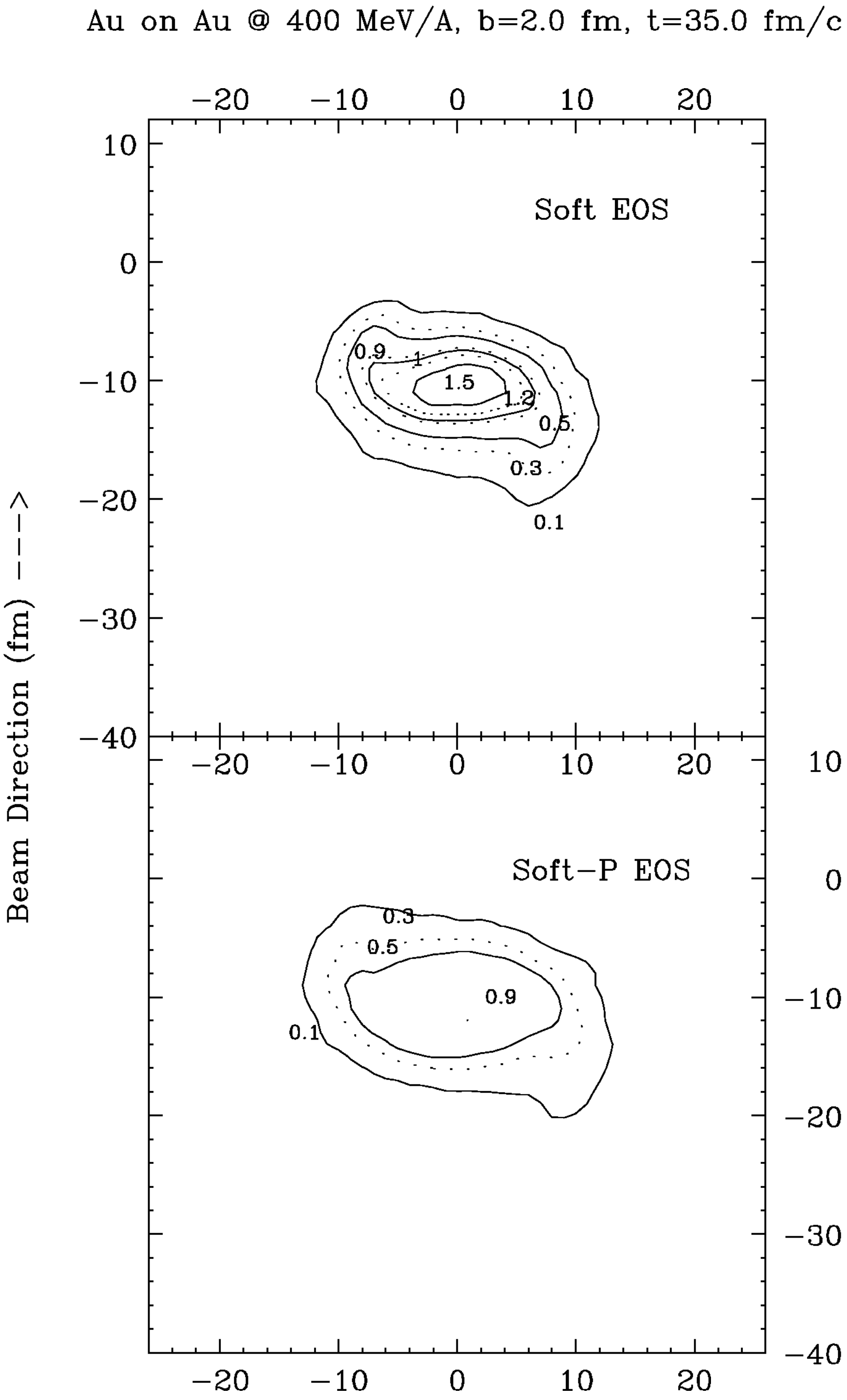

Figure 2.23: Calculated density contours. Numbers are normalized densities: ρ/ρ_0.

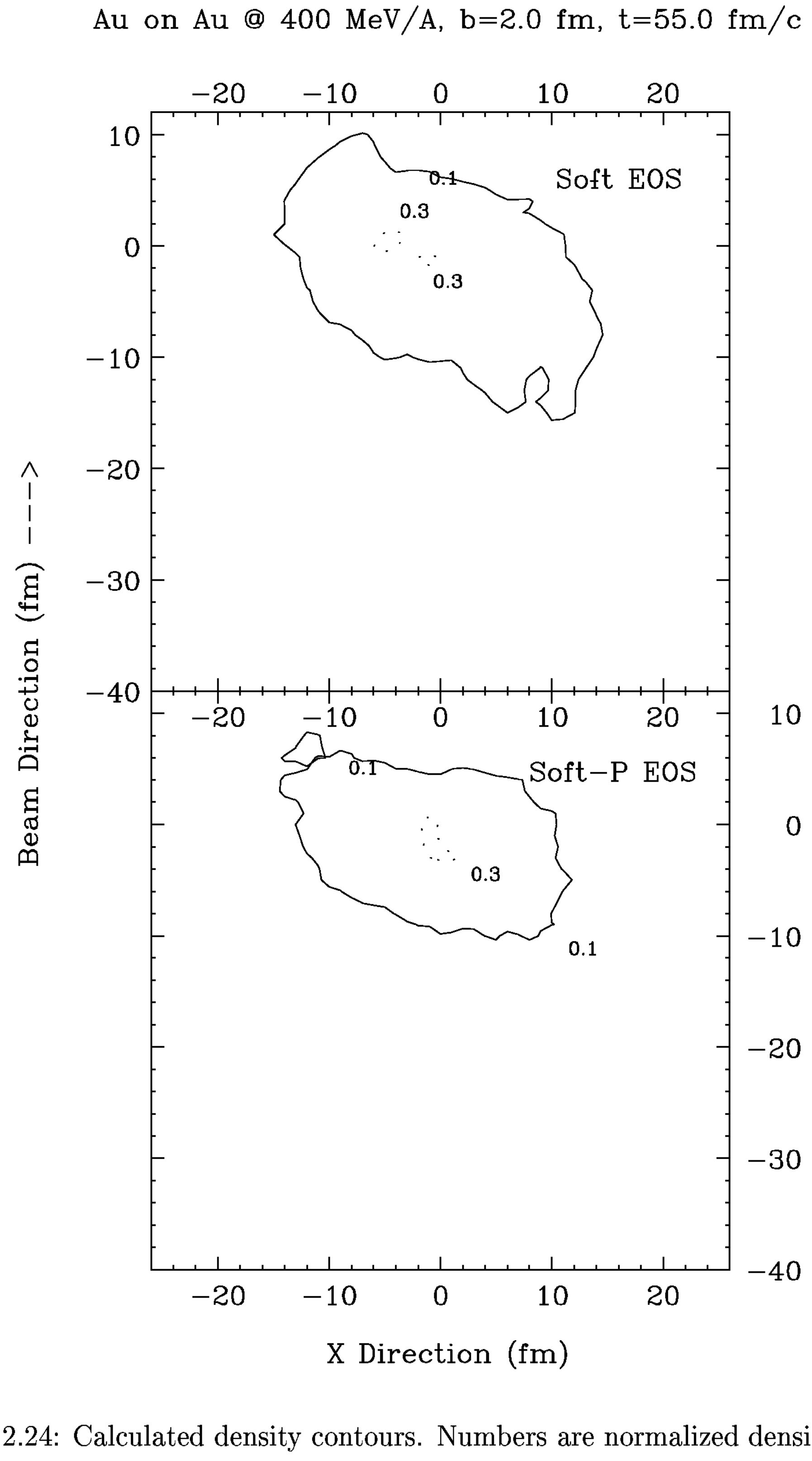

Figure 2.24: Calculated density contours. Numbers are normalized densities: ρ/ρ_0.

2.3.2 Sphericity Analysis

A useful means of characterizing the shape of the final-state momentum-space distribution is sphericity analysis. Here we follow closely the works of Gyulassy, *et al.*,[Gyu82], Gutbrod, *et al.*,[Gut90] and Danielewicz [Dan95].

A weighted flow tensor is calculated from the final-state momenta:

$$F_{ij} = \sum_{\nu=1}^{N} w_\nu p_i(\nu) p_j(\nu) \tag{2.3}$$

where the sum is taken over all N fragments each of which possess an index ν. The weight w_ν is given as $\frac{1}{2m_\nu}$, where m_ν is the mass of the fragment. In the analysis the tensor is diagonalized and the Eigen vectors are extracted. The largest of the three will correspond to the major axis of the momentum ellipsoid. Its length f_3 is the square of the major radius, and its direction defines the flow angle for the event. The remaining two vectors define the size and orientation of the minor axes. Their directions can be used to define the reaction plane in the analysis of experimental data. However, since we possess *a priori* knowledge of the reaction plane in the BUU model, they simply serve to describe the oblateness of the ellipsoid. Total kinetic energy is the trace of the diagonalized tensor:$f_1 + f_2 + f_3$.

Figures 2.25 and 2.26 display the results of the sphericity analysis for ^{197}Au on ^{197}Au collisions at 200 MeV/A and 400 MeV/A, respectively. The abscissa is the flow angle and the ordinate is the ratio, $f_3/f_{1,2}$, called the kinetic flow ratios of the events. The number beside each point is the impact parameter in fm/c.

In Figure 2.25 the trajectories of the two systems, one momentum-dependent and the other momentum-independent, are well separated for the larger impact parameters. It is little surprise that this separation is accompanied by a difference in the flow values (see Figure 2.12). Note that for the lower impact parameters the momentum-dependent calculations yield a final-state momentum distribution of protons that is more spherical than that of the momentum-independent calculations.

The picture is not so simple; one cannot explain the differences in flow values using only sphericity arguments. It is true that the more spherical the momentum distribution, the lower the flow value, but the orientation of the momentum ellipsoid plays a part as well. And while the momentum-dependent calculations show a more spherical momentum distribution, they also have higher flow angles. Thus there are two competing event characteristics: the flow angle, and the sphericity.

Figure 2.26 shows the same calculations, but at 400 MeV/A. Here the trajectories are more alike. The points from the momentum-dependent calculations and the momentum-independent calculations are closer to one another for the lower impact parameters than those in the previous Figure. Returning to Figure 2.12 one can see that the two systems exhibit similar flow values until an impact parameter of 4 fm. Thus the flow enhancement appears energy dependent.

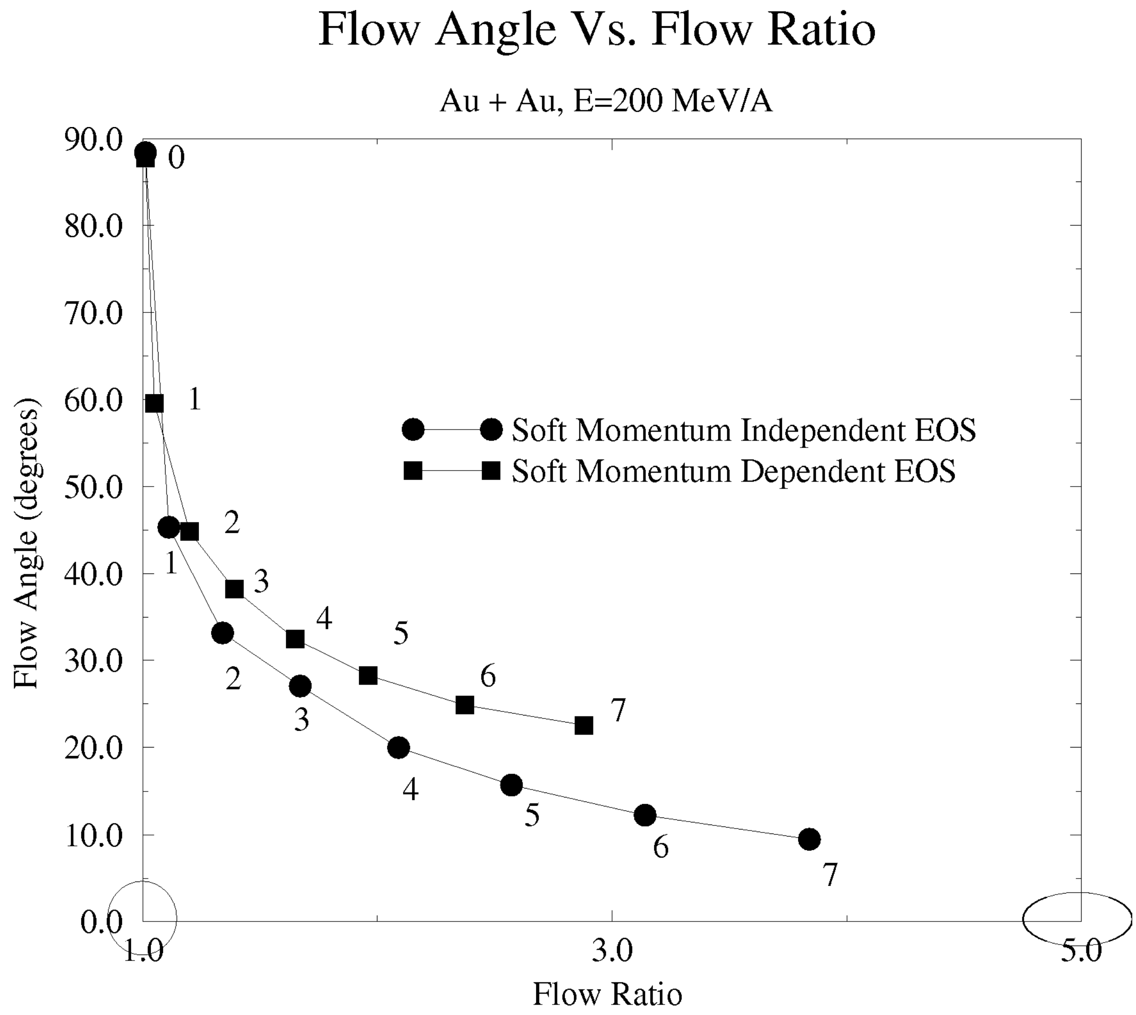

Figure 2.25: Flow angle versus flow ratio $f_3/f_{1,2}$ for protons. Squares are for soft (K=200 MeV) equation of state without momentum dependence. Circles are for soft momentum-dependent equation of state. Numerals beside the points indicate the impact parameter in fm.

2.3.3 Total In-Plane, Transverse Momentum Versus Rapidity

Flow is defined as

$$\left.\frac{d\langle\, p_x\rangle}{dy}\right|_{y=0},$$

where $\langle\, p_x\rangle$ is

$$\frac{\sum_{\nu(y)}^{N(y)} p_x^\nu}{N(y)},$$

$N(y)$ is the number of fragments (protons in this work) with rapidity y, and $\nu(y)$ is the particle index. Rapidity is defined as

$$y = \frac{1}{2}\ln\left(\frac{E^\nu + p_z^\nu}{E^\nu - p_z^\nu}\right), \tag{2.4}$$

where

$$E^\nu = \sqrt{p_x^\nu p_x^\nu + p_y^\nu p_y^\nu + p_z^\nu p_z^\nu + m_\nu^2}.$$

The z-direction is usually taken to correspond to the direction of the beam, the x-direction corresponds to the impact parameter vector, and the speed of light is taken as unity. This often-used parameter offers the convenience of simplifying velocity addition for relativistic systems. Once fragments are assigned their rapidities relative to an inertial frame, their velocities relative to another inertial frame can be calculated by treating their rapidities and the rapidity of the inertial frames as Galilean velocities–a much more intuitive operation. Their correct velocities relative to the new inertial frame are then obtained by inverting their new rapidities.

During discussions with PawełDanielewicz, he suggested that the distribution of the total in-plane, transverse momentum in rapidity may be more sensitive to the

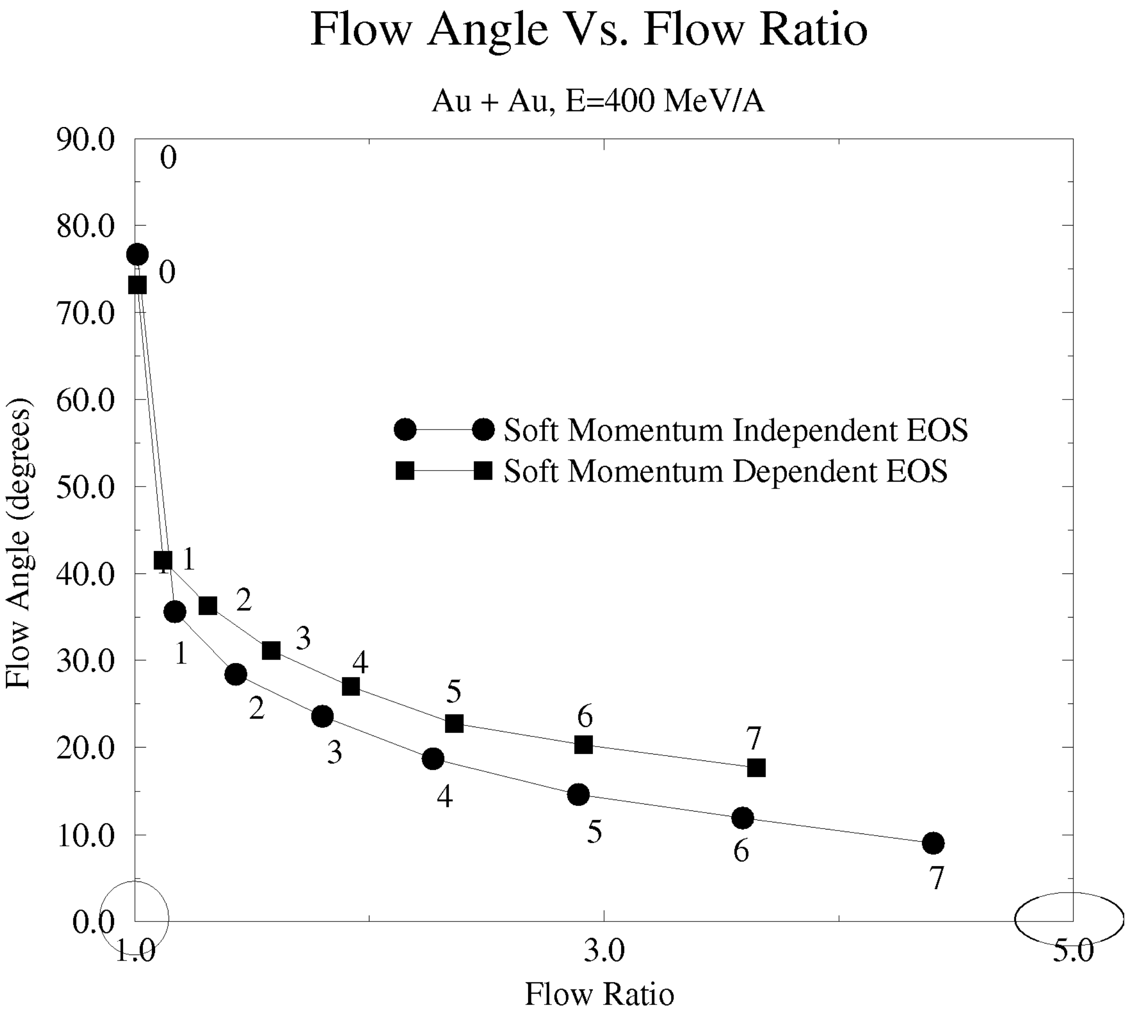

Figure 2.26: Flow angle versus flow ratio $f_3/f_{1,2}$ for protons. Squares are for soft (K=200 MeV) equation of state without momentum dependence. Circles are for soft momentum-dependent equation of state. Numerals beside the points indicate the impact parameter in fm.

flow enhancement seen in momentum-independent calculations. This observable can be written as

$$\mathcal{O}(y) = \sum_{\nu(y)}^{N(y)} p_x^\nu. \tag{2.5}$$

Figures 2.27 and 2.28 show the total transverse in-plane momentum for 200 MeV/A ^{197}Au on ^{197}Au collisions. Two curves are shown in each panel of each Figure: one for the soft momentum-independent mean field, and one for the soft momentum-dependent mean field. Figure 2.27, upper panel, shows $\mathcal{O}(y)$ oscillating around zero for central collisions. At an impact parameter of 2 fm, Figure 2.27, lower panel, the observable differentiates between the momentum-dependent mean field calculations and the momentum-independent mean field calculations. In the lower panel of Figure 2.27 near mid-rapidity, the slope of the momentum-independent curve is larger than the slope of the momentum-dependent curve. The slopes of the two curves are almost identical in appearance for an impact parameter of 4 fm, Figure 2.28, upper panel. However, the lower panel shows the mid-rapidity slope of the momentum-dependent curve exceeding that of the momentum-independent curve. All of this correlates well with the trends in the calculated flow values of Figure 2.12, lower panel.

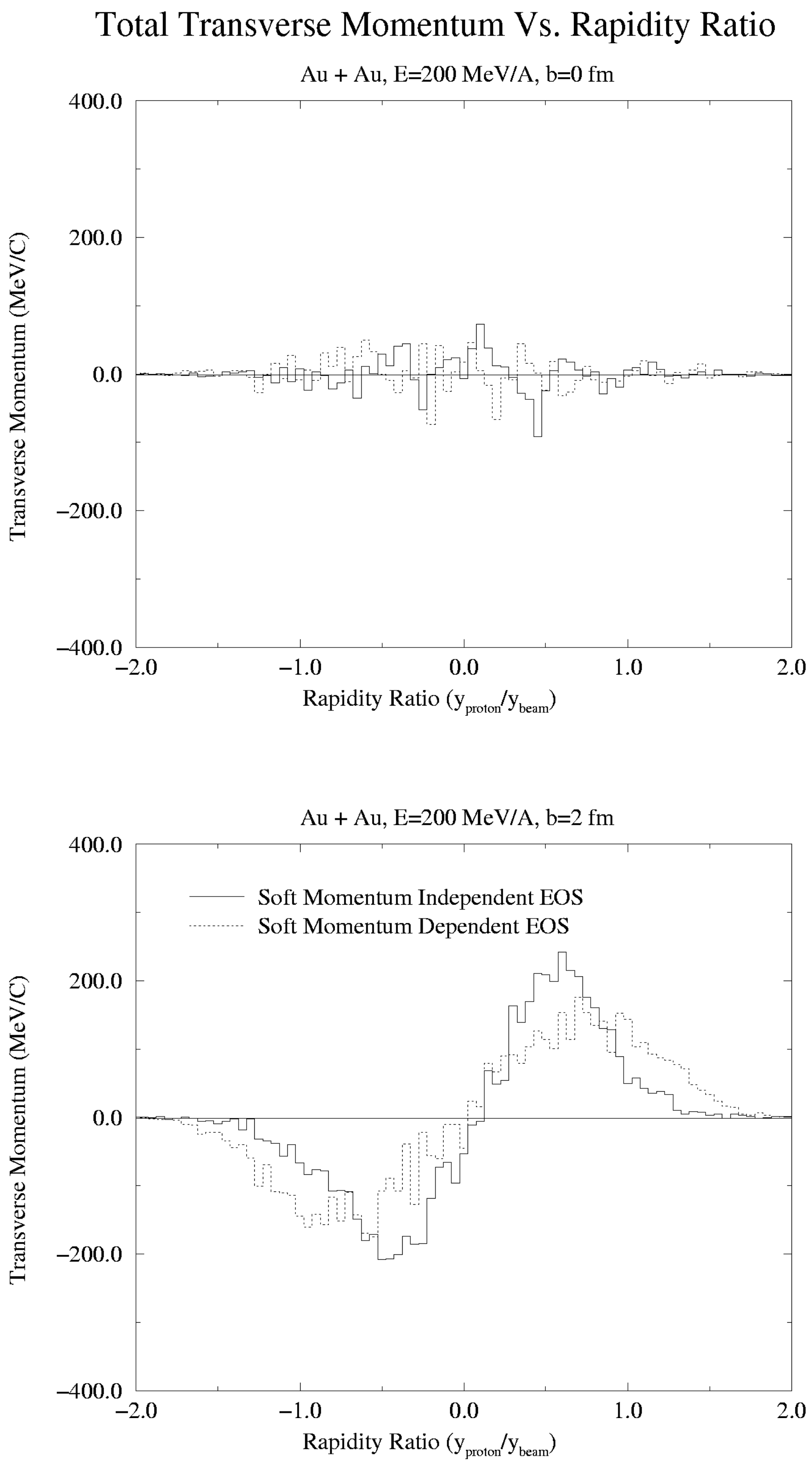

Figure 2.27: Total transverse momentum as a function of rapidity-ratio.

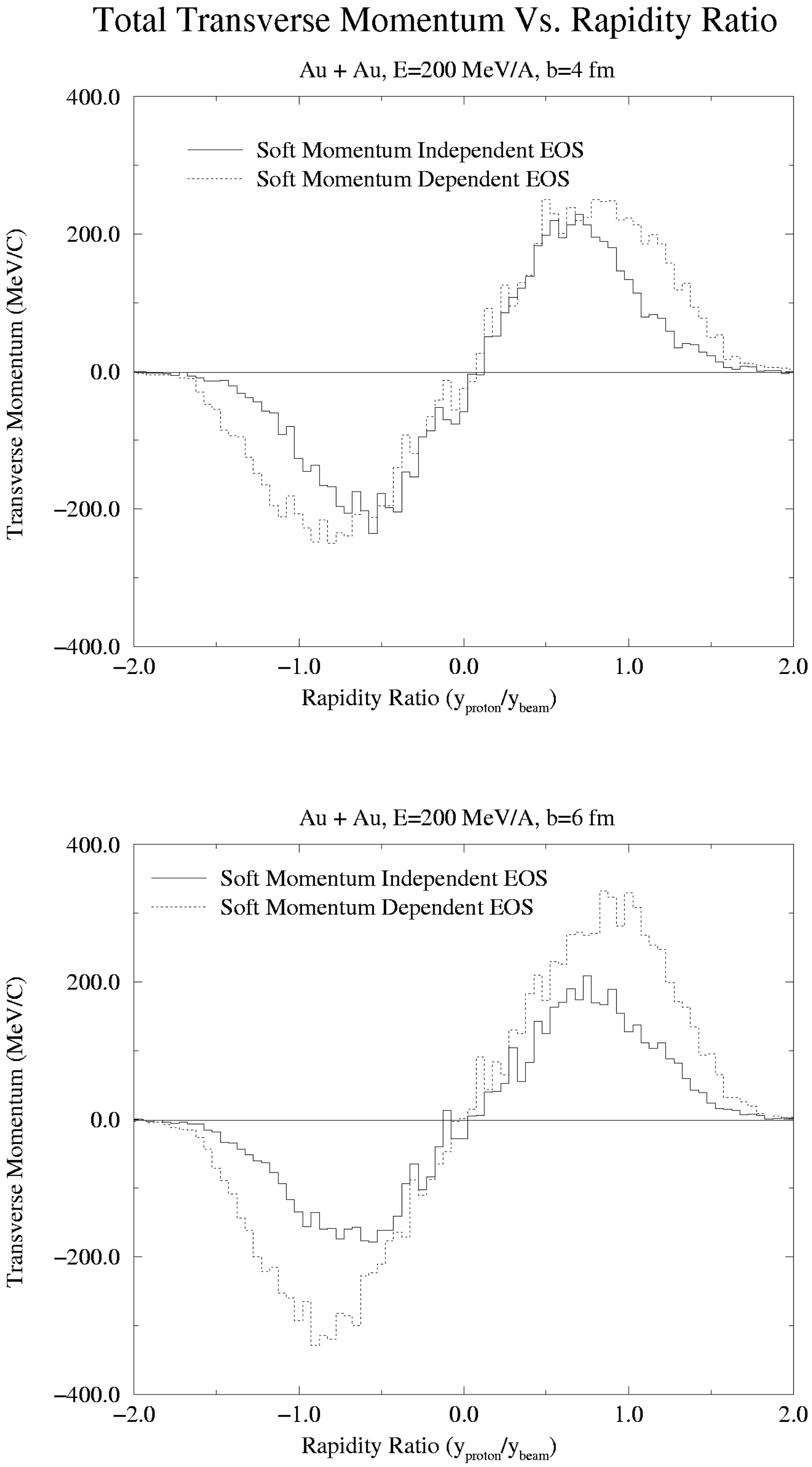

Figure 2.28: Total transverse momentum as a function of rapidity-ratio.

The calculated $\mathcal{O}(y)$ for ^{197}Au on ^{197}Au collisions at 400 MeV/A, Figures 2.29 and 2.30, begin much the same; at zero impact parameter, $\mathcal{O}(y)$ oscillates about zero. However, for an impact parameter of 2 fm, the mid-rapidity slopes of the curves are very similar. For 4 fm and 6 fm, Figure 2.30 the momentum-dependent calculations result in larger mid-rapidity slopes for the total in-plane, transverse momentum than those from the momentum-dependent calculations. Again, this correlates well with the calculated flow values from Figure 2.12, upper panel.

The 200 MeV/A calculations show that the high- and low-rapidity peaks of $\mathcal{O}(y)$ are shifted more toward mid-rapidity for the momentum-independent mean field than for the momentum-dependent mean field. This effect persists throughout the range of impact parameters studied. The effect is not as dramatic in the 400 MeV/A calculations. This could mean there is more overall stopping of nuclear matter in the momentum-independent calculations than the momentum-dependent calculations, a counter-intuitive result. However, the effect appears energy-dependent, as does the enhancement of flow in the momentum-independent calculations over flow in momentum-dependent calculations. The two are probably related, but not in a simple way.

One may write the total in-plane, transverse momentum, $\mathcal{O}(y)$, as:

$$p_x(y) = N(y)\langle p_x\rangle(y),$$

where $N(y)$ is the number distribution in rapidity. The slope of the distribution is then:

$$\frac{p_x(y)}{dy} = \frac{dN(y)}{dy}\langle p_x\rangle(y) + \frac{d\langle p_x\rangle(y)}{dy}N(y). \tag{2.6}$$

Thus, if the distribution is symmetric about mid-rapidity, which within fluctuations it is, the slope of $\mathcal{O}(y)$ is enhanced over the flow signal. However, the slope of this observable is more sensitive to acceptance cuts than is transverse flow.

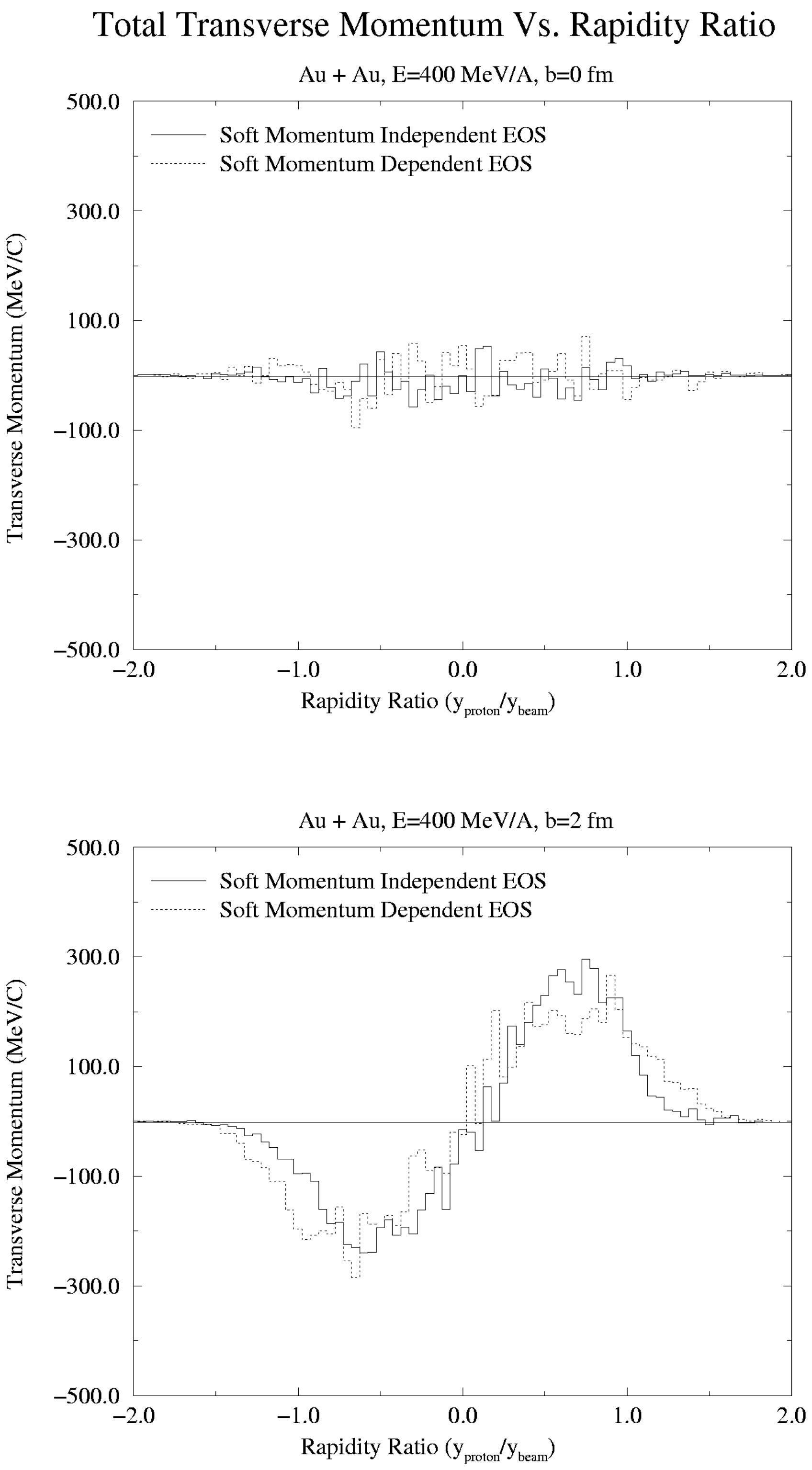

Figure 2.29: Total transverse momentum as a function of rapidity-ratio.

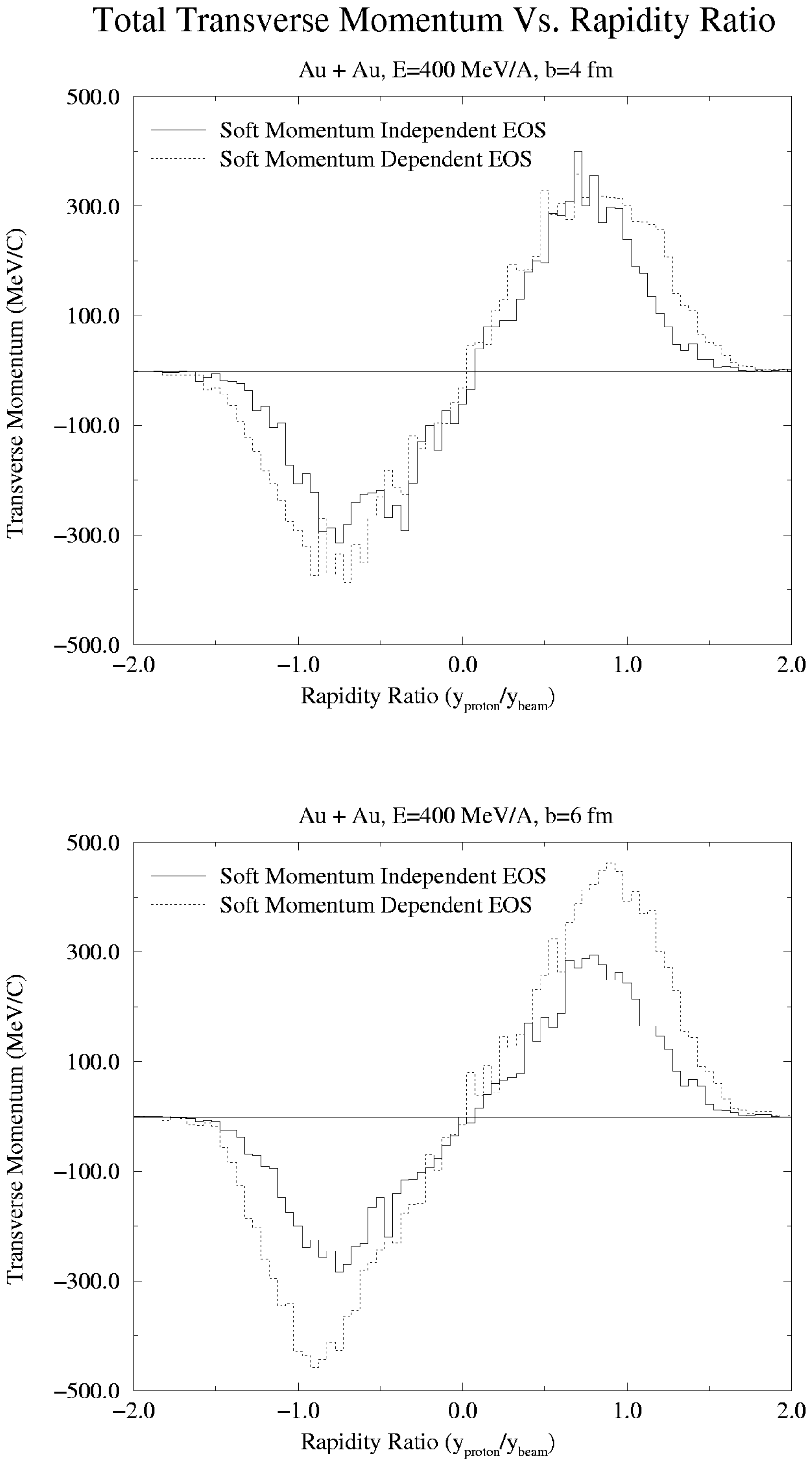

Figure 2.30: Total transverse momentum as a function of rapidity-ratio.

To investigate the behavior of $\mathcal{O}(y)$, one may attempt to find an analytical expression which relates $\mathcal{O}(y)$ to the characteristics of the momentum distribution. Outlined below is such an attempt.

Analytical Exploration of $\mathcal{O}(y)$

Consider an inversion of Equation 2.4:

$$\frac{p_z^2(1-\eta^2)}{m^2\eta^2} - \frac{p_x^2}{m^2} - \frac{p_y^2}{m^2} = 1, \tag{2.7}$$

where $\eta = \tanh(y)$. In momentum-space constant rapidity yields hyperboloids of two sheets. $\mathcal{O}(y)$ is then the sum of all values p_x on surfaces of constant rapidity:

$$\mathcal{O}(y) = \int\limits_{\mathcal{S}\,\in\, y=const.} p_x\, g(\vec{p},t)\, d\mathcal{S}, \tag{2.8}$$

where the weight is

$$g(\vec{p},t) = \int\limits_{\infty} f(\vec{p},\vec{r},t)\, d\vec{r},$$

and $f(\vec{p},\vec{r},t)$ is the Wigner phase-space density distribution evolved under the BUU formalism.

Figure 2.3 is typical for heavy-ion BUU collisions: the final state momentum distributions are ellipsoidal in shape, though tilted about the p_y axis at an angle equal to the flow angle from the sphericity analysis. An ellipsoid rotated ϕ_{flow} about the p_y-axis has the form:

$$\begin{aligned} &p_x^2\left(\frac{\cos(\phi_{flow})^2}{A^2} + \frac{\sin(\phi_{flow})^2}{B^2}\right) + \\ &p_z^2\left(\frac{\sin(\phi_{flow})^2}{A^2} + \frac{\cos(\phi_{flow})^2}{B^2}\right) + \\ \frac{p_y^2}{B^2} + 2p_xp_z &\left(\frac{\cos(\phi_{flow})\sin(\phi_{flow})}{B^2} - \frac{\cos(\phi_{flow})\sin(\phi_{flow})}{A^2}\right) = 1, \end{aligned} \tag{2.9}$$

where C is the major axis, and A,B are the minor axes in the rotated system. Then the total in-plane, transverse momentum for a distribution uniform over a rotated ellipse can be written as:

$$\mathcal{O}(y) = \iint\limits_{\vec{p} \in \{\mathfrak{E} \cap \mathfrak{H}\}} p_x \, \varkappa \, d\vec{r} \, d\vec{p} \tag{2.10}$$

where

$$\begin{gathered}
\mathfrak{E} \equiv \{p_x, p_y, p_z : \\
p_x^2 \left(\frac{\cos(\phi_{flow})^2}{A^2} + \frac{\sin(\phi_{flow})^2}{B^2} \right) + \\
p_z^2 \left(\frac{\sin(\phi_{flow})^2}{A^2} + \frac{\cos(\phi_{flow})^2}{B^2} \right) + \\
\frac{p_y^2}{B^2} + 2p_x p_z \left(\frac{\cos(\phi_{flow}) \sin(\phi_{flow})}{B^2} - \frac{\cos(\phi_{flow}) \sin(\phi_{flow})}{A^2} \right) \leqq 1\},
\end{gathered} \tag{2.11}$$

$$\mathfrak{H} \equiv \{p_x, p_y, p_z : \frac{p_z^2(1-\eta^2)}{m^2\eta^2} - \frac{p_x^2}{m^2} - \frac{p_y^2}{m^2} = 1\}, \tag{2.12}$$

and where $\varkappa$ is a constant.

The surface integral of Equation 2.10 is confounded by the requirement that it must be carried out over the intersection of the rotated momentum ellipsoid and the surfaces of the hyperboloids of constant rapidity in momentum-space. These intersections, surfaces really, take the form:

$$\begin{gathered}
p_z^2 \left[\frac{(1-\eta^2)}{\eta^2} \left(\frac{\cos(\phi_{flow})^2}{A^2} + \frac{\sin(\phi_{flow})^2}{B^2} \right) + \frac{\sin(\phi_{flow})^2}{A^2} + \frac{\cos(\phi_{flow})^2}{B^2} \right] + \\
\frac{p_y^2}{B^2} \pm 2p_z \sqrt{\frac{p_z^2(1-\eta^2)}{\eta^2} - p_y^2 - m^2} = 1
\end{gathered} \tag{2.13}$$

which does not have a closed-form solution.

A uniform density within the ellipse is admittedly artificial. A more natural approach would be to use a Gaussian-ellipsoidal distribution:

$$g(\vec{p}) = \kappa \exp\left(\frac{-p_x^2}{2\sigma_x^2}\right) \exp\left(\frac{-p_y^2}{2\sigma_y^2}\right) \exp\left(\frac{-p_z^2}{2\sigma_z^2}\right). \qquad (2.14)$$

Surfaces of constant probability density are ellipsoidal.

With this density $\mathcal{O}(y)$ may be written:

$$\mathcal{O}(y) = \int_{\mathcal{S}\in\mathfrak{H}} p_x\, g(\vec{p})\, d\mathcal{S}. \qquad (2.15)$$

Here the integral may be transformed into:

$$\mathcal{O}(y) = \int_{A\in p_x - p_y plane} p_x\, g(p_x, p_y, h(p_x, p_y)) \sec(\gamma)\, dA, \qquad (2.16)$$

where

$$h(p_x, p_y) = \pm\sqrt{\frac{(m^2 + p_x^2 + p_y^2)\eta^2}{1-\eta^2}},$$

and γ is the angle between the outwardly directed unit normal to the surface of one hyperboloid–constant rapidity–and the z-direction. A solution to this integral is not attempted here.

Numerical Analysis of $\mathcal{O}(y)$

In an effort to understand better the behavior of the total in-plane transverse momentum in rapidity in the absence of a closed-form relationship between the observable and hypothetical momentum-space distributions, a numerical study is presented.

Computer programs were written to generate momentum-space ellipsoidal distributions for calculation of $\mathcal{O}(y)$. Several different distributions were generated, but they all fall under two distinct classes: Constant-density ellipsoid, and Gaussian ellipsoid. Each class was studied separately, and within each class both the total kinetic energy and particle number were conserved. The goal was to explore the characteristics of the total transverse in-plane momentum distribution in rapidity as the momentum ellipsoids changed orientation and oblateness.

The total kinetic energy for each class could best be achieved numerically by first calculating the criteria for conservation using continuous distributions. This can be done analytically:

$$\mathcal{KE} = \frac{1}{2m} \iiint (p_x^2 + p_y^2 + p_z^2)\, g(p_x, p_y, p_z)\, dp_x\, dp_y\, dp_z, \tag{2.17}$$

where $g(p_x, p_y, p_z)$ is the number density of the protons in momentum-space, and m is the proton mass. For a uniform distribution of protons throughout an ellipsoid the integral becomes:

$$\mathcal{KE} = \iiint\limits_{\frac{p_x^2}{A^2}+\frac{p_y^2}{B^2}+\frac{p_z^2}{C^2}\leq 1} (p_x^2 + p_y^2 + p_z^2)\, \varkappa\, dp_x\, dp_y\, dp_z, \tag{2.18}$$

where

$$\varkappa = \frac{3N}{4ABC\pi},$$

N is the number of protons in the ellipsoid, C is the major axis of the ellipsoid and A, B are the minor axes of the ellipsoid. Note that $\mathcal{KE}$ is rotationally invariant.

Using the transform:

$$\begin{aligned} \tilde{p_x} &= \frac{p_x}{A} \\ \tilde{p_y} &= \frac{p_y}{B} \\ \tilde{p_z} &= \frac{p_z}{C} \end{aligned}$$

one can rewrite Equation 2.18 as a spherical integral:

$$\mathcal{KE} = \frac{1}{2m} \iiint\limits_{\tilde{p_x}^2+\tilde{p_y}^2+\tilde{p_z}^2 \leqq 1} ABC(A^2\tilde{p_x}^2 + B^2\tilde{p_y}^2 + C^2\tilde{p_z}^2)\, \varkappa \, d\tilde{p_x}\, d\tilde{p_y}\, d\tilde{p_z} \tag{2.19}$$

$$= \frac{1}{2m}\left(\frac{4\pi}{15}\right) ABC(A^2 + B^2 + C^2)\varkappa$$

$$= \frac{N(A^2 + B^2 + C^2)}{10m}.$$

The calculation of the kinetic energy due to the elliptical Gaussian distribution is simpler:

$$\mathcal{KE} = \frac{1}{2m} \iiint\limits_{\infty} (p_x^2 + p_y^2 + p_z^2)\, (e^{-\frac{p_x^2}{2\sigma_x^2}} e^{-\frac{p_y^2}{2\sigma_y^2}} e^{-\frac{p_z^2}{2\sigma_z^2}})\varpi \, dp_x\, dp_y\, dp_z \tag{2.20}$$

$$= \frac{1}{2m}\left(\frac{\varpi\pi^{\frac{3}{2}}}{8}\right)(\sqrt{\sigma_x^3\sigma_y\sigma_z} + \sqrt{\sigma_x\sigma_y^3\sigma_z} + \sqrt{\sigma_x\sigma_y\sigma_z^3})$$

$$= \frac{1}{2m}\left(\frac{4N}{\sqrt{\pi^3\sigma_x\sigma_y\sigma_z}}\right)\left(\frac{\pi^{\frac{3}{2}}}{8}\right)(\sqrt{\sigma_x^3\sigma_y\sigma_z} + \sqrt{\sigma_x\sigma_y^3\sigma_z} + \sqrt{\sigma_x\sigma_y\sigma_z^3})$$

$$= \frac{1}{2m}N(\sigma_x^2 + \sigma_y^2 + \sigma_z^2).$$

Figures 2.31–2.35 show the total in-plane transverse momentum as a function of rapidity. Within each panel, both kinetic energy and particle number are conserved to within about 2%. Note the high- and low-rapidity tails of $\mathcal{O}(y)$, upper panels, compared to the more abrupt patterns from the constant density ellipsoids, lower panels. This is to be expected since the Gaussian has essentially infinite extent in momentum-space whereas the constant density ellipsoid makes no contributions outside of its finite volume. Notice also that in all cases the peaks in the distributions are sharper for the Gaussian ellipsoids.

Figure 2.31 shows the variation of $\mathcal{O}(y)$ with flow angle for a constant kinetic energy ratio:

$$\frac{f_3}{f_{1,2}} = \frac{\sum_{\nu=1}^{N} p_z^\nu p_z^\nu}{\sum_{\nu=1}^{N} p_x^\nu p_x^\nu = \sum_{\nu=1}^{N} p_y^\nu p_y^\nu},$$

since by symmetry and the absence of fragments $\sum_{\nu=1}^{N} p_x^\nu p_x^\nu = \sum_{\nu=1}^{N} p_y^\nu p_y^\nu$. In both panels a pronounced shift toward mid-rapidity develops as the ellipsoids are rotated. Simple geometrical arguments satisfy for an explanation of this behavior: Consider the problem in two-dimensions where the constant rapidity are hyperbolas in the p_x-p_z plane. As the momentum ellipse is rotated from zero flow angle, positive p_x contributions to the $\sum p_x$ in the forward-going hemisphere overtake the negative p_z contributions. Note that this is not simply a projection of the ellipse onto the p_z-axis as the summation is taken over lines of constant rapidity (the hyperbolas).

Figures 2.32–2.35 show the changes in $\mathcal{O}(y)$ as the shape of the momentum ellipsoids is changed for a given flow angle. In the Gaussian ellipsoids in Figure 2.32 (upper panel) where ϕ_{flow} =20°, the mid-rapidity slope of the curves remain surprisingly constant as the kinetic energy ratio $f_3/f_{1,2}$ goes from 2 to 5. Note that the constant-density ellipsoid (lower panel) shows a slight change is the slope near mid-rapidity. This suggests that

$$\left.\frac{d\mathcal{O}(y)}{dy}\right|_{y=0} \tag{2.21}$$

is relatively insensitive to the oblateness of the ellipsoid for small flow angles. The same can be said, though the effect is less dramatic, for the Gaussian distribution for a flow angle of 40°, Figure 2.33. In both Figures the peaks in the distribution shift only slightly. The value of Equation 2.21 seems more sensitive to the oblateness of the constant-density ellipsoid. However, the constant-density ellipsoidal distribution is un-physical. The Gaussian distribution is more realistic, and one should give more weight to results derived from it.

For larger flow angles, Figures 2.34 and 2.35 show Equation 2.21 nicely distinguishes among the various ellipsoids for both classes of distributions. The peaks, however, appear over nearly the same rapidity.

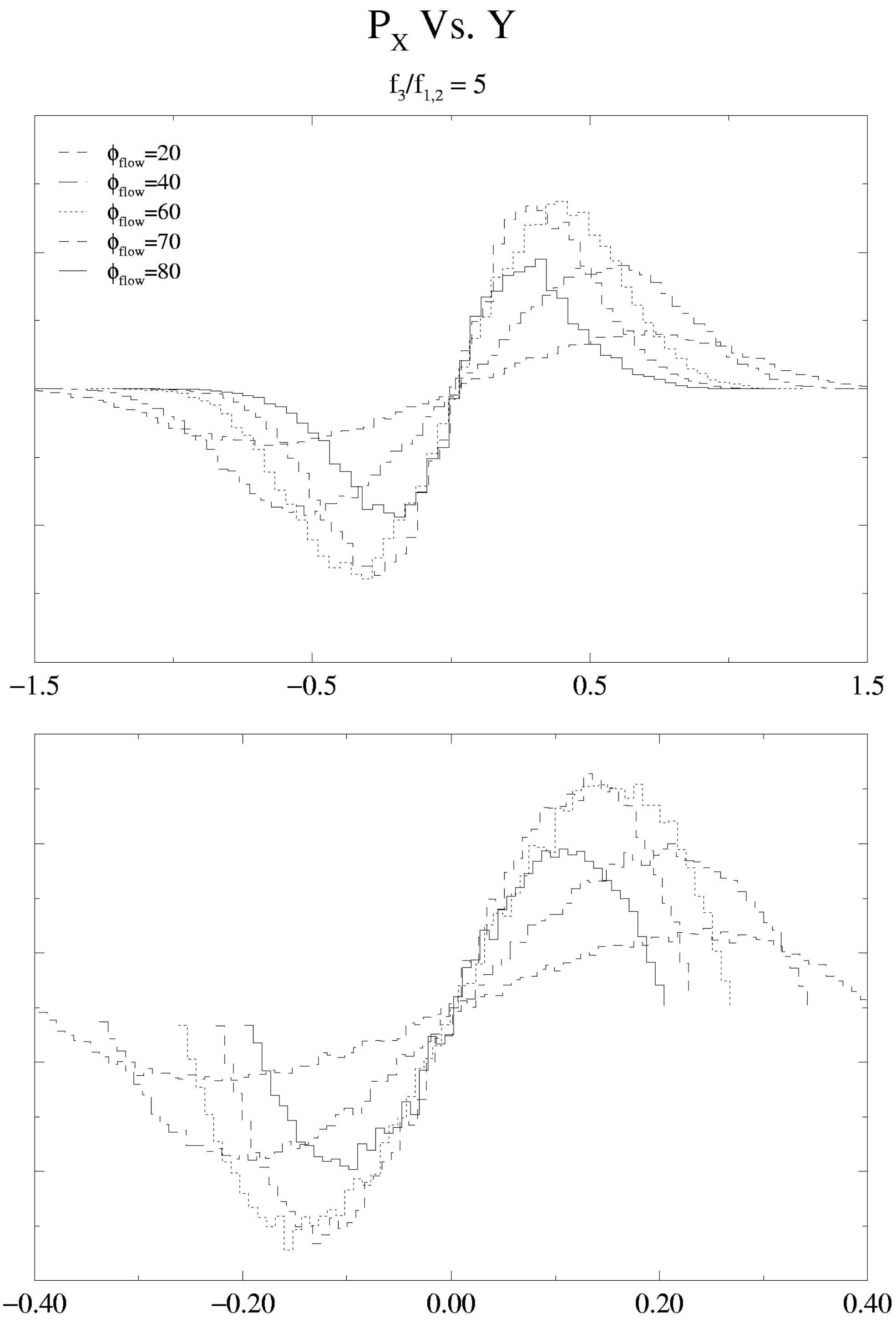

Figure 2.31: Total in-plane, transverse momentum p_x in arbitrary units as a function of rapidity from hypothetical ellipsoids. The upper panel shows results from a Gaussian-ellipsoidal density, whereas the lower panel are results from the uniform ellipsoidal density. Each panel shows $\mathcal{O}(y)$ of ellipsoids which have kinetic energy ratios of 5, but rotated various angles ϕ_{flow} relative to the beam axis.

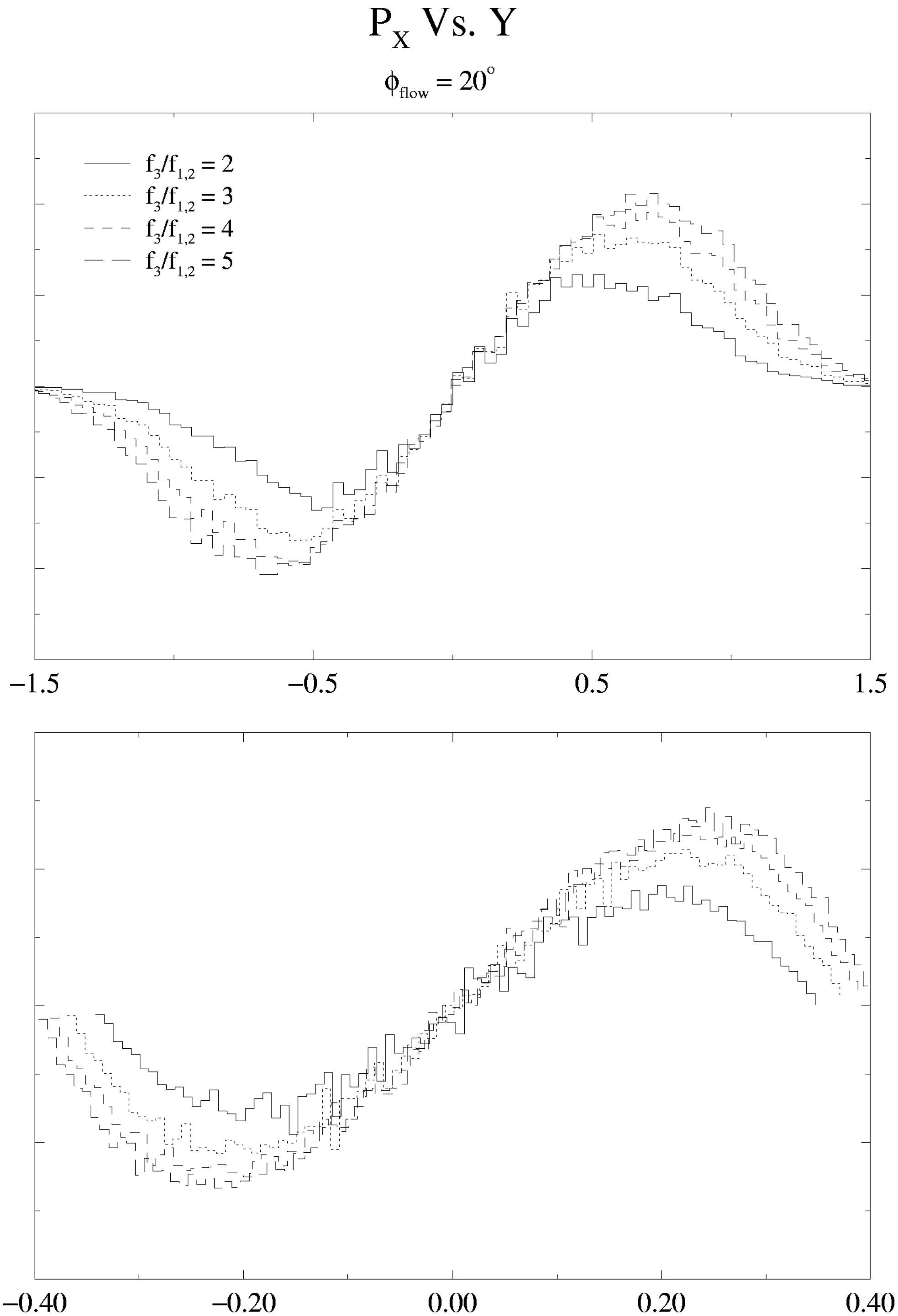

Figure 2.32: Total in-plane, transverse momentum p_x in arbitrary units as a function of rapidity from hypothetical ellipsoids. The upper panel shows results from a Gaussian-ellipsoidal density, whereas the lower panel are results from the uniform ellipsoidal density. Each panel shows $\mathcal{O}(y)$ of ellipsoids rotated various angles ϕ_{flow} relative to the beam axis, but which possess identical kinetic energy ratios.

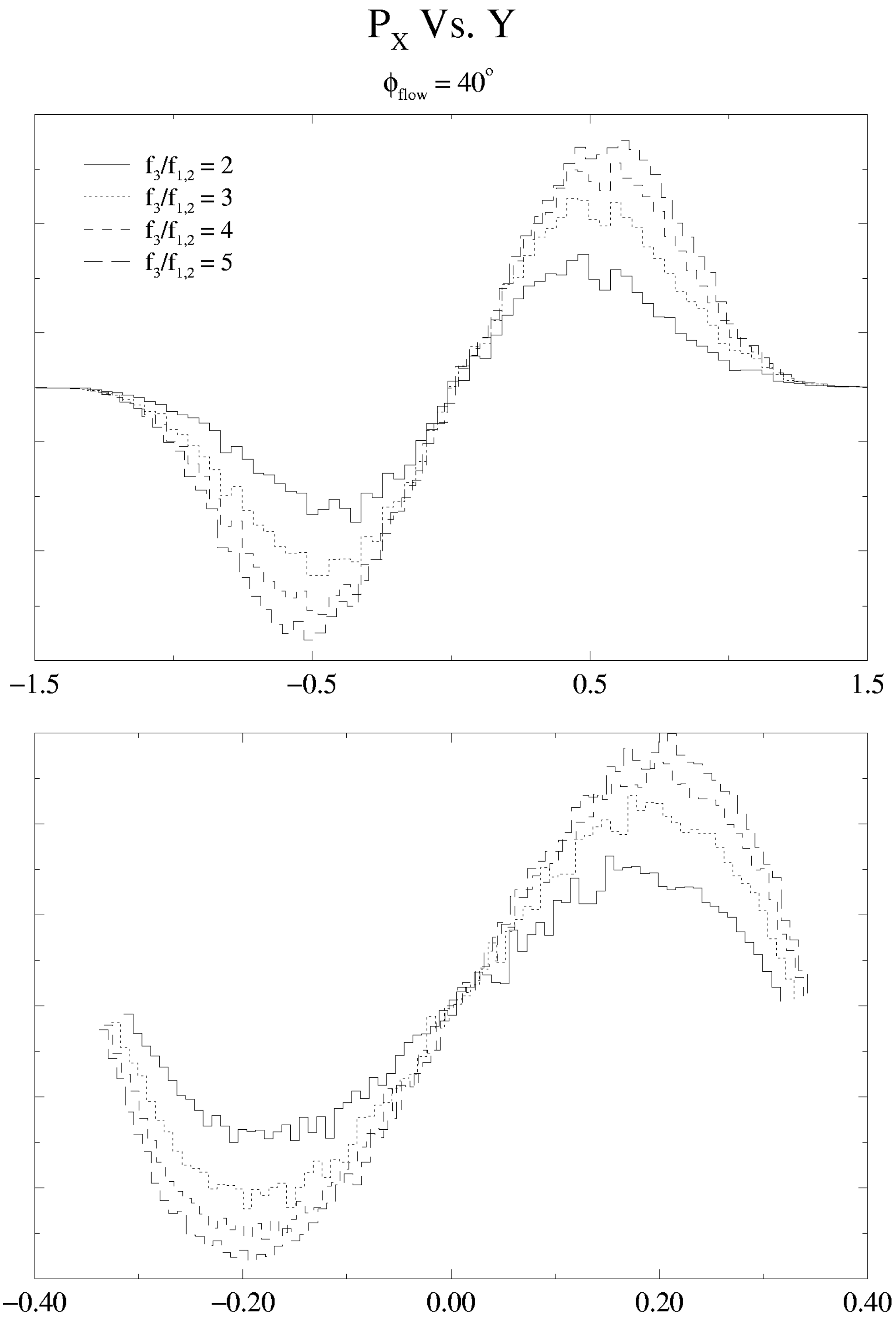

Figure 2.33: Total in-plane, transverse momentum p_x in arbitrary units as a function of rapidity from hypothetical ellipsoids. The upper panel shows results from a Gaussian-ellipsoidal density, whereas the lower panel are results from the uniform ellipsoidal density. Each panel shows $\mathcal{O}(y)$ of ellipsoids rotated various angles ϕ_{flow} relative to the beam axis, but which possess identical kinetic energy ratios.

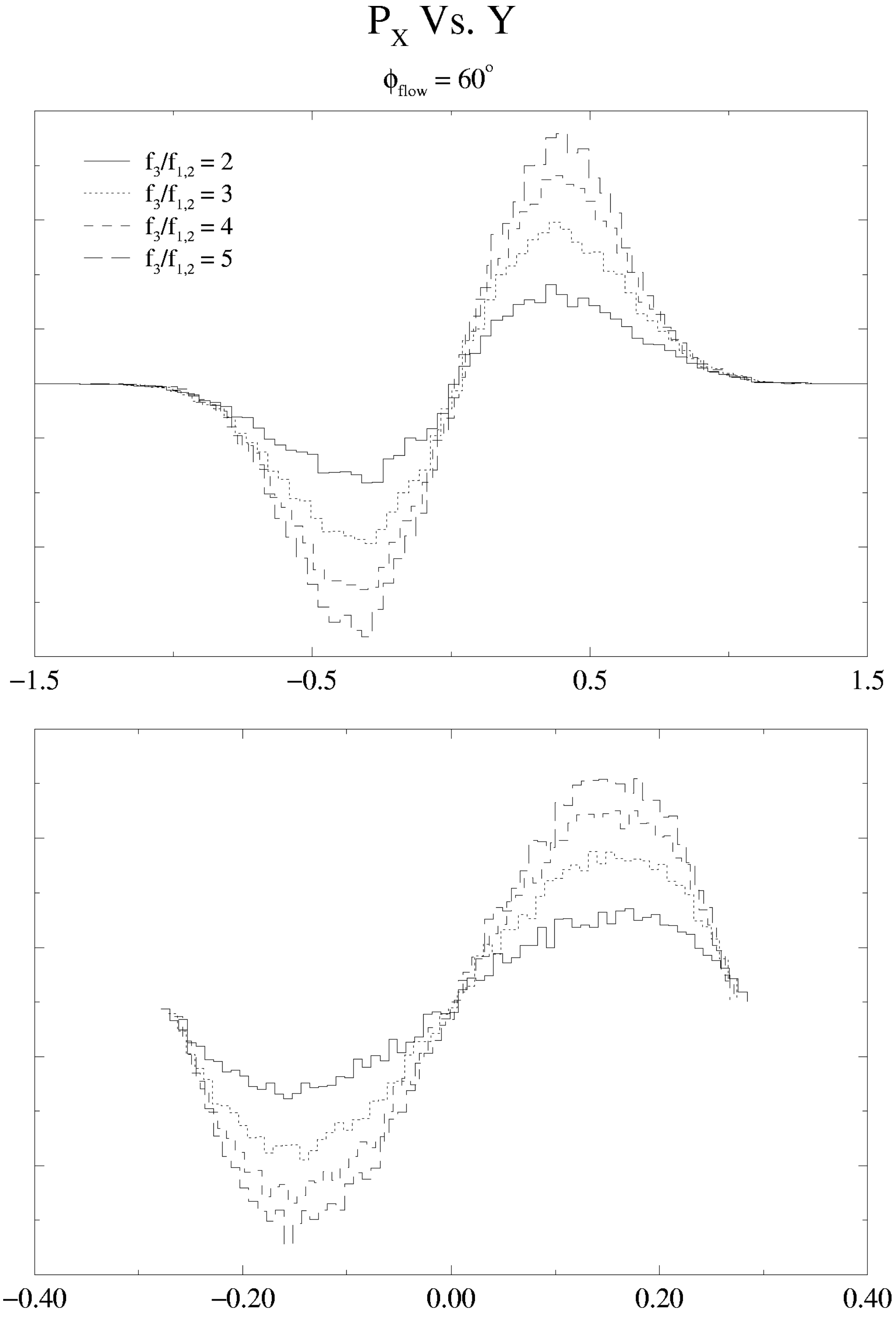

Figure 2.34: Total in-plane, transverse momentum p_x in arbitrary units as a function of rapidity from hypothetical ellipsoids. The upper panel shows results from a Gaussian-ellipsoidal density, whereas the lower panel are results from the uniform ellipsoidal density. Each panel shows $\mathcal{O}(y)$ of ellipsoids rotated various angles ϕ_{flow} relative to the beam axis, but which possess identical kinetic energy ratios.

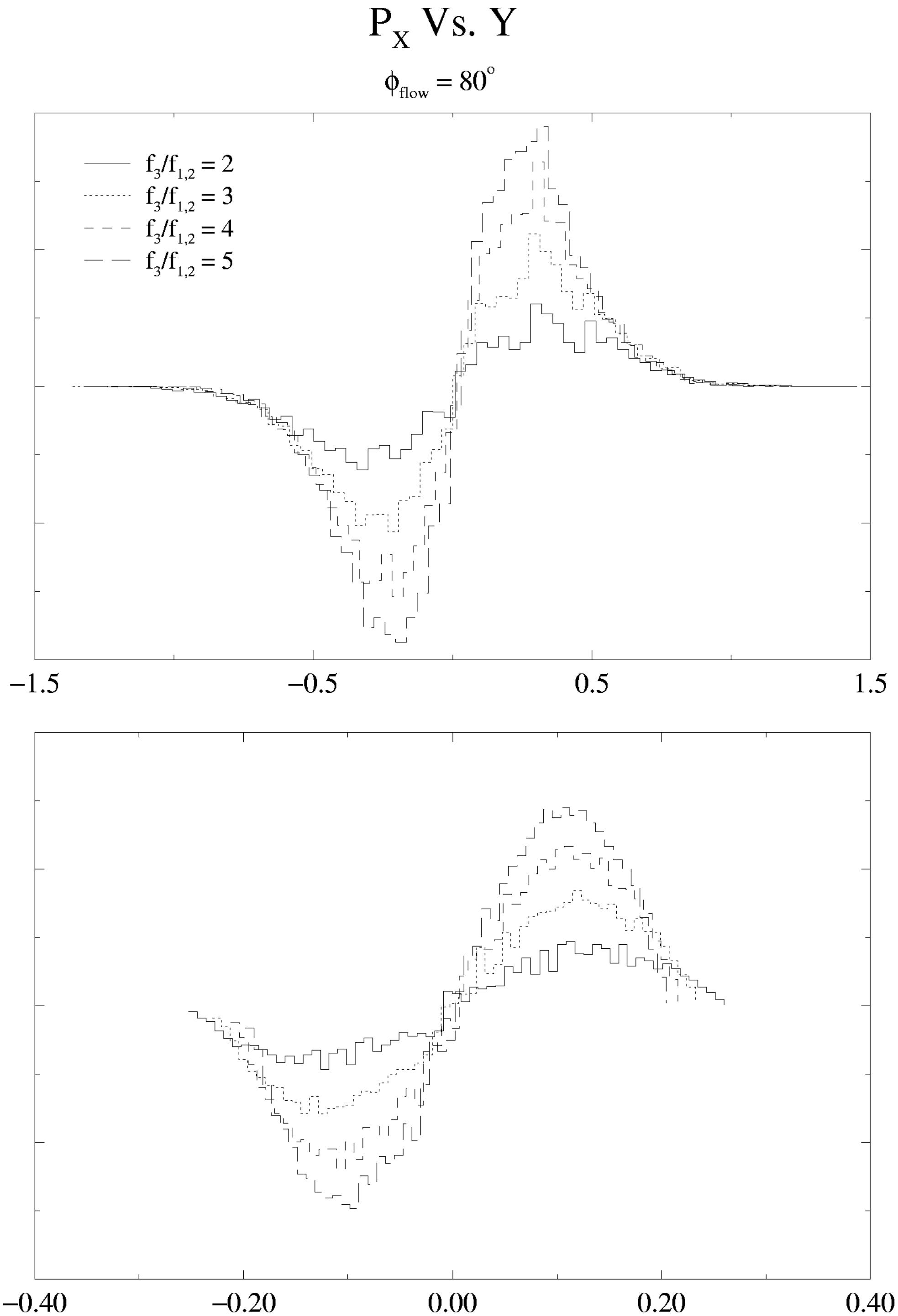

Figure 2.35: Total in-plane, transverse momentum p_x in arbitrary units as a function of rapidity from hypothetical ellipsoids. The upper panel shows results from a Gaussian-ellipsoidal density, whereas the lower panel are results from the uniform ellipsoidal density. Each panel shows $\mathcal{O}(y)$ of ellipsoids rotated various angles ϕ_{flow} relative to the beam axis, but which possess identical kinetic energy ratios.

Summary on $\mathcal{O}(y)$

The total in-plane, transverse momentum as a function of rapidity may be a useful observable in the study of near-central heavy-ion collisions. In the numerical study the slope of the observable near mid-rapidity shows some sensitivity to the shape of the momentum ellipsoid at large flow angles and its orientation. In addition, Equation 2.21 correlates well with the traditional flow values. The shifting of the peaks appears to be more sensitive to changes in the flow angle than changes in the shape of the momentum ellipsoid. Nevertheless, as the flow angle increases for constant flow ratio, the peaks shift toward mid-rapidity. When the flow angles are small and held constant while the flow ratio is increased, the peaks shift away from mid-rapidity. While Equation 2.21 appears to be more sensitive to the particle yield near mid-rapidity, it will also be more sensitive to detector cuts.

2.3.4 Concluding Remarks

One expects the stiffer mean-field to produce more flow at all impact parameters. However, an unexpected enhancement of the flow signal at low-rapidities from ^{197}Au on ^{197}Au collisions at 200 MeV/A was found in BUU calculations using momentum-independent mean-fields. This effect appears energy dependent and practically disappears by 400 MeV/A. The density profiles from time t=1 fm/c to t=60 fm/c were calculated for both momentum-dependent and momentum-independent mean fields at collision energies of 200 MeV/A and 400 MeV/A. These profiles provided important clues to the dynamics underlying this unexpected enhancement in flow.

The shape of the momentum-space distribution is responsible for the suppression of flow in the momentum-dependent calculations–this in spite of their larger flow angles. Generally the larger the flow angle, the larger the flow signal. In addition, the more oblate the momentum distribution for a given non-zero flow angle, the larger the flow signal. Thus there is a competition between the oblateness and the flow angle. In the momentum-dependent calculations it is the oblateness of the distribution that carries the day for low-impact parameters. At higher impact parameters the momentum-dependent calculations still show a more spherical momentum distribution at a given impact parameter. However the higher flow angles overcome this. The end result is higher flow at the larger impact parameters.

It should be noted that this study represents a considerable challenge for experimentalists. Of primary concern are the detector acceptances and their effect on the observables and the precision of their impact-parameter discrimination. Neither are trivial.

2.4 Balance Energy

Flow in lower energy collisions is often negative. That is, the dynamics are attractive overall. The collisions are not violent enough and/or numerous enough and densities are not high enough to overcome the attractive term of the nuclear mean field. As energy is increased the flow signal gradually becomes positive. The point in the flow excitation function where it crosses zero is called the balance energy[Ogi90, Kro92, Wes93, Kla93]. The higher the balance energy for a given system, the more attractive the dynamics. Experimentally one cannot easily distinguish between attractive flow and repulsive flow. For experimental studies the flow signal will approach zero at the balance energy. Often the flow data for beam energies less than the balance energy is reflected across the abscissa to indicate that flow there is negative.

Changes in the model parameters of the BUU model affect the balance energy. The “stiffer”–higher compressibility–the mean field the lower the balance energy, the

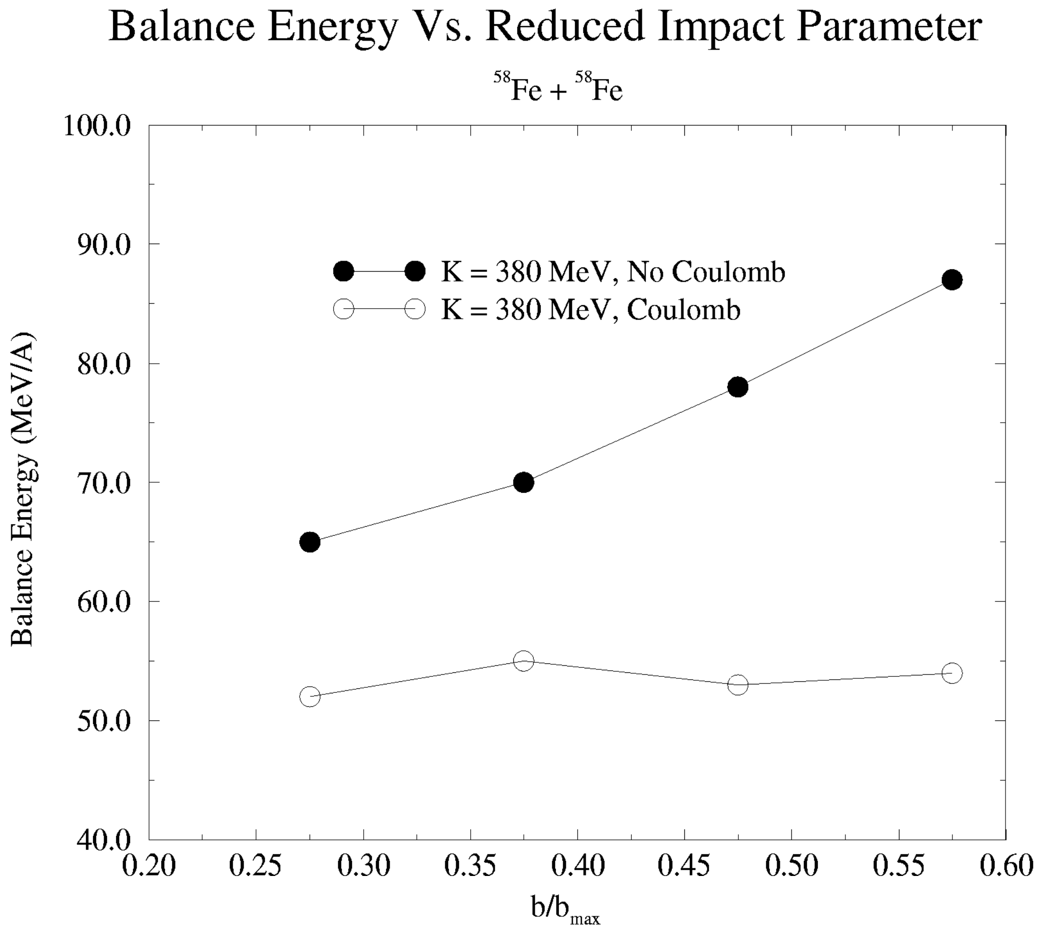

Figure 2.36: Balance energies for ^{58}Fe + ^{58}Fe from BUU model with and without the Coulomb field. Stiff mean field and vacuum nucleon cross sections were used.

smaller the nucleon cross section, the higher the balance energy, the more central the collision, the lower the balance energy. One may thus use the balance energy to learn about the role of the nuclear mean-field and in-medium corrections to the nucleon cross section[Ogi90, Kro92, Wes93, Kla93]. In addition, the mass of the system affects the balance energy. Generally, the higher the mass of the system the lower the balance energy[Wes93].

Figure 2.36 illustrates the suppression of the balance energy from the Coulomb field. The term "Reduced Impact Parameter" (b/b_{max}) is the impact parameter of the collision divided by the maximum impact parameter (the sum of the radii of

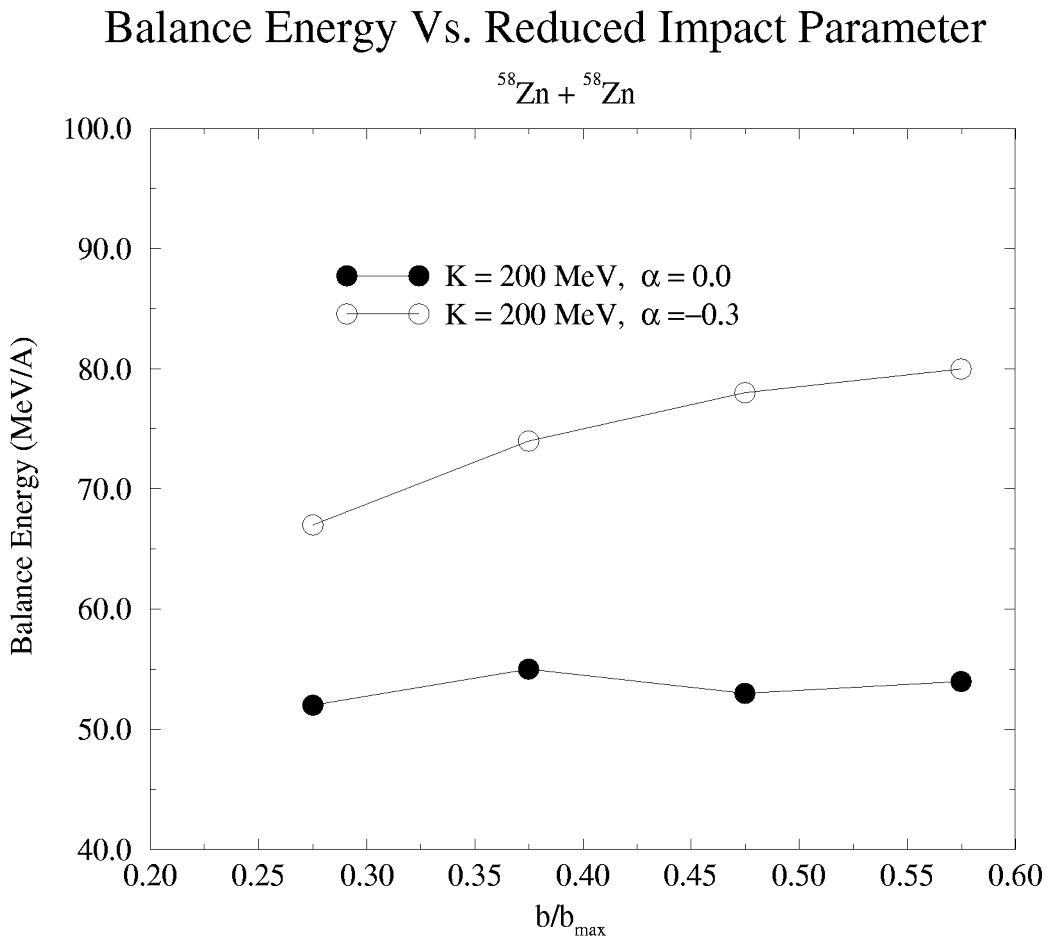

Figure 2.37: Balance energies for ^{58}Zn + ^{58}Zn from BUU model with and without the Coulomb field. Soft mean field was used and in-medium nucleon corrections as indicated.

the nuclei in the collision). At every impact parameter, the balance energy is lower, indicating a generally more repulsive collision, for ^{58}Fe + ^{58}Fe collisions.

The effect of in-medium corrections on the balance energy is shown in Figure 2.37. Here the nucleon cross section is reduced according to Klakow,*et al.*[Kla93], Equation 1.9:

$$\sigma_{nn} = \sigma_{free}(1 + \alpha \frac{\rho}{\rho_0}),$$

where σ_{nn} is the free nucleon cross section. The effect is clear: reducing the cross section raises the balance energy at all impact parameters. This is not surprising since hard scattering is responsible for a great deal of the repulsive nature of collisions at these energies.

2.4.1 Effects of Iso-Spin and In-Medium Corrections on the Balance Energy

It is known that the inter-nucleon potential is iso-spin dependent. That is, it depends, in part, upon whether the nucleon is a proton or a neutron. The T=1 state is unbound for the two-nucleon system, but the state T=0 (deuteron) is bound, if weakly.

Work by Müller and Serot[Mül95] has shown that the liquid-gas phase transition may in fact be of *second* order rather than first order. Their work, based upon a thermodynamic approach, demonstrated that local chemical instabilities are responsible for the transition when an asymmetric potential is used. This contrasts with the common view that mechanical instabilities are responsible for the onset of fragmentation in excited, diffuse systems. The new experimental facilities coming on-line which will probe heavy-ion dynamics near the drip lines affords an opportunity to explore these results.

In stellar evolution the softening of the compressibility of nuclear matter as neutron ratios deviate from 1/2 is critical for generating a supernova explosion for massive stars ($12\,\mathrm{M}_\odot$ to $15\,\mathrm{M}_\odot$)[Bar85]. Core collapse cannot sustain a shock if the nuclear EOS retains its equilibrium stiffness; the result is at least a delay of such important processes as nucleosynthesis.

Neutron stars cool by emitting neutrinos. After an initial fast-cooling phase, they enter a more sedate cooling epoch producing neutrinos via the modified URCA process:

$$\begin{aligned} (n,p) + p + e^- &\rightarrow (n,p) + n + \nu_e, \\ (n,p) + n &\rightarrow (n,p) + p + e^- + \bar{\nu}_e. \end{aligned} \tag{2.22}$$

However, if the proton density exceeds a critical value between 11% and 15%, which is dependent upon the symmetry energy, the direct URCA process can occur and become the dominant cooling mechanism[Lat91]:

$$\begin{aligned} n &\rightarrow p + e^- + \bar{\nu}_e, \\ p + e^- &\rightarrow n + \nu_e. \end{aligned} \tag{2.23}$$

The role of iso-spin in collective observables stems from two sources: an asymmetry in the nuclear mean field, and an asymmetry in the nucleon cross section. The latter is automatically included via the parameterization of the Particle Data Group[PDG88]. The role of the former is studied below.

The effects of an iso-spin asymmetry and in-medium corrections to the nucleon collision cross section on the balance energy were recently explored. The BUU model for intermediate energy heavy-ion collisions is used with mean fields featuring iso-spin asymmetry to calculate the balance energies of ^{58}Fe + ^{58}Fe and ^{58}Ni + ^{58}Ni for a range of impact parameters. We find better agreement with experiment with these mean fields and a reduction in the in-medium nucleon cross section. Unfortunately, we fail to find significant differences in the balance energies between the ^{58}Fe + ^{58}Fe calculations and the ^{58}Ni + ^{58}Ni calculations. This is at variance with recent work from R. Pak, Bao-An Li, *et al.*[Pak97].

In this study, we choose two mean fields: One recently used by Bao-An Li, *et al.*[Li95, Li96a] (also see Ref. [Tsa89, Dan92, Li93]):

$$U = A\left(\frac{\rho}{\rho_0}\right) + B\left(\frac{\rho}{\rho_0}\right)^{\sigma} + C\tau_z\left(\frac{\rho_n - \rho_p}{\rho_0}\right), \tag{2.24}$$

where ρ_0 is the normal nuclear density, ρ_n is the neutron density, ρ_p is the proton density, and τ_z is the iso-spin factor which is 1 for neutrons and -1 for protons. Coefficients A, B and σ are typically chosen to match the ground state properties of symmetric nuclear matter such as the saturation density and saturation binding energy. The compressibility is a free parameter, and in this study we choose it to be 200MeV. This gives $A = -109$MeV, $B = 82$MeV, and $\sigma = \frac{7}{6}$. In keeping with Bao-An Li's work, $C = 32$MeV.

The other mean field is derived from a Hamiltonian due to Sobotka[Sob94]:

$$\mathcal{H} = \mathcal{KE} + \frac{4a}{\rho_0}({\rho_n}^2 + b\rho_n\rho_p + {\rho_p}^2) + \frac{4c}{\rho_0}({\rho_0}^2\rho_p + \rho_n{\rho_p}^2). \tag{2.25}$$

Here the coefficients $a = -3.66$MeV, $b = 15.0$ and $c = 23.4$MeV and $\mathcal{KE}$ is the kinetic energy term. Neutrons are acted upon by:

$$U_n = \frac{\partial\mathcal{H}}{\partial\rho_n} = 8a\frac{\rho_n}{\rho_0} + 4ab\frac{\rho_p}{\rho_0} + 8c\frac{\rho_n\rho_p}{{\rho_0}^2} + 4c\frac{{\rho_p}^2}{{\rho_0}^2}, \tag{2.26}$$

whereas protons are affected by:

$$U_p = \frac{\partial\mathcal{H}}{\partial\rho_p} = 8a\frac{\rho_p}{\rho_0} + 4ab\frac{\rho_n}{\rho_0} + 8c\frac{\rho_n\rho_p}{{\rho_o}^2} + 4c\frac{{\rho_n}^2}{{\rho_0}^2}. \tag{2.27}$$

In symmetric matter, this mean field reduces to the often-called "Stiff" equation of state (compressibility 380MeV). It should be noted that there is no transformation of the Sobotka mean field that will yield an equivalent "Soft" equation of state. Thus direct comparisons between the two formulations are impossible. One may simply alter A, B and σ in Equation 2.24 to give the appropriate compressibility in symmetric matter.

With

$$\delta = \frac{\rho_n - \rho_p}{\rho_0} \tag{2.28}$$

and

$$\tilde{\rho} = \frac{\rho}{\rho_0} \tag{2.29}$$

Equations 2.24 and 2.26 can be written as:

$$U = A\tilde{\rho} + B\tilde{\rho}^{\sigma} + C\tau_z\delta \tag{2.30}$$

and

$$U_n = \tilde{\rho}(4a + 2ab) + \delta(4a - 2ab) - c\delta^2 + 3c\tilde{\rho}^2 - 2c\delta\tilde{\rho}, \tag{2.31}$$

for the neutron potential, and

$$U_p = \tilde{\rho}(4a + 2ab) + \delta(2ab - 4a) - c\delta^2 + 3c\tilde{\rho}^2 + 2c\delta\tilde{\rho}, \tag{2.32}$$

where a, b and c are as defined above. Figure 2.38 shows Equation 2.30 as neutron excess and normalized nuclear density are varied, left-hand plot, and Equation 2.31 as neutron excess and normalized nuclear density are varied, right-hand plot. One can see in the Figure that Equation 2.31 is more attractive to neutrons in the midst of proton-rich matter for all densities than Equation 2.30.

The nucleon-nucleon cross sections are parameterization from the Particle Data Group[PDG88] with medium modification implemented according to Equation 1.9:

$$\sigma_{nn} = \sigma_{nn}^{free}(1 + \alpha\,\frac{\rho}{\rho_0}),$$

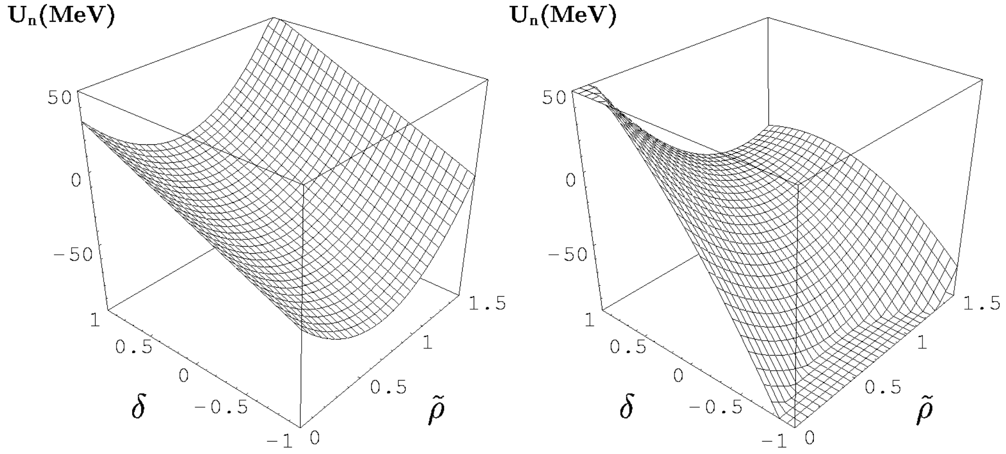

Figure 2.38: Mean fields due to Bao-An Li, *et al.*[Li95, Li96a], left panel, and Sobotka[Sob94]. δ is defined in Equation 2.30, and is often referred to as the neutron excess. $\tilde{\rho}$ is the normalized symmetric density ρ/ρ_0.

where α is varied between -1 and 0, ρ_0 is normal nuclear matter density and where ρ is the nuclear matter density in the neighborhood of the collision[Kla93, Alm95]. This is a parameterization of the Pauli-blocking of intermediate states in Bückner G-matrix theory[Brü55].

We begin by calculating the proton freeze-out (recall that "freeze-out" refers to the point in the evolution beyond which few hard collisions remain) phase-space distribution at reduced impact parameters $\hat{b} = b/b_{max} = 0.275, 0.375, 0.475$ and 0.575, beam energies $50, 60, 70, 80, 90$ and 100 MeV/A, using Equations 2.24 and 2.26 and various in-medium corrections α. This is followed by calculating the flow for each permutation, and finally the balance energy for each $\hat{b}$.

It has been shown that an in-medium reduction of about 20% tends to best reproduce the flow signals of symmetric collisions for a broad range of energies[Ogi90, Kla93, Wes93]. Previous work[Ogi90, Kla93, Wes93] showed the BUU model consistently under-predicted the balance energies of various systems. R. Pak, *et al.*[Pak97] found BUU under-predicted the balance energies of ^{58}Fe + ^{58}Fe and ^{58}Ni + ^{58}Ni collisions. We introduce this correction to the nucleon cross section to our calculations in anticipation of raising the balance energies at all impact parameters. Figure 2.39 shows the effect of the in-medium correction $\alpha = -0.3$ for BUU calculations using the mean field from Equation 2.24. Notice that the effect diminishes as the impact parameter increases. It can be argued that that this is due to the diminishing role collisions tend to play in the overall dynamics of the nucleus-nucleus collision. The calculation also suggests a contraction of the difference in balance energies between the relatively neutron-rich ^{58}Fe and the relatively neutron-poor ^{58}Ni, although there is a widening at the highest impact parameters. At near central collisions, the combination of in-medium reduction of the cross section and the inclusion of the asymmetry energy in the mean field better reproduces the experimental data in Figure 2.40. However, the model still tends to under predict the experimental data for more peripheral collisions.

The trend of the balance energies is more linear, suggesting that the loss of repulsive dynamics from fewer collisions in the dense regions of the collision volume is partially compensated by an additional repulsive contribution from the mean field. Since both species studied here are slightly neutron rich, then, as the density is driven higher by ever smaller cross sections (remember for these calculations the cross section is 30% reduced at nominal density and is smaller still at higher densities), the asymmetry term, along with the usual Skyrme terms, in Equation 2.24 grow ever more repulsive. This would tend to reduce the upward surge of balance energies at higher impact parameters. Any further reduction of the cross sections would likely result in a further divergence in this trend from experiment.

Figure 2.42 compares BUU calculations using the stiff mean field without

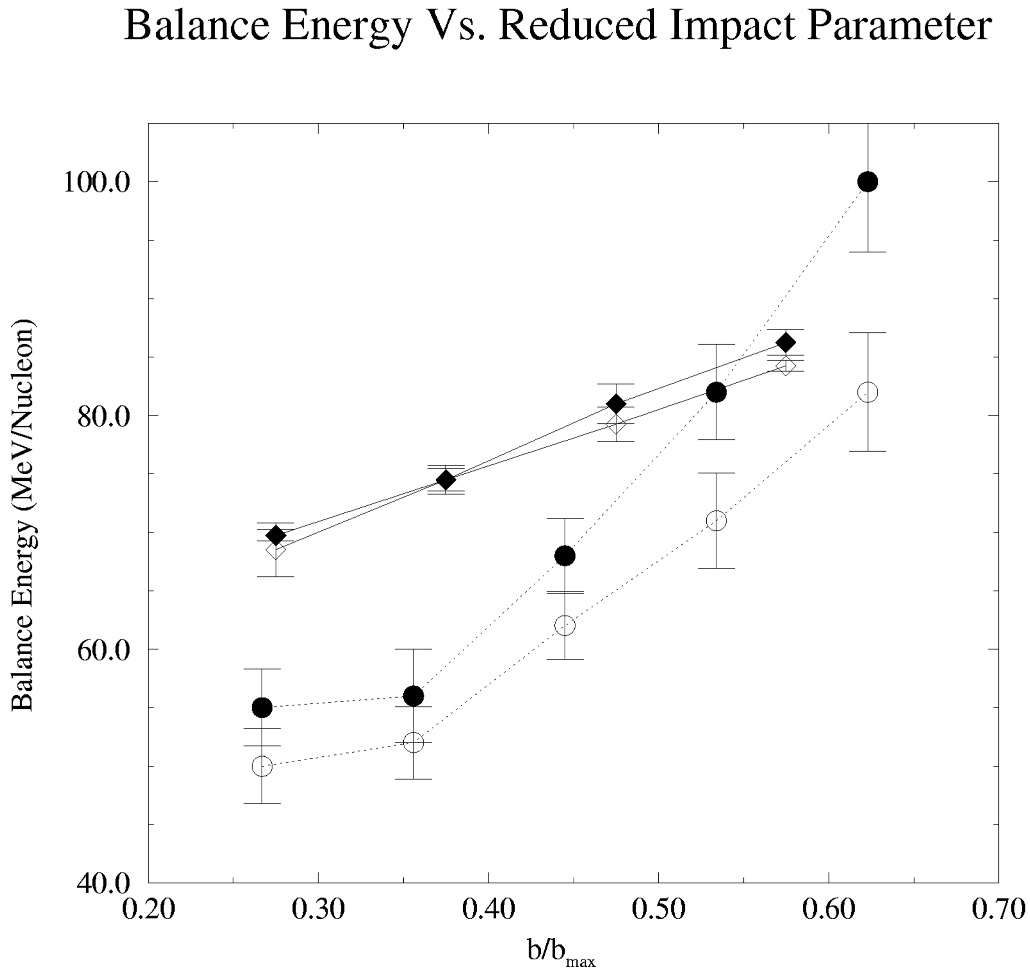

Figure 2.39: Balance energy versus reduced impact parameter for ^{58}Fe + ^{58}Fe, solid points, and ^{58}Ni + ^{58}Ni, open points. Diamonds are BUU calculations using Equation 2.24 with a 30% in medium reduction factor, α, for the nucleon cross section. Circles are BUU calculations[Pak97] with the same mean field but with the vacuum nucleon cross section.

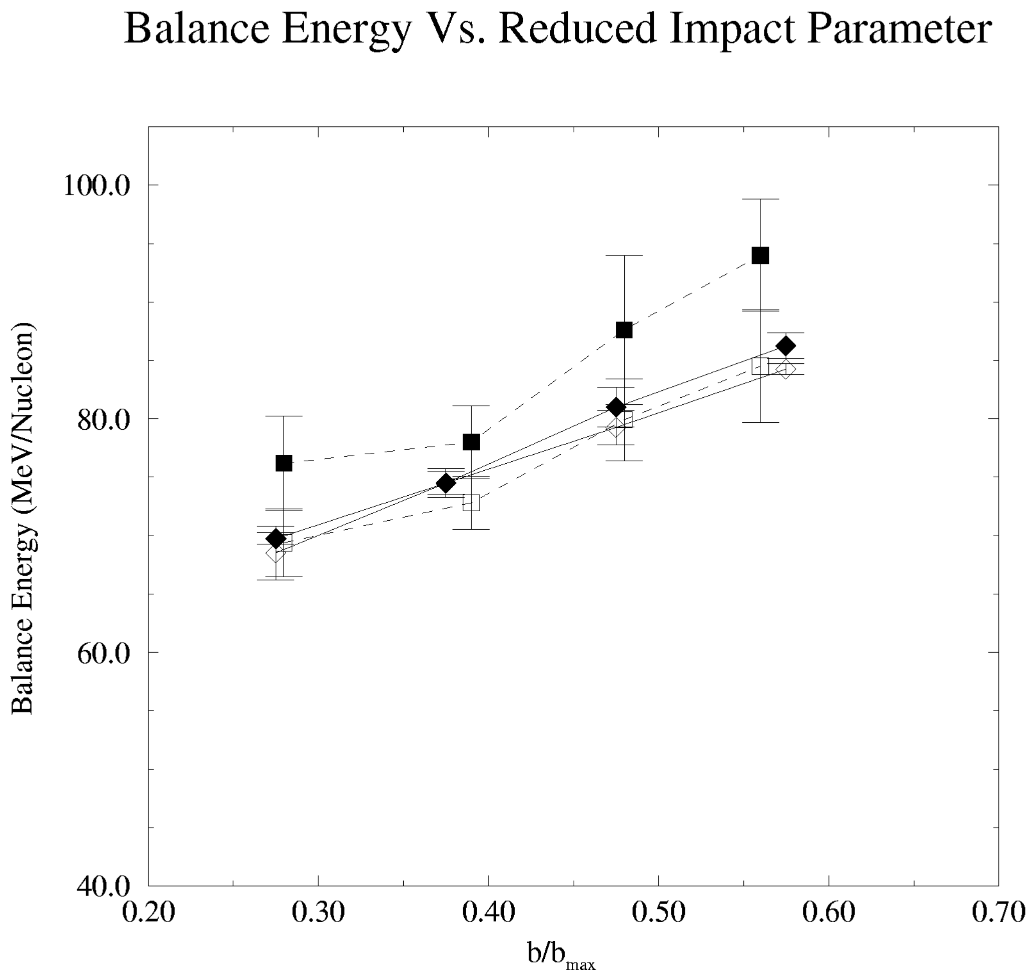

Figure 2.40: Balance energy versus reduced impact parameter for ^{58}Fe + ^{58}Fe, solid points, and ^{58}Ni + ^{58}Ni, open points. Squares are empirical data[Pak97], diamonds are from calculations using the BUU model with Equation 2.24 as a mean field and an in-medium correction factor $\alpha = -0.3$.

asymmetry corrections and an in-medium reduction factor of 20% to experiment[Pak97]. Here too we find a collapse of the ^{58}Fe balance energies onto the ^{58}Ni balance energies for low impact parameters, and a progressive separation at higher impact parameters. That this occurs in calculations using Equation 2.24 and those using the plain, stiff mean field could indicate a weakness of the overall effect the asymmetry terms in Equation 2.24. However, in asymmetric matter the asymmetry term makes the dynamics more repulsive overall. Thus, Bao-An Li's mean field, which is just the soft mean field plus a linear asymmetry term, behaves more like the stiff mean field without the asymmetry correction.

Figure 2.41 compares the balance energies calculated using the Sobotka mean field and an in-medium correction factor, $\alpha = -0.2$, with experimentally measured[Pak97] balance energies. At low impact parameters the BUU calculations perform well. However, there is a curious flip-flop in the calculated balance energies as impact parameters increase. At the lowest impact parameter, the BUU calculations are well within the reported experimental uncertainties. The ordering switches at $\hat{b} = 0.375$; the ^{58}Ni + ^{58}Ni balance energies are higher than ^{58}Fe + ^{58}Fe balance energies, contrary to experiment. The ordering switches again at $\hat{b} = 0.475$ and remains consistent with experiment to the end of the range of the impact parameters studied.

Figure 2.43 illustrates the differences in balance energies as a function of impact parameter between BUU calculations using the stiff mean field without any asymmetry correction and BUU calculations using Equation 2.26, Sobotka's mean field. Note that both sets of calculations use $\alpha = -0.2$. The two pairs of curves are similar for the higher impact parameters studied. The two pairs of curves quite close to each other at the lower impact parameters, except for the flip-flop in the ordering of the balance energies of the species in the calculations using the Sobotka mean field. The similarity of the calculated balance energies may diminish when species near the drip

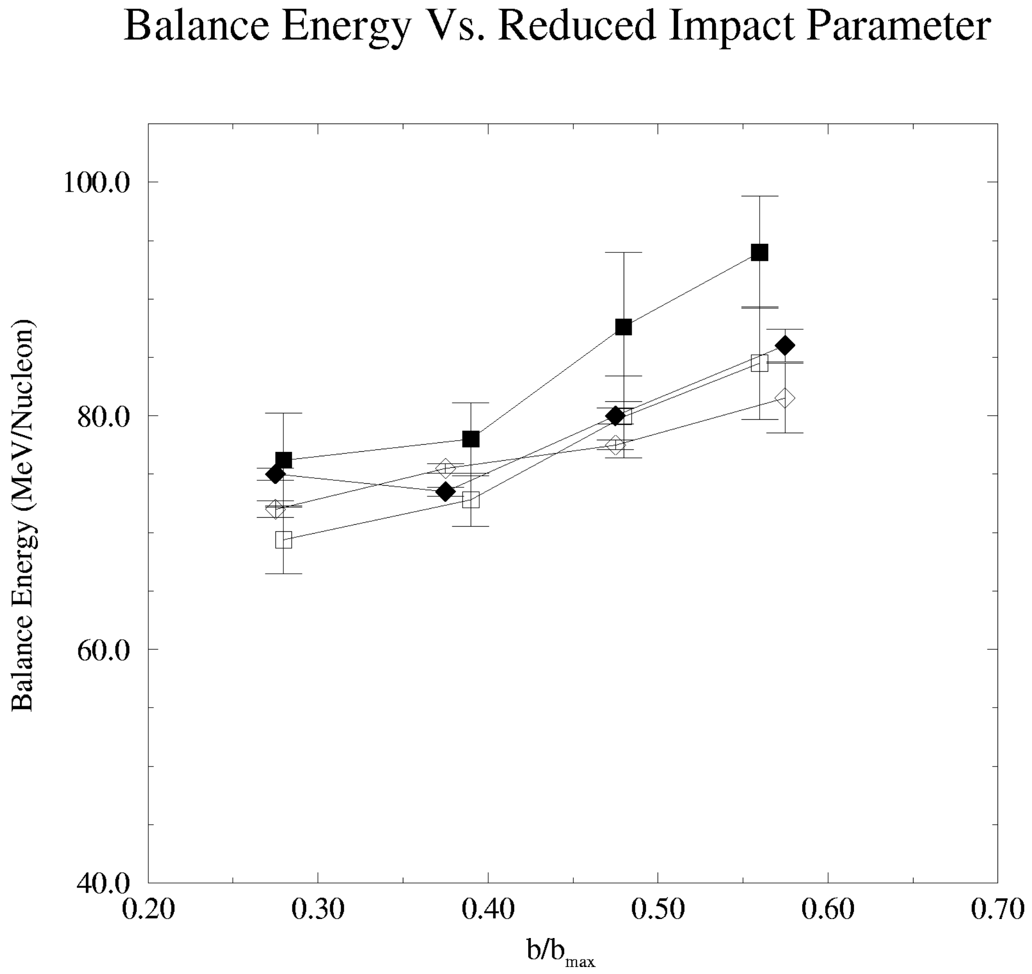

Figure 2.41: Balance energy versus reduced impact parameter for ^{58}Fe + ^{58}Fe, solid points, and ^{58}Ni + ^{58}Ni, open points. Squares are empirical data[Pak97], and diamonds are BUU calculations using Equation 2.26 and an in-medium correction factor, $\alpha = -0.2$.

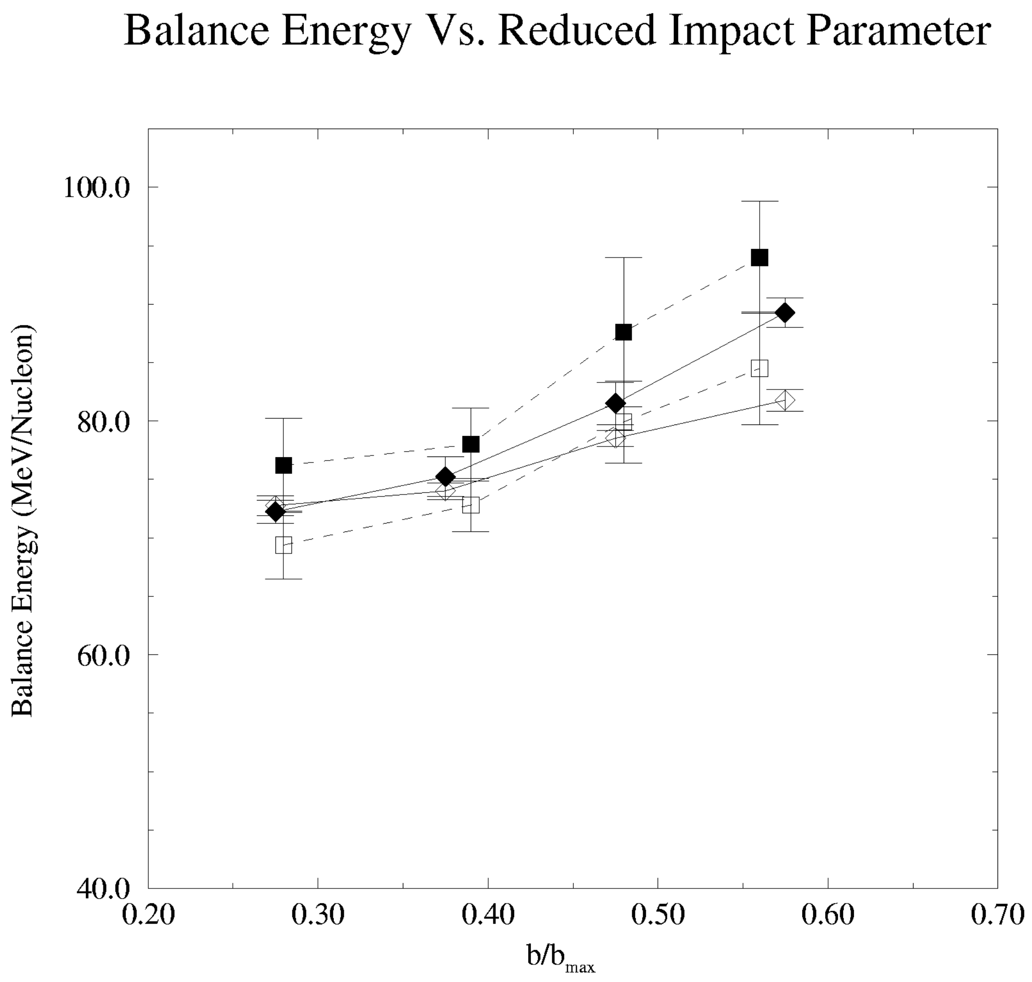

Figure 2.42: Balance energy versus reduced impact parameter for ^{58}Fe + ^{58}Fe, solid points, and ^{58}Ni + ^{58}Ni, open points. Squares are empirical data[Pak97], and diamonds are BUU calculations using the stiff mean field without asymmetry corrections and an in-medium correction factor, $\alpha = -0.2$.

lines are studied. This anticipates experiments using the new radioactive beams.

There is a curious feature of the Figure in the differences between the balance energies calculated with the mean field from Bao-An Li and those calculated with the mean field from Sobotka. Notice that the differences among the ^{58}Ni + ^{58}Ni calculations are greatest at low impact parameters and smallest at high impact parameters. However, the reverse is true for the ^{58}Fe + ^{58}Fe calculations.

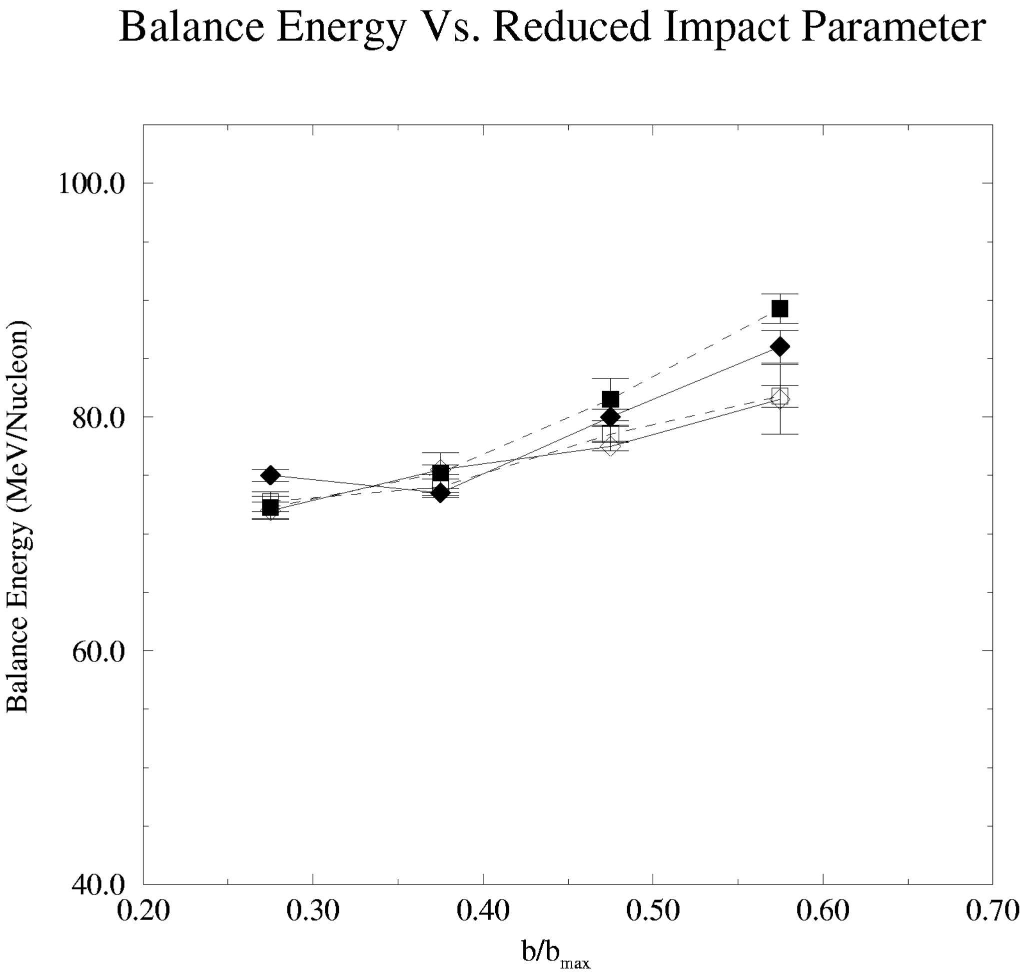

Figure 2.43: Calculated balance energies using the BUU model. Solid points are ^{58}Fe + ^{58}Fe and open points are ^{58}Ni + ^{58}Ni. Diamonds represent calculations using Equation 2.26 as the mean field with $\alpha = -0.2$, and squares represent calculations using the stiff mean field without asymmetry corrections and with $\alpha = -0.2$.

2.5 Summary

This Chapter began with a detailed discussion of the configuration-space and momentum-space evolution typical of relativistic, heavy-ion collisions, then introduced two directed, collective observables. The more common of the two, introduced by Danielewicz and Odyniec[Dan85] and called directed transverse flow, or just "flow", is the slope at mid-rapidity of the average in-plane, transverse momentum versus rapidity. This quantity has demonstrated a sensitivity to the directed collective dynamics of intermediate energy, heavy-ion collisions.

However, an unexpected result was found in the comparison of flow values for momentum-dependent and momentum-independent ^{197}Au on ^{197}Au collisions at 200 MeV/A. Normally momentum-dependence adds to the repulsive elements in the evolution of heavy-ion collisions. But the momentum-dependent calculations yielded smaller flow values than those of momentum-independent calculations.

A qualitative study of the evolution of the density of these collisions was undertaken. It suggested that the momentum-space distributions for the momentum-dependent calculations may be more spherical in shape than those distributions from momentum-independent calculations.

Sphericity analysis was then used to get a quantitative picture of this hypothesis. Indeed, the momentum-dependent calculations showed a more spherical distribution than the momentum-independent calculations. In addition, the momentum-dependent distributions showed greater flow angles than those of the momentum-independent distributions. Thus, in spite of higher flow angles, which usually generally give higher flow values, the lesser oblateness of the momentum-dependent distributions lead to lower flow values.

This leads to a proposal of an apparently new observable: the total in-plane, transverse momentum versus rapidity. This quantity was studied in detail, and it was found to be sensitive to both the orientation and the shape of the momentum distribution. However, the slope of this observable is also more sensitive to population distributions. This could present difficulties if detector cuts become obtrusive.

Finally, this Chapter carried out a study of the behavior of the balance energy for ^{58}Fe on ^{58}Fe and ^{58}Ni on ^{58}Ni using an iso-spin dependent nuclear mean field and in-medium corrections to the nucleon-nucleon scattering cross section. Two iso-spin dependent mean fields were studied: one from Sobotka[Sob94] and one from the work of Bao-An Li[Li95, Li96a]. The inclusion of in-medium corrections improved the performance of both mean fields, but Sobotka's best matched experimental work[Pak97].

The next chapter introduces an hybridization of BUU and a simple coalescence model. A study of collective, non-directed behavior is then presented and the consequences discussed.

Chapter 3

BUU, Coalescence and the Radially Expanding Thermal Model

3.1 Introduction

The collective phenomena discussed thus far have been of a directed nature. In other words it has a definite direction in momentum-space. However, isotropic radial expansion is common in our universe. A system's rate of expansion can tell us about the forces driving its evolution. It is then easy to wonder what radial expansion can tell us about the forces driving the evolution of heavy-ion collisions.

In experiments conducted at Berkeley, Mike Lisa and the EOS-TPC collaboration[Lis95] found evidence for a radial component and a thermal component in the velocity profiles of light fragments (deuterons, tritons, ^{3}He's and alphas) emitted near mid-rapidity. The collisions studied were Au + Au at energies ranging from $0.025 - 2\,\mathrm{GeV/A}$. They choose the most central events, those which exhibited the highest multiplicities, with an estimated range of impact parameters of $0\,\mathrm{fm}$ to $3\,\mathrm{fm}$.

Recall that the BUU transport model, while having been quite successful in predicting and explaining directed phenomena of single-particle observables[Ber87, Gale90, Wes90], possesses no self-consistent means of treating two-body forces. The Coulomb field is treated classically, since this is easily done with today's computers, and hard scattering among nucleons is well modeled. A single-particle mean field is used to model soft processes arising from the cumulative effects of multiple two-body interactions. However, the BUU formalism has no self-consistent means of treating the N-body phase-space. In an effort to correct this deficiency in BUU, we chose a simple coalescence algorithm. When applied to the single-particle freeze-out phase-space distribution from BUU, the algorithm will provide the momentum-space distribution of light fragments.

Several questions suggest themselves regarding the hybridization of BUU and a simple coalescence model: how well, if at all, can this combination of models perform? Can they predict or reproduce experimental data? Will they give us insight into the inner workings of heavy-ion collisions? The subject of this chapter is a study which seeks to answer some of these questions.

The thermalization of nuclear matter in heavy-ion collisions is not complete. That this is so is easily seen in momentum-space scatter plots of test particles, Figures 2.3 and 2.5 of Chapter 2. The common volume of the two colliding nuclei can be well characterized as having a single temperature. However, the spectator matter is still quite "cold". This matter still carries much of its original beam momentum. The few collisions that the nucleons within these spectator regions have suffered have meant little opportunity for the conversion of longitudinal momentum to random or thermalized momentum. Thus, one would not expect a strong radial velocity profile to manifest from regions of high or low rapidity. However, near mid-rapidity directed signals can be expected to give way to a radial expansion, and it is near mid-rapidity that the EOS-TPC collaboration focus its efforts. And this is where we focus our efforts.

We use a coalescence model to produce the momentum-space distribution of free protons, deuterons, tritons, ^{3}He and alpha particles. Then, using χ^2/ν minimization, we fit the resulting spectra to thermal yet radially expanding distributions to assign a common temperature and expansion velocity for the entire collision volume.

The next section details the models and calculations we use in the study; Sections 3.3 and 3.4 are presentations of our results and comparison to experimental data, and in Section 3.5 we draw our conclusions.

3.2 Models and Calculations

The nuclear mean field we use in this study takes the form of Equation 1.6[Wel88]:

$$U(\rho,\vec{p}) = A\left(\frac{\rho}{\rho_0}\right) + B\left(\frac{\rho}{\rho_0}\right)^{\sigma} + \frac{C}{\rho_0}\int d^3p' \frac{f(\vec{r},\vec{p}')}{1+\left(\frac{\vec{p}-\vec{p}'}{\Lambda}\right)^2}$$

It can be modeled with various combinations of force parameters leading to different compressibilities, in addition to toggling the momentum dependence. Values for the parameters in Equation 1.6 are shown in Table 2.1.

In an effort to exclude spectator matter, fragements with momenta outside $\theta_{cm} = 90° \pm 15°$ relative to the beam axis are excluded. The excluded matter will undergo directed flow and likely contaminate the thermal signature of the participant matter. We mimic this acceptence in our efforts to test BUU and simple coalescence. In addition, our calculations concentrate on impact parameters 0 fm to 3 fm. Experimental efforts cannot easily characterize the impact parameter of an event. We use a geometrical weighting of

$$N_{b_i} = \frac{b_i}{b_j} N_{b_j} \tag{3.1}$$

where N_{b_i} is the weight of events at an impact parameter b_i, and N_{b_j} is the weight of events at an impact parameter b_j. Thus, there should be 3 times as many collisions calculated at an impact parameter of 3 fm as there are at 1 fm. This does imply that there will be no events at zero fm. Central collisions are often calculated for the insight they provide by virtue of their symmetry.

Since the EOS-TPC collaboration focuses its attention on the spectra of light fragments in addition to that of protons, a coalescence model is needed. The algorithm converts the freeze-out phase-space distribution of protons and neutrons into a phase-space distribution of light fragments.

The coalescence of light fragments followed a simple, and some may say naive, prescription: should two or more nucleons of the right species fall within a critical radius, ΔR, in configuration-space and a critical radius, ΔP, in momentum-space, the group will constitute a fragment. The critical radius in configuration-space for heavier fragments is simply increased according to $R_i \propto A_i^{1/3}$, where i is the fragment species, while the critical radius in momentum-space remains 100 MeV/c.

This prescription for coalescence is not original[Kru85, Nag94], although it represents something of a departure from what is more common at these energies: a momentum-space coalescence[But63, Mek77, Kap80, Das81, Sat81, Cse86]. The success of momentum-space coalescence at intermediate energies is well documented[Sch63, Gos77, Lem79, Jac84, Tsa88, Wan95]. The additional constraint, ΔR, allows one to explore coalescence calculations where the source size exceeds that of the fragments emitted[Bar94, Sor95]. However, source sizes at energies ~1 GeV/A are expected to be of the same order as the fragments emitted from them, effectively negating the need for a constraint in configuration-space[Wan95]. Indeed, in our work to fix the coalescence parameters, we find the spectra to have little sensitivity to changes in ΔR.

The coalescence model we use here produces light fragments, all at the same time coordinate, propagates them to infinity free of mutual interaction or interaction with the spectator system, and without the possibility of decay from excited states to ground states. This is equivalent to making non relativistic and sudden approximations, in addition to assuming that chemical equilibrium is reached for all the fragments, regardless of species, at the same time. It is free, however, from assumptions about thermal equilibrium, local or otherwise, light fragment potentials and source sizes.

The sudden approximation is probably a good one[Mek77] and has been used extensively in the older models. It has the advantage of being relatively simple to code and minimizes the combinatorial burden. There are more sophisticated coalescence models[Kap80, Dov91, Llo95] which are less cavalier in their presumptions about the conditions under which fragmentation, coalescence and clustering occur. And the imposition of a coalescence "after-burner" upon the phase-space distribution evolved using transport codes barren of strong multiparticle interaction fails to answer questions regarding the role of clustering before freeze-out, though alternatives do exist[Dan91, Dan95].

The spectra of protons, deuterons, tritons, ^{3}He and alphas are analyzed using a radially expanding thermal model[Sie79]. In this model the fragments are assumed to possess a thermal velocity distribution characterized by a temperature in Maxwell-Boltzmann statistics, and an overall radial velocity. In the global rest frame the resultant distribution is

$$\frac{d^3N}{dp^3} \sim \exp\left(-\gamma E/T\right)\left[\left(\gamma + \frac{T}{E}\right)\frac{\sinh(\alpha)}{\alpha} - \frac{T}{E}\cosh(\alpha)\right], \qquad (3.2)$$

where $\gamma \equiv 1/\sqrt{1-\beta^2}$, $\alpha \equiv \gamma\beta p/T$, T is temperature and $\beta \equiv v/c$ is the radial flow velocity. The spectra are fitted to Equation 3.2 by fixing the overall normalization and varying T and β to obtain a minimum χ^2/ν. Global fits constitute simultaneous fits to deuterons, ^{3}He, tritons, and alphas, since we use the proton spectrum to fix the critical radii for coalescence. Critical radii are fixed by minimizing the difference between the final-state proton spectra from the BUU calculation and that from the EOS-TPC study[Lis95] at 1 GeV/A. We find $\Delta\, R_{deuteron} = 1.5\,\mathrm{fm}$ and $\Delta\, P = 100\,\mathrm{MeV/c}$. These values are of the same order of magnitude as length and momentum parameters used in other coalescence models[Nag96, Jac84].

In addition to the impact-parameter averaged study, we perform calculations probing the relative importance of the various features the BUU transport model in terms of their effect on radial flow velocity and temperature. Calculations are again of Au + Au, but restricted to $b = 2\,\mathrm{fm}$, a beam energy of 1 GeV/A, using various nuclear mean fields, with and without Coulomb fields, and various reductions in the nucleon-nucleon cross section.

The effect of Δ-resonances is also studied since the decay products receive an extra kick, and this may be visible in the proton spectra. By tagging those protons the last interaction of which before freeze-out was a recoil from Δ-decay, and by removing them from the BUU output we are able to isolate their influence on the overall proton spectra. Our results are presented below.

3.3 Results

Our results for the impact-parameter-averaged calculations for 1GeV/A appear in Figure 3.1. The temperature and radial flow velocities are consistent with those obtained in experiment[Lis95] within uncertainties, and provides good evidence that BUU+coalescence is capable of reproducing this combination of radial and thermal motion in light fragments. Our simultaneous fit to the fragment spectra with a nonzero radial flow velocity gives a minimum χ^2/ν of 1.3. Forcing a zero radial flow velocity yields a minimum χ^2/ν of 1.8, in keeping with, though not as dramatic as, the results of the EOS-TPC study[Lis95]. Without absolute cross sections, normalizations are free parameters in our minimization of χ^2/ν-fit.

We extend our impact-parameter-averaged investigation to energies 250 MeV/A, 600 MeV/A, 1.5 GeV/A and 2 GeV/A. The results are presented in Figure 3.2. Here one can see that results from the calculations have significant overlap with experiment. Temperatures extracted from BUU+coalescence calculations agree well with those extracted from experiment, whereas our results for radial flow velocity agree less well. They do suggest a saturation of radial flow velocity as beam energy is increased beyond 1 GeV/A. Other models show a saturation at higher energies[Li96b]. This is consistent with AGS data[Har95].

The microscopic features of the BUU transport code seem to have little influence on the radial flow velocity. We calculate the temperatures and radial flow velocities for reactions with an impact parameter of 2 fm and an energy of 1 GeV/A. The results of the study are presented in Table 3.1. Immediately, one can see the insensitivity of radial flow velocity to the equation of state and the in-medium modification of the nucleon-nucleon cross section. The numerical models used in the EOS-TPC study[Lis95] also showed the radial flow velocity to have little dependence on the equation of state (EOS) used. Indeed, we cannot discern any significant EOS dependence. Radial flow will not develop within $\theta_{cm} = 90^\circ \pm\ 15^\circ$ of the beam axis without nucleon-nucleon collisions. For calculations at $b = 2$ fm and E_{beam}=1 GeV/A that are allowed to reach maximum compression before σ_{nn} is set to zero, almost no baryons obtained rapidities low enough to meet the kinematic selection criteria. However, we do see evidence of directed flow. Thus we conclude that both nuclear mean fields and nucleon-nucleon collisions are important in the development of radial flow, and that it is likely that they provide roughly equal contributions to radial flow. We find

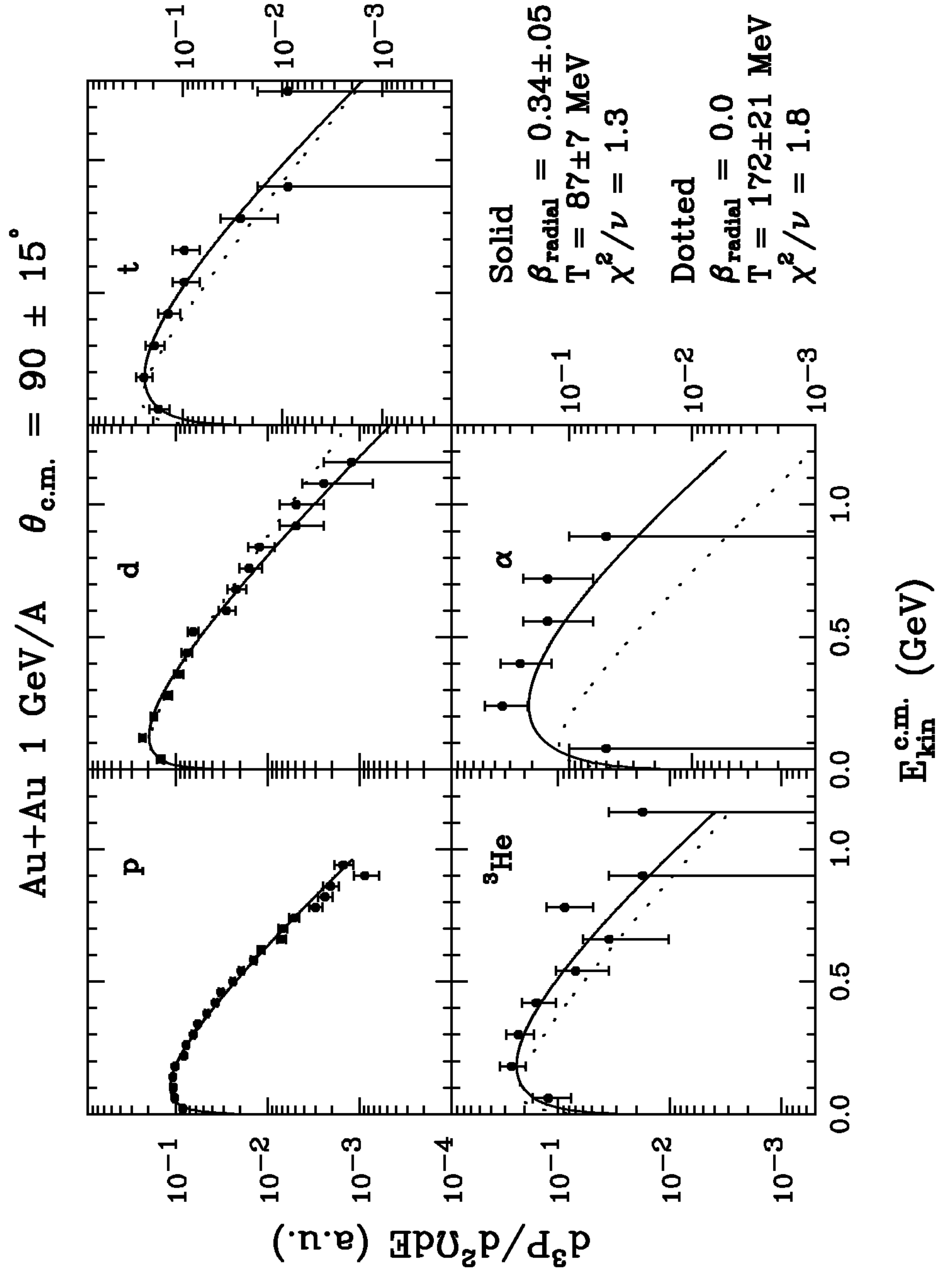

Figure 3.1: Spectra of BUU + coalescence for impact parameter averaged Au + Au collisions with $b \leq 3\,\mathrm{fm}$. The ^{197}Au + ^{197}Au phase-space is calculated using a momentum-dependent stiff equation of state from Table 2.1 and the free nucleon cross sections[PDG88]. Global temperature and radial flow velocity are obtained by fitting the radially expanding thermal model[Sie79] to deuterons, tritons, ^{3}He, and alphas simultaneously. Dotted lines are the global fits for a radial flow velocity of zero.

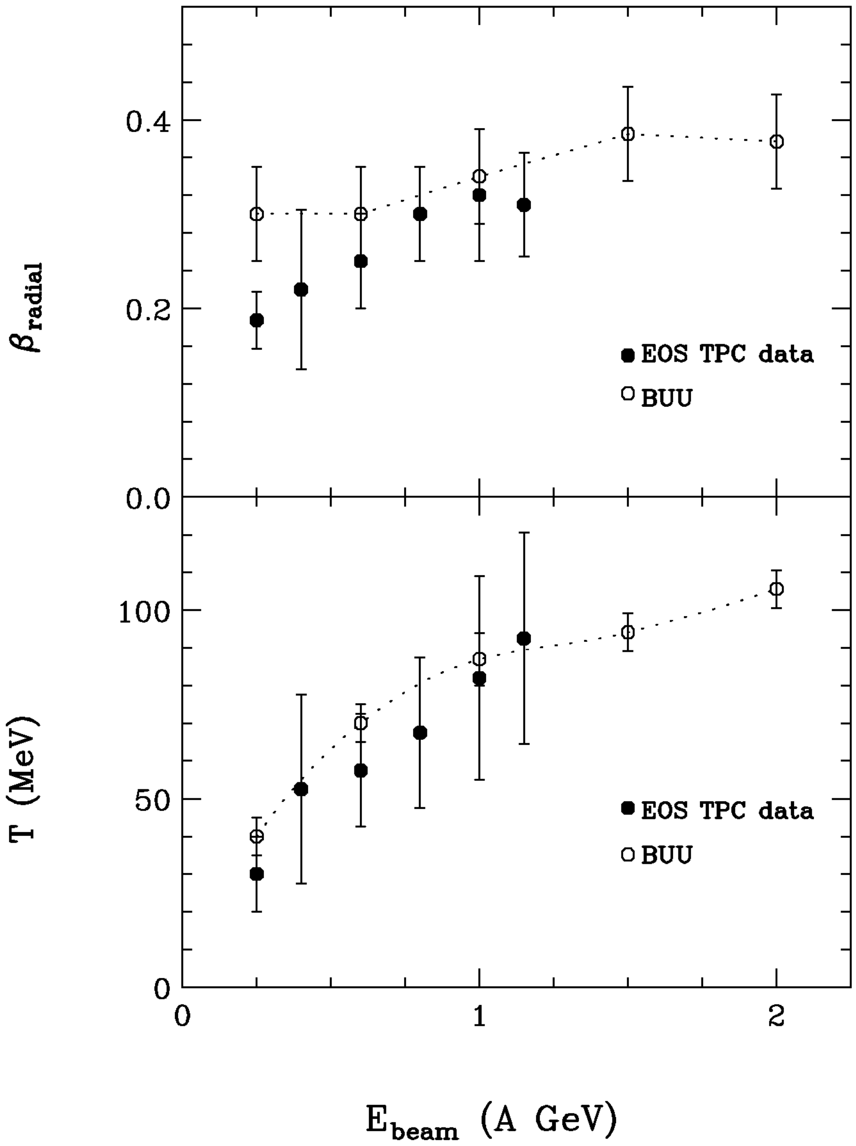

Figure 3.2: Excitation function of radial flow velocity β and apparent temperature from BUU + coalescence for impact parameter averaged ^{197}Au + ^{197}Au collisions with b$\leq$3 fm. The Au + Au phase-space is calculated using a momentum-dependent stiff equation of state from Table 2.1 and the free nucleon cross sections[PDG88].

EOS	T±5 (MeV)	$\beta \pm 0.05$
Coulomb, $\alpha = 0$		
Stiff	70	0.35
Soft	80	0.35
Soft $\vec{p}$	75	0.35
Stiff $\vec{p}$	90	0.35
No Coulomb, $\alpha = 0$		
Stiff	70	0.35
Soft	70	0.30
Soft $\vec{p}$	95	0.35
Stiff $\vec{p}$	95	0.35
Coulomb, $\alpha = -0.20$		
Stiff	75	0.35
Soft	65	0.35
Soft $\vec{p}$	80	0.35
Stiff $\vec{p}$	75	0.40
Coulomb, $\alpha = -0.50$		
Stiff	70	0.35
Soft	65	0.35
Soft $\vec{p}$	70	0.35
Stiff $\vec{p}$	90	0.35

Table 3.1: Effects of the microscopic features of BUU on apparent temperature and radial flow velocity.

that the magnitude of the radial flow, as opposed to the total radial kinetic energy, is chiefly governed by the beam energy.

In contrast, we do see striking changes in the unnormalizd kinetic energy distributions of protons and light fragments as the mean fields and in-medium cross sections are changed. This is especially pronounced in the high energy tails of the light fragment spectra, with α's showing the most sensitivity. In addition, there is some sensitivity in the temperature of the light fragment spectra to momentum dependence in the nuclear mean field, as well as to the influence of the Coulomb field.

3.4 Temperature and Microscopic Features of BUU

There are trends in the effects of the microscopic features of BUU on the extracted temperatures. The strongest is the addition of momentum dependence in the nuclear mean field. We see an increase in temperature as the momentum dependence is switched on in the calculations. We find the greatest increase in calculations devoid of Coulomb fields and using the free-space values of nucleon-nucleon cross sections, and smaller increases in those calculations which include the Coulomb fields.

The momentum-dependent terms in the mean field are repulsive at these energies. Thus, the addition of a repulsive mechanism should lead to lower densities and fewer collisions. One might expect this to decrease the extracted temperature. However, it seems that the repulsive momentum dependence tends to increase the amount of strongly thermalized matter splashing off of the hard, dense elliptical core that forms as maximum compression is reached. An explanation is that this matter, initially streaming in at beam velocity, is compressed and thermalized against this core. Since both density gradients (which by themselves offer some contribution via diffusive mechanisms) and momentum gradients are larger in the longitudinal directions than in the transverse directions, this matter will be ejected into the mid-rapidity regions. The ejection of this matter competes with the reduction of the collision rate to produce this result. This mechanism is sensitive to both the beam energy, which will set the relative importance of the mean field and collisions, and the impact parameter. Geometrical arguments imply that the angle of the major axis of this hard, dense core relative to the beam axis is strongly dependent upon the impact parameter.

There are weak trends with temperature variations and the reduction of the in-medium nucleon-nucleon cross section. We use the prescription[Kla93]

$$\sigma_{nn} = \sigma_{nn}^{free}(1 + \alpha \frac{\rho}{\rho_0})$$

where three values $\alpha = 0, -0.2$ and -0.5 are taken. One might expect that as the collision cross section decreases, the amount of beam energy converted from directed and longitudinal to random and transverse kinetic energy decreases as well. This should manifest a lower temperature. Indeed, we find this to be true for those calculations using a soft momentum-dependent and the stiff momentum-independent mean fields. However, we find no discernible change when we use soft momentum-independent mean field, and find a slight increase in temperature while using the stiff momentum-dependent mean field.

The weakness of these trends is due to the dominant role the first few nucleon-nucleon collisions play in the final single-particle kinetic energy distributions. Figure 3.3 shows single-particle momentum distributions for central Au on Au collisions at 1 GeV/A and using 200 test particles per nucleon. The top row of graphs show the distributions early in the calculations, after 10 fm/c. Here the two Fermi spheres of the initial state are clearly seen; the clouds around the origin represent the nucleons elastically scattered in these early stages. The lower row of graphs are the distributions after 30 fm/c. The kinematic cuts are represented graphically as the white lines intersecting the origins. Within these cuts, one can see the initial collisions' strong influence on the intermediate- and high-energy portions of the kinetic energy distributions after 30 fm/c. As a result, the temperature becomes sensitive to the kinematics of the initial state, namely the beam energy. The weakness of the sensitivity of the apparent temperature to the in-medium cross section is shown in the right-hand panel. Here the slopes, and thus the apparent temperature, of the kinetic energy distributions are similar.

Figure 3.4 shows the same information as Figure 3.3, but for calculations using a soft, momentum-independent equation of state. As the figure shows, most of the intermediate- and high-energy portions of the final kinetic energy distributions are

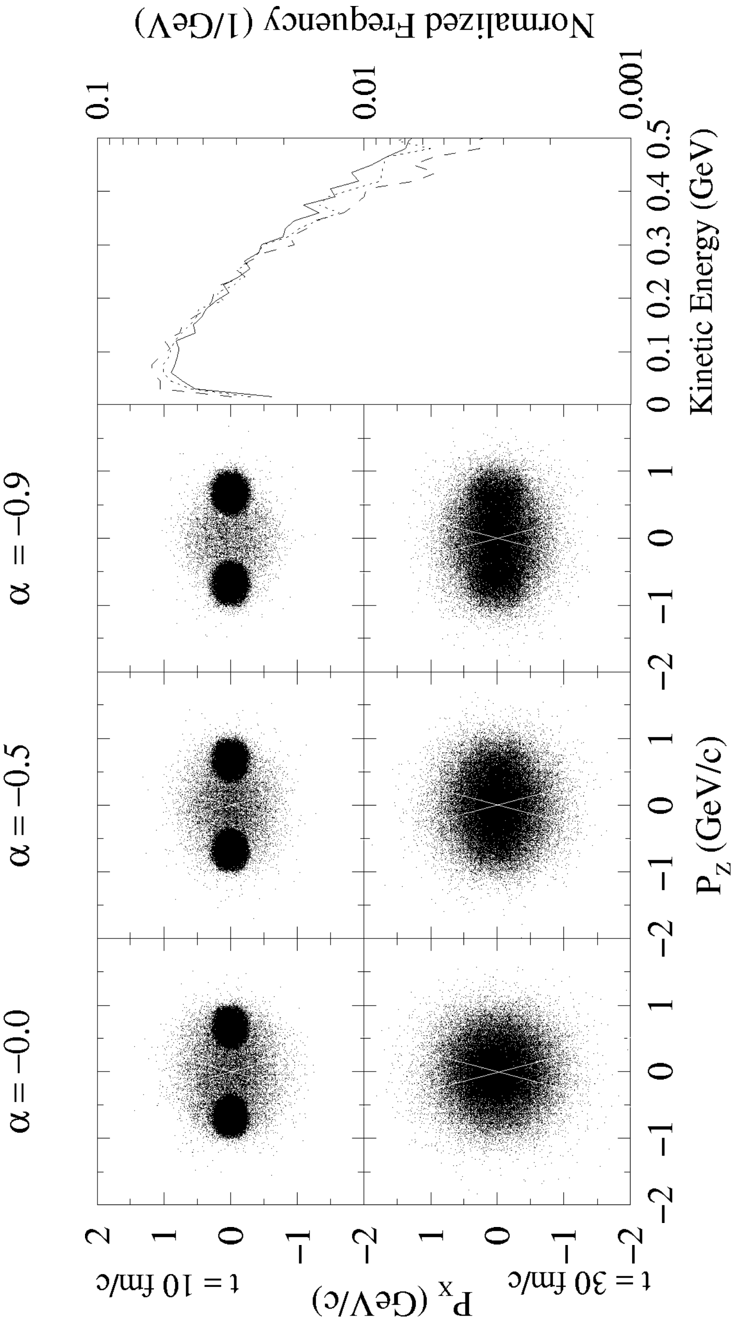

Figure 3.3: The single-particle, reaction-plane momentum distributions for central Au on Au collisions using the stiff, momentum-dependent mean field. α is the in-medium cross section reduction factor and the angular cuts are illustrated as white lines on the graphs. The right-most panel is the kinetic energy distribution of the systems after 30 fm/c for various cross section reduction factors. Solid lines are calculations using $\alpha = 0$ dotted lines $\alpha = -0.5$ and dashed lines $\alpha = -0.9$.

dominated by collisions occurring after 10 fm/c. These collisions are subject to in-medium effects, and as a result, temperature manifests a sensitivity to α. This sensitivity on α, however, is surprisingly small. We believe the nucleons that scatter elastically to 90° are constrained by momentum and energy conservation. Thus, to first order these kinematic constraints are only sensitive to the beam energy. It follows that even if we drastically decrease the scattering probabilities, the nucleons that do scatter to 90° have similar slope parameters in their energy spectrum. The net result is that the slope parameters (temperatures) only show limited sensitivity to the magnitude of the in-medium cross section.

That this limited sensitivity does not materialize in the light-fragment spectra is due primarily to the imposition of our coalescence model on the single-particle phase-space distribution upon freeze-out. Since we find the light fragment spectra to be relatively insensitive to the critical coalescence radii in configuration-space while sensitive to the momentum-space radius, to first order the coalescence we use in this study is a momentum-space coalescence. Figure 3.4 shows that a momentum-space coalescence radius of 100 MeV/c is too large to adequately resolve the nucleon density gradient in momentum-space. This effectively integrates out the features of the momentum distribution that would likely lead to different global temperatures in the light-fragment spectra as the collision cross section is modified. However, we find this radius to most accurately reproduce the proton kinetic energy spectra from the EOS-TPC experiment[Lis95].

Finally, to study the effects of Δ-decays on the final-state proton spectra, we calculate the spectra with and without those protons coming from Δ-decays. There is concern that the recoil protons receive from the decays would contaminate the spectra. Protons created in Δ-decays as a final interaction, are unlikely to contain information about the radial flow and the temperature of the system that created

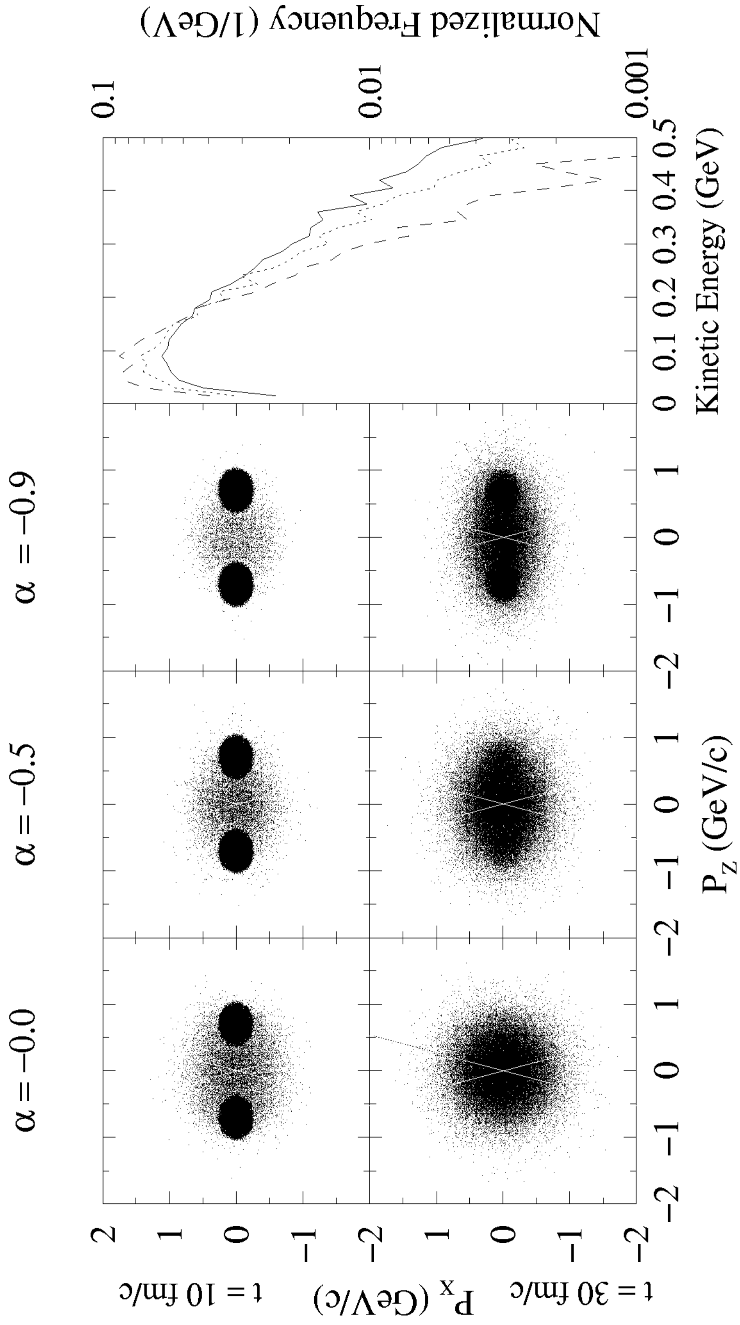

Figure 3.4: The single-particle, reaction-plane momentum distributions for central Au on Au collisions using the soft, momentum-independent mean field. α is the in-medium cross section reduction factor and the angular cuts are illustrated as white lines on the graphs. The right-most panel is the kinetic energy distribution of the systems after 30 fm/c for various cross section reduction factors. Solid lines are calculations using $\alpha = 0$, dotted lines $\alpha = -0.5$, and dashed lines $\alpha = -0.9$.

the Δ-resonances. In an effort to isolate this effect, we tag those protons the last interaction of which is a recoil from a Δ decay. We see little change in the spectra when those recoiling protons are removed. This is somewhat contrary to what is reported by the EOS-TPC collaboration[Lis95].

3.5 Concluding Remarks

A clear nonthermal component has been observed in calculated light fragment spectra in ^{197}Au + ^{197}Au collisions at beam energies of 0.25, 0.60, 1.0, 1.5 and 2.0 GeV/A with the application of a simple coalescence model to the final state phase-space from the BUU transport model. This hybrid successfully reproduces the observed temperature and radial flow velocity, within estimated uncertainties, found in light fragment spectra in an experiment by the EOS-TPC collaboration[Lis95]. Furthermore, we find unfortunately that the radial flow velocity shows little sensitivity to the microscopic features of the BUU model.

The global temperature extracted from the final-state light fragment spectra showed weak dependence on in-medium modifications to the nucleon cross section. Lower cross sections lead to lower temperatures in conjunction with a soft, momentum-dependent mean field and a stiff, momentum-independent mean field. From our calculations of the single-particle momentum distributions of central ^{197}Au on ^{197}Au collisions at 1 GeV/A using a stiff, momentum-dependent mean field, we find the final kinetic energy distributions to be dominated by beam kinematics. For calculations using a soft, momentum-independent mean field, we find the momentum-space coalescence radius to be too coarse to resolve the in-medium effects.

We find protons from the decay of Δ-resonances to have little effect on the final-state proton spectra at 1 GeV/A.

Chapter 4

Summary and Outlook

4.1 Summary

The BUU formalism has proven itself successful in providing insight into the detailed and aggregate behavior of dense, excited nuclear matter. Through the comparison of observables such as balance energy, directed flow, and radial flow to experimental values, one can estimate such bulk quantities as the compressibility of nuclear matter, and the in-medium effects on nucleon-nucleon scattering. Both of these quantities rely heavily on the short-range parts of the nuclear force, and are thus only weakly affected by the finite size of the nuclei.

The truncation in the BBGKY hierarchy[Won77, Bau86a] leads to a calculable model. Unfortunately, because of this truncation, BUU is devoid of self-consistent N-body interactions critical to the formation of clusters of nucleons found in experiments; it does not form fragments without hybridization. At low energies the BUU model shows none of the long range correlations among nuclei that give the shell-like effects in nuclei. At high energies it fails to yield quark-gluon degrees of freedom in addition to exhibiting such un-physical behavior as super-luminal momentum transport[Kor95a].

The model's forte is the evolution of the single-particle, intermediate energy

Wigner phase-space distribution. And it is here BUU shines.

Directed transverse flow was presented, and its dependence on BUU model parameters discussed. For years this observable has served the relativistic heavy-ion physics community with its sensitivity to the repulsive and attractive elements in the dynamics of heavy-ion collisions.

Momentum dependence usually enhances the repulsive elements of the dynamics of heavy-ion reactions. However, at 200 MeV/A ^{197}Au + ^{197}Au flow calculations give higher values for momentum-independent nuclear mean fields. At 400 MeV/A the effect disappears; thus, it is energy dependent. To understand this effect, sphericity tensor analysis was performed to characterize the shape quantitatively and orientation of the final-state momentum distributions. The effect was found to be caused by a more spherical, and thus less directed, final-state momentum distribution for momentum-dependent mean fields. However, these distributions did exhibit higher flow angles. Momentum-independent calculations have, by contrast, more oblate, and thus more directed, momentum distributions. However, momentum-independent distributions did exhibit lower flow angles.

A new observable, total, in-plane, transverse momentum versus rapidity was introduced, and it was studied using hypothetical momentum ellipsoids of various shapes and orientations. The sensitivity of the slope of the new observable near mid-rapidity was discussed as well as the location of the forward and backward peaks of the observable.

At high flow angles the slope is sensitive to the shape of the momentum distribution. Nevertheless, given a constant shape to the momentum ellipsoid the slope is sensitive to the flow angle, large and small. Thus, there is degeneracy in the slope at high flow angles; the observable will not uniquely map changes in the oblateness of the ellipsoid and changes in the flow angle to its mid-rapidity slope. This is not surprising given that the flow angle and the oblateness of the momentum ellipsoid are independent of one another and the slope of $\mathcal{O}(y)$ is a scalar.

The peaks of the distribution shift toward mid-rapidity while the flow angle is increased and $f_3/f_{1,2}$ held constant. For small flow angles held constant, the peaks shift away from mid-rapidity as $f_3/f_{1,2}$ is increased. However, at high flow angles held constant, the peaks show no significant shift as $f_3/f_{1,2}$ varied.

The effects of iso-spin asymmetry and in-medium cross section corrections on the balance energy were examined. Balance energy is the energy at which flow values go through zero. Recall that low-energy collisions are generally attractive, giving negative flow values. But as the energy of the collisions is increased, the repulsive elements overcome the attractive ones, and the flow turns positive.

Two iso-spin dependent mean fields were used: one from the work of Bao-An Li, *et al.*[Li95, Li96a] and one from the work of Sobotka[Sob94]. R. Pak, *et al.*[Pak97] showed that BUU under-predicts measured balance energies. The performance of BUU using each of the two iso-spin dependent mean fields was improved when the in-medium correction, Equation 1.9, included. Unfortunately, the calculations show little of the experimentally measured separation in the balance energies, at all impact parameters, between ^{58}Fe on ^{58}Fe and ^{58}Ni on ^{58}Ni collisions. The Sobotka mean field did show some separation of the balance energies at higher impact parameters, but almost none at low impact parameters. Bao-An Li's mean field showed little separation between the balance energies for all impact parameters.

The hybridization of BUU and a simple coalescence model proved successful in reproducing, within uncertainties, experimental data. The study investigated the radial and thermal velocity components of near-central Au on Au collisions for a range of energies. Radial flow did not appear sensitive to BUU model parameters. Temperature, or rather the inverse slope parameter of the kinetic energy distribution, did show marginal sensitivity to the in-medium correction factor α, see Equation 1.9, for central collisions, but little sensitivity to the compressibility of the nuclear matter.

4.2 Outlook

BUU theory has made great strides over the last decade in our understanding of heavy-ion reactions. The insight the model has provided has spurred growth in the interest of heavy-ion collisions in the ultra-relativistic regime. Currently many in the community are working to understand the quark-gluon plasma (QGP) expected from the Relativistic Heavy-Ion Collider at Brookhaven National Laboratory.

The approximations, numerical and otherwise, which enhance the model's calculability yet fail the model at high and low energies can be addressed. Hard scattering may be modified to include a kind of relativistic correction and suppress the superluminal transport. Coulomb fields may be treated as propagating with finite velocity, though this will require greater RAM than BUU currently requires.

One other weakness lies in the numerical model's inability to create clusters of nucleons. Whereas it is possible to extend the theory to include N-body dynamics, a practical numerical implementation is as yet beyond us.

Nonetheless, BUU has been and will continue to be the premiere model for intermediate energy heavy-ion collisions for some time to come.

Bibliography

[Aich87] J. Aichelin, A Rosenhauer, G. Peilert, H. Stoecher, and W. Greiner, Phys. Rev. Lett. **58**, 1926, (1987).

[Alm95] T. Alm, G. Röpke, W. Bauer, F. Daffin and M. Schmidt, Nucl. Phys. **A587**, 815, (1995).

[Bar85] E. Baron, J. Cooperstein, and S. Kahana, Phys. Rev. Lett. **55**, 126, (1985).

[Bar94] J. Barrette, R. Bellwied, P. Braun-Munzinger, W. E. Cleland, T. M. Cormier, G. David, J. Dee, G. E. Diebold, O. Dietzsch, J. V. Germani, S. Gilbert, S. V. Greene, J. R. Hall, T. K. Hemmick, N. Herrmann, B. Hong, K. Jayananda, D. Kraus, B. S. Kumar, R. Lacasse, D. Lissauer, W. J. Llope, T. W. Ludlam, S. McCorkle, R. Majka, S. K. Mark, J. T. Mitchell, M. Muthuswamy, E. O'Brien, C. Pruneau, F. S. Rotondo, J. Sandwiess, N. C. daSilva, U. Sonnadara, J. Stachel, H. Takai, E. M. Takagui, T. G. Throwe, D. Wolfe, C. L. Woody, N. Xu, Y. Zhang, Z. Zhang, and C. Zou, Phys. Rev. C **50**, 1077, (1994).

[Bau86] W. Bauer, G. F. Bertsch, and U. Mosel, Phys. Rev. C **34**, 2127, (1986).

[Bau86a] W. Bauer, Ph.D. thesis, University of Giessen, 1986.

[Bau88] W. Bauer, Phys. Rev. Lett. **61**, 2534, (1988).

[Ber84] G. F. Bertsch, H. Kruse, and S. Das Gupta, Phys. Rev. C **29**, 673 (1984).

[Ber87] G. F. Bertsch, W. G. Lynch, and M. B. Tsang, Phys. Lett. B **189**, 384, (1987).

[Ber88] G. F. Bertsch, and S. Das Gupta, Phys. Rep. **160**, 189, (1988).

[Bon76] J. P. Bondorf, P. J. Siemens, S. Garpman, and E. C. Halbert, Z. Phys. **A279**, 385 (1976).

[Brü55] K. A. Brückner, Phys. Rev. **97**, 1353, (1955).

[But63] S. T. Butler, and C. A. Pearson, Phys. Rev. **129**, 836, (1963).

[Cse86] L. P. Csernai, and J. I. Kapusta, Phys. Rep. **131**, 223, (1986).

[Cug81] J. Cugnon, T. Mizutani, and J. Vandermeulen, Nucl. Phys. **A352**, 505, (1981).

[Dan85] P. Danielewicz, and G. Odyniec, Phys. Lett. **157B**, 146, (1985).

[Dan91] P. Danielewicz, and G. F. Bertsch, Nucl. Phys. **A533**, 712, (1991).

[Dan92] P. Danielewicz, and Q. Pan, Phys. Rev. C **46**, 2002, (1992).

[Dan95] P. Danielewicz, Phys. Rev. C **51**, 716, (1995).

[Dan97] P. Danielewicz, private communication, 1997.

[Das81] S. Das Gupta, and A. Z. Mekjian, Phys. Rep. **72**, 131, (1981).

[Dov91] C. B. Dover, U. Heinz, E. Schnedermann, and J. Zimányi, Phys. Rev. C **44**, 1636, (1991).

[Gale87] C. Gale, G. Bertsch, and S. Das Gupta, Phys. Rev. C **35**, 1666, (1987).

[Gale90] C. Gale, G. M. Welke, M. Prakash, S. J. Lee, and S. Das Gupta, Phys. Rev. C **41**, 1545, (1990).

[Gos77] J. Gosset, H. H. Gutbrod, W. G. Meyer, A. M. Poskanzer, A. Sandoval, R. Stock, and G. D. Westfall, Phys. Rev. C **16**, 629, (1977).

[Gut89] H. H. Gutbrod, K. H. Kampert, B. W. Kolb, A. M. Poskanzer, H. G. Ritter, and H. R. Schmidt, Phys. Lett. B **216**, 267, (1989).

[Gut90] H. H. Gutbrod, K. H. Kampert, B. Kolb, A. M. Poskanzer, H. G. Ritter, R. Schicker, and H. R. Schmidt, Phys. Rev. C **42**, 640, (1990).

[Gyu82] M. Gyulassy, K. A. Frankel, and H. Stöcker, Phys. Lett. **110B**, 185, (1982).

[Har95] J. Harris, W. Lynch, B. Zajc, W. Bauer, M. Gyulassy, J. Natowitz, J. Stachel, Report of the Intermediate and High Energy Heavy-Ion Reactions: NSAC/DNP Town Meeting-Brookhaven National Laboratory, January 27-28, 1995.

[Hua96] M. J. Huang, R. C. Lemmon, F. Daffin, W. G. Lynch, C. Schwarz, M. B. Tsang, C. Williams, P. Danielewicz, K. Haglin, W. Bauer, N. Carlin, R. J. Charity, R. T. de Souza, C. K. Gelbke, W. C. Hsi, G. J. Kunde, M.-C. Lemaire, M. A. Lisa, U. Lynen, G. F. Peaslee, J. Pochodzalla, H. Sann, L. G. Sobotka, S. R. Souza, and W. Trautmann, Phys. Rev. Lett. **77**, 3739, (1996).

[Jac84] B. V. Jacak, D. Fox, and G. D. Westfall, Phys. Rev. C **31**, 704, (1984).

[Jeu76] J. P. Jeuhenne, A. Lejeune, and C. Mahaux, Phys. Rep. **25**, 85 (1976).

[Kap80] J. I. Kapusta, Phys. Rev. C **21**, 1301, (1980).

[Kla93] D. Klakow, G. Welke, and W. Bauer, Phys. Rev. C **48**, 1982, (1993).

[Koon79] S. E. Koonin, "The time-dependent Hartree-Fock description of heavy-ion collisions," in *Heavy Ion Interactions at Hight Energies*, edited by D. Wilkinson, Peogress in Particle and Nuclear Physics (Pergamon, Oxford), Vol. 4, p. 283.

[Kor95] G. Kortemeyer, F. Daffin, and W. Bauer, Phys. Lett. B **374**, 25, (1995).

[Kor95a] G. Kortemeyer, W. Bauer, K. Haglin, J. Murray, and S. Pratt, Phys. Rev. C **52**, 2714, (1995).

[Kro92] D. Krofcheck, W. Bauer, G. M. Crawley, S. Howden, C. A. Ogilvie, A. Vander Molen, G. D. Westfall, and W. K. Wilson, Phys. Rev. C **46**, 1416, (1992).

[Kru85] H. Kruse, B. V. Jacak, J. J. Molitoris, G. D. Westfall, and H. Stöcker, Phys. Rev. C **31**, 1770, (1985).

[Lan93] A. Lang, H. Badovsky, W. Cassing, U. Mosel, H.-G. Reusch, and K. Weber, J. Comp. Phys. **106**, 391, (1993).

[Lat91] James M. Lattimer, C. J. Pethick, Madappa Prakash, and PawełHaensel, Phys. Rev. Lett. **66**, 2701, (1991).

[Lem79] M. C. Lemaire, S. Nagamiya, S. Schnetzer, H. Steiner, and I. Tanihata, Phys. Lett. **85B**, 38, (1979).

[Li93] Bao-An Li, Phys. Rev. C **48**, 2415, (1993).

[Li95] Bao-An Li, and Sherry J. Yennello, Phys. Rev. C **52**, R1746, (1995).

[Li96a] Bao-An Li, Zhongzhou Ren, C. M. Ko, and Sherry J. Yennello, Phys. Rev. Lett. **76**, 4492, (1996).

[Li96b] Bao-An Li, and C. M. Ko, "Excitation Functions in Central Au+Au Collisions", Texas A&M preprint, nucl-th/9601041.

[Lis95] M. A. Lisa, S. Albergo, F. Bieser, F. P. Brady, Z. Caccia, D. A. Cebra, A. D. Chacon, J. L. Chance, Y. Choi, S. Costa, J. B. Elliott, M. L. Gilkes, J. A. Hauger, A. S. Hirsch, E. L. Hjort, A. Insolia, M. Justice, D. Keane, J. Kintner, H. S. Matis, M. McMahan, C. McParland, D. L. Olson, M. D. Partlan, N. T. Porile, R. Potenza, G. Rai, J. Rasmussen, H. G. Ritter, J. Romanski, J. L. Romero, G. V. Russo, R. Scharenberg, A. Scott, Y. Shao, B. K. Srivastava, T. J. M. Symons, M. Tincknell, C. Tuvé, S. Wang, P. Warren, G. D. Westfall, H. H. Wieman, and K. Wolf, Phys. Rev. Lett. **75**, 2662, (1995).

[Llo95] W. J. Llope, S. E. Pratt, N. Frazier, R. Pak, D. Craig, E. E. Gualtieri, S. A. Hannuschke, N. T. B. Stone, A. M. Vander Molen, G. D. Westfall, J. Yee, R. A. Lacey, J. Laurent, A. C. Migerey, and D. E. Russ, Phys. Rev. C **52**, 2004, (1995).

[Mek77] A. Mekjian, Phys. Rev. Lett. **38**, 640, (1977).

[Mül95] Horst Müller, and Brian D. Serot, Phys. Rev. C **52**, 2072, (1995).

[Nag94] J. L. Nagle, B. S. Kumar, M. J. Bennett, S. D. Coe, G. E. Diebold, and J. K. Pope, Phys. Rev. Lett. **73**, 2417, (1994).

[Nag96] J. L. Nagle, B. S. Kumar, D. Kusnezov, H. Sorge, and R. Mattiello, Phys. Rev. C **53**, 367, (1996).

[Neg82] J. W. Negele, Rev. Mod. Phys. **54**, 913, (1982).

[Ogi89] C. A. Ogilvie, D. A. Cegra, J. Clayton, P. Danielewicz, S. Howden, J. Karn, A. Nadasen, A. Vander Molen, G. D. Westfall, W. K. Wilson, and J. S. Winfield, Phys. Rev. C **40**, 2592, (1989).

[Ogi90] C. A. Ogilvie, W. Bauer, D. A. Cebra, J. Clayton, S. Howden, J. Karn, A. Nadasen, A. Vander Molen, G. D. Westfall, W. K. Wilson, and J. S. Winfield, Phys Rev. C **42**, R10, (1990).

[Pak97] R. Pak, Bao-An Li, W. Benenson, O. Bjarki, J. A. Bown, S. A. Hannuschke, R. A. Lacey, D. J. Magestro, A. Nadasen, E. Norbeck, D. E. Russ, M. Steiner, N. T. B. Stone, A. M. Bander Molen, G. D. Westfall, L. B. Yang, and S. J. Yennello, Phys. Rev. Lett. **78**, 1026, (1997).

[PDG88] Particle Data Group, Phys. Lett. **B**, April, 126, (1988).

[Sat81] H. Sato, and K. Yazaki, Phys. Lett. **98B**, 153 (1981).

[Sch63] A. Schwarzchild, and C. Zupančič, Phys. Rev. **129**, 854, (1963).

[Sch98] A. Schnell, G. Röpke, U. Lombardo, and H.-J. Schulze, Phys. Rev. C **57**, 806, (1998).

[Ser47] R. Serber, Phys. Rev. **72**, 1114, (1947).

[Sie79] P. J. Siemens, and J. O. Rasmussen, Phys. Rev. Lett. **42**, 880 (1979).

[Skyr59] T. H. R. Skyrme, Nucl. Phys. **9**, 615, (1959).

[Smi77] K. Smith, and M. Danos, Proc. of the Fall Creek Falls State Park Conference, Tennessee, June 1977.

[Sob94] L. G. Sobotka, Phys. Rev. C **50**, R1272, (1994).

[Sor95] H. Sorge, J. L. Nagle, and B. S. Kumar, Phys. Lett. **B355**, 27, (1995).

[Tsa88] M. B. Tsang, W. G. Lynch, R. Ronningen, A. Chen, C. K. Gelbke, T. K. Nayak, J. Pochodzalla, F. Zhu, M. Tohyama, W. Trautmann, and W. Dünnweber, Phys. Rev. Lett. **60**, 1479, (1988).

[Tsa89] M. B. Tsang, G. F. Bertsch, W. G. Lynch, and M. Tohyama, Phys. Rev. C **40**, 1685, (1989).

[Ueh33] E. A. Uehling, and G. E. Uhlenbeck, Phys. Rev. **43**, 552 (1933).

[Wan95] S. Wang, S. Albergo, F. Bieser, F. P. Brady, Z. Caccia, D. A. Cebra, A. D. Chacon, J. L. Chance, Y. Choi, S. Costa, J. B. Elliott, M. L. Gilkes, J. A. Hauger, A. S. Hirsch, E. L. Hjort, A. Insolia, M. Justice, D. Keane, J. Kintner, M. A. Lisa, H. S. Matis, M. McMahan, C. McParland, D. L. Olson, M. D. Partlan, N.T. Porile, R. Potensza, G. Rai, J. Rasmussen, G. G. Ritter, J. Romanski, J. L. Romero, G. V. Russo, R. P. Scharenberg, A. Scott, Y. Shao, B. K. Srivastava, T. J. M. Symons, M. L. Tincknell, C. Tuvè, P. G. Warren, D. Weerasundara, H. H. Wieman, and K. L. Wolf, Phys. Rev. Lett. **74**, 2646, (1995).

[Wel88] G. M. Welke, M. Prakash, T. T. S. Kuo, S. Das Gupta, and C. Gale, Phys. Rev. C **38**, 2101, (1988).

[Wes90] G. D. Westfall, C. A. Ogilvie, D. A. Cebra, W. K. Wilson, A. Vander Molen, W. Bauer, G. S. Winfield, D. Krofcheck, J. Darn, S. Howden, T. Li, R. Lacey, K. Tyson, and M. Cronqvist, Nucl. Phys. **A519**, 141, (1990).

[Wes93] G. D. Westfal, W. Bauer, D. Craig, M. Cronqvist, E. Gualtieri, S. Hannuschke, D. Klakow, T. Li, T. Reposeur, A. M. Vander Molen, W. K.

Wilson, J. S. Winfield, J. Yee, and S. J. Yennello, Phys. Rev. Lett. **71**, 1986, (1993).

[Won77] C.-Y. Wong, and J. A. McDonald, Phys. Rev. C **16**, 1196, (1977).